NPL
National Physical Laboratory

NPL REPORT MS 32

EMPIR PROJECT 17IND01 MIMAS (MEDICAL IMPLANT MANUFACTURERS' SAFETY PROCEDURES): DELIVERABLE D07

L WRIGHT, D BOWNDS, J WOOLDRIDGE, M COX, I PARTARRIEU, L R WRIGHT, T GOREN, A YAO, O BOTTAUSCIO, L ZILBERTI, M CHIAMPI, U ZANOVELLO, A ARDUINO

SEPTEMBER 2021

EMPIR Project 17IND01 MIMAS (Medical Implant Manufacturers' Safety Procedures): Deliverable D07

L. Wright, J. Wooldridge, M. Cox, I. Partarrieu, L. R. Wright,
Data Science Department, NPL.

D. Bownds,
Electromagnetic Measurements Group, NPL.

T. Goren, A. Yao,
ZMT.

O. Bottauscio, L. Zilberti, M. Chiampi, U. Zanovello, A. Arduino,
INRIM.

ABSTRACT

This report is the deliverable D07 of EMPIR project 17IND01 MIMAS, described in the project protocol as "Report on a statistical method to demonstrate MRI compliance for small (<10 cm) orthopaedic implants, including analysis of implant exposures within human surrogates during MRI scan by implant type and the feasibility of the application of stochastic approaches to risk assessment for implant bearing patients undergoing MRI scans".

ISSN 1754-2960

https://doi.org/10.47120/npl.MS32

National Physical Laboratory
Hampton Road, Teddington, Middlesex, TW11 0LW

Approved on behalf of NPLML by
Peter Harris, Science Area Leader for Data Analytics & Modelling

CONTENTS

1 INTRODUCTION

This report summarises the activities carried out to construct statistical and parametric models of radio frequency-induced and gradient-induced heating of orthopaedic implants during MRI scans.

The heating effects during a scan are affected by many different factors. In some cases (implant size, scan sequence, etc.) it is possible to perform controlled experiments to assess the effects of these factors. In other cases, principally those associated with the human body and its variability, it is more difficult to isolate, identify, and quantify the effects. The work reported here has therefore used a variety of approaches to assess variability of temperature rise due to these effects.

The work has investigated the controllable effects in detail for RF and gradient-field MRI scans separately: the radio frequency (RF) work is reported in section 2, and the gradient coil (GC) work in section 3. A common approach has been used for the two investigations. The influencing parameters have been identified and ranges have been assigned to each parameter. Computer simulations have been used to examine the effects of the geometric, material, and scan sequence parameters on heating of simplified parameterised geometries. Simplified geometries have been used because the geometry of realistic implants is too complicated to parameterise in a meaningful way, and because initial tests showed that for some implants (screws and simple plates) the simplified geometry gave similar results to realistic geometries. Realistic implant geometries have also been analysed under various conditions to link results to actual implant geometries. For the RF case, measurements of uniform rods of different lengths and radii have been made, and the same cases have been simulated to provide a validation of the computational approach.

The uncontrollable parameters have been examined in a more statistical sense, by considering the variability of implant recipients and the risk associated their exposure to electromagnetic fields, focussing on the RF heating. This work is reported in section 4. The detailed human models available within Sim4Life have been used to calculate the E-fields incident during three typical common scans (knee, hip and shoulder), and the results have been analysed. Publicly available data sets describing the prevalence of MRI scans and orthopaedic implants have been combined with this analysis of the E-fields to estimate the likelihood of a person with an implant having an MRI scan, and hence their likely E-field exposure. This information has then been used to assess the feasibility of a stochastic risk analysis for MR implant safety.

The sensitivity of the temperature rise to the properties of human tissue have been considered, as reported in section 5. The distribution of tissue types within the models has been examined, and the effects of perfusion (an important difference between measurements in a phantom and the situation in a human undergoing a scan) have been examined to generate correction factors for measurements of phantoms.

This project has received funding from the EMPIR programme co-financed by the Participating States and from the European Union’s Horizon 2020 research and innovation programme (grant 17IND01 – MIMAS).

1.1 RELEVANT ELECTROMAGNETIC PHENOMENA

Two electromagnetic phenomena affect the results presented in this report, and it is helpful to explain them ahead of the results. The phenomena are skin depth and the antenna effect.

The skin depth effect occurs in materials of high conductivity. The electric field inside materials decays exponentially in magnitude with distance from the surface. The field

penetration depth δ (the depth at which the field reaches 1/*e* of its surface value) is estimated from

$$\delta = \sqrt{\frac{2}{\sigma\omega\mu}}, \quad (1)$$

where σ is the electrical conductivity, ω is the frequency of the field, and μ is the magnetic permeability of the implant (typically equal to 1.0). For RF coils in typical clinical MRI scanners, where the magnetic field strength is typically 1.5 T or 3.0 T corresponding to RF frequencies of 64 MHz or 128 MHz, the skin depth is of the order of 10 μm – 100 μm. For GC coils, the relevant frequency is the fundamental frequency associated with the pulse sequence, which is determined from the Fourier transform of the detailed pulse sequence and typically lies in the range 50 Hz – 2000 Hz, the skin depth varies from 10 mm to 100 mm and hence is comparable with the dimensions of the implants so there is significant electric field strength inside the implants, but for higher frequencies and hence smaller skin depths, the field may not be significant everywhere inside larger implants.

Any long thin object in an electric field will behave like a dipole antenna. The electromagnetic field around the object tends to be strongly affected by the length of the object and the properties of the material surrounding the object. For a surrounding material of magnetic permeability μ, electric permittivity ϵ, electrical conductivity, and a field of frequency ω, the maximum power will be deposited in the material when the object has length

$$L = \frac{\pi\sqrt{2}}{\omega\sqrt{\mu\epsilon}}\left[1 + \sqrt{1 + \frac{\sigma^2}{\omega^2\epsilon^2}}\right]^{-1/2}, \quad (2)$$

which is half of the resonant wavelength, and integer multiples of this value. This effect means that the dependence of power on object length is not monotonic and depends on the properties of the surrounding material. For a gel phantom, the values of *L* at 64 MHz and 128 MHz are 21.7 cm and 12.2 cm respectively. In practice, the dimensions of the object in the other directions also affect the resonant length, and it is generally found that the resonant length lies between *L* and *L*/2.

2 PARAMETRIC ANALYSIS OF IMPLANT-RELATED FACTORS AFFECTING RF INDUCED TEMPERATURE RISES

2.1 RELEVANT PARAMETERS

Following discussions between the project partners, it was agreed that the work would focus on orthopaedic screws and plates. Stents were also proposed as a topic of interest, but a literature search showed that extensive research (including simulation) on stents had already taken place and so they were omitted from this work as they are already well understood.

The following parameters were identified as affecting the RF-induced heating for both screws and plates:

- MRI field strength,
- Orientation of the implant relative to the scanner,
- Position of the implant within the scanner,
- Nature of the tissue surrounding the implant,
- Material properties of the implant material,
    - Electrical conductivity, thermal conductivity, specific heat capacity, density.

The following parameters were identified as affecting the RF-induced heating for screws:

- Length,
- Diameter,
- Tip sharpness (quantified as an aspect ratio of a cone),
- Presence of thread,
- Cannulation.

The following parameters were identified as affecting the RF-induced heating for plates:

- Length,
- Width,
- Thickness.

Several other factor were suggested for consideration, including the presence of holes in plates, the use of mesh rather than solid materials, and the detailed local geometry of plates when adapted to fit an individual patient. It was decided that these factors were too difficult to parameterise effectively and to simulate accurately.

The factors of position in the scanner and tissue properties directly surrounding the implant are specifically addressed in separate tasks within this work package, and so these factors were omitted from the sensitivity analysis. The simulations were carried out following the procedure defined in ASTM F2182 [1], so the tissue material properties were those of the ASTM gel (see section 2.2 for a complete definition of the approach used).

The majority of the parameters are independent. Several parameters are categorical and so have had discrete values assigned rather than ranges. In particular:

- MRI field strength could be 1.5 T or 3.0 T,
- Implant properties could be those of Titanium or Titanium alloy, listed in table 2 below.

Ranges for the geometric parameters of the screws and the plates were identified based on the contents of Medartis medical supply catalogues [2]. These parameters are correlated, because screws and plates are typically designed to have a particular bending stiffness so that for a given length, only a small range of screw diameters or plate thicknesses will be used.

Based on the screw diameters and lengths seen in the catalogues, the diameter of the screws was varied between 1 mm and 7 mm. Five screw lengths, listed in table 1, were selected for each screw diameter.

Table 1: Screw lengths for each diameter

Diameter (mm)	Lengths (mm)
1	2, 4, 6, 8, 10
2	4, 10.5, 17, 23.5, 30
3	12, 19, 26, 33, 40
4	15, 26.25, 37.5, 48.75, 60
5	20, 35, 50, 65, 80
6	30, 47.5, 65, 82.5, 100
7	40, 60, 80, 100, 120

For each combination of screw diameter and length, five different tip aspect ratios were considered. The tip of the screw was defined as a cone of height $H = \alpha D$, where D is the screw diameter. The parameter α was set equal to 0.2, 0.4, 0.6, and 0.8 for each screw geometry, and a rounded tip was also considered. These screw geometries are shown in figure 1.

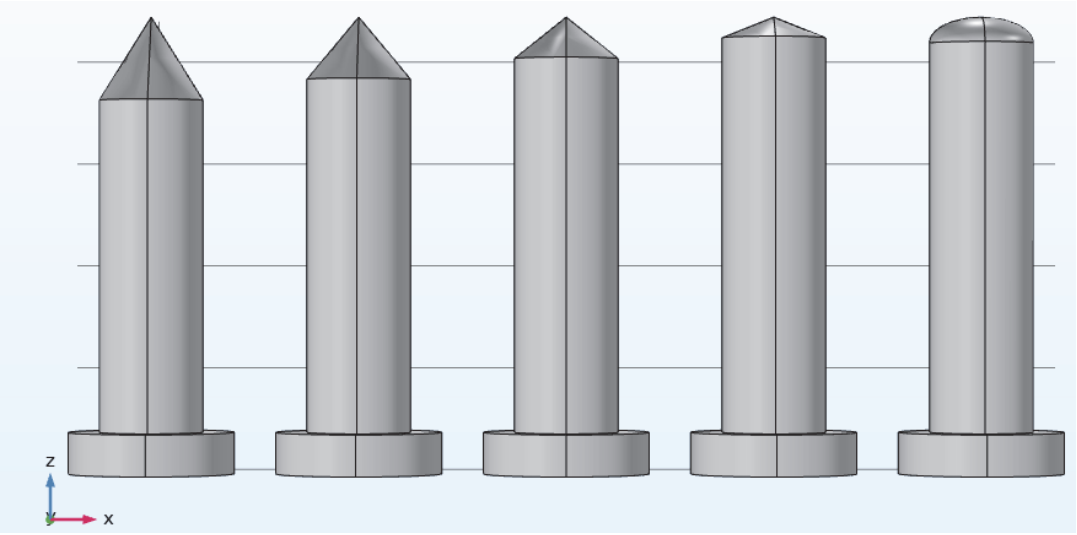

Figure 1: Tip aspect ratios used in initial screw models.

It was decided that initially single simulations would be used to address the effects of cannulation and screw thread, with the idea that the study would be extended if either factor had a significant effect.

2.2 SENSITIVITY OF TEMPERATURE RISE TO PARAMETERS

Throughout the following, models have been run using 1.5 T and 3.0 T fields. In all cases, the 1.5 T fields led to higher temperature rises. In all cases, the model has simulated the process described in ASTM F2182-11 [1], so the electromagnetic field was turned on for 900 s (15 minutes) and the sample was then allowed to cool. The peak temperature therefore occurred at 900 s, and so the maximum temperature within the model at 900 s is the result most frequently plotted below.

2.2.1 Model overview

A series of RF heating simulations was constructed using COMSOL Multiphysics v5.5 [3], in which a 16 rung birdcage coil was modelled with a geometry to match those of body coils in typical commercial scanners (birdcage radius of 0.3 m, length of 0.6 m, high-pass design). An RF shield (of radius 0.4 m and length 0.7 m) was placed around the birdcage coil [4]. The entire system is enclosed within an air sphere of radius 1.5 m, with the phantom located centrally within the coil. Implants are placed within the phantom centred on the isocentre plane of the coil, located close to the edge of the phantom within the highest intensity and most uniform section of the electric field.

The coil and shield were both modelled within COMSOL as perfect electrical conductors. The coil is excited at the mid-point of each rung with sinusoidal input of 63.9 MHz and 127.7 MHz (a stationary magnetic flux density B_0 of 1.5 T and 3.0 T respectively), varying in phase from 0 rad to 2π rad around the circumference of the coil. A capacitor was placed at the top and bottom of each rung, and a series of parametric sweeps in capacitance was performed to tune the coil to the desired mode 1 resonance frequency [4] for each B_0 field. The outermost sphere in the geometry is defined as an absorbing boundary to prevent any reflections into the modelling domain. Finally, given the skin depth of the metallic implants is in the range 30 μm to 80 μm for the materials and frequencies considered in this study, the internal parts of the implant were not calculated within the electromagnetic part of the simulation; rather the surface of the implant was modelled using an impedance boundary condition [5]. Table 2 shows the electromagnetic properties of the implants used in the model. All implants were set to have a relative electric permittivity of 1.0 (assigning electrical conductivity separately).

Table 2: Material properties of the implants [25-43].

Material	Thermal conductivity (W/ (m K))	Specific heat capacity (J/(kg K))	Density (kg/m^3)	Electrical conductivity (MS/m)
CoCrMo alloy	14	450	8845	1.16
Ti alloy (Ti6Al4V)	7.2	520	4420	5.81
Titanium	19	523	4512	2.13
Steel	15	500	7900	1.25

Tables 3 and 4 show (respectively) the thermal and electromagnetic properties of the materials simulated as surrounding the implants. The electromagnetic properties show a small amount of frequency dependence.

Table 3: Thermal properties of the surrounding tissue [44].

Material	Thermal conductivity (W/ (m K))	Specific heat capacity (J/(kg K))	Density (kg/m^3)
Muscle	0.50	3421	1090
Cancellous bone	0.31	2274	1178
Cortical bone	0.32	1313	1908
Saline gel	0.54	4152	998

Table 4: Electromagnetic properties of the surrounding tissue [45].

Material	Electrical Conductivity (S/m)		Relative permittivity	
	At 64 MHz	At 128 MHz	At 64 MHz	At 128 MHz
Muscle	0.69	0.72	72.2	63.5
Cancellous bone	0.16	0.18	30.9	26.3
Cortical bone	0.06	0.07	16.7	14.7
Saline gel	0.47	0.47	80	80

The model calculates the electromagnetic field throughout the entire domain outside of the implant and calculates the temperature distribution within the phantom and the implant. The SAR can then be calculated from [1]

$$SAR = \frac{\sigma|\mathbf{E}|^2}{2\rho}, \tag{3}$$

where **E** is the electric field, σ is the electrical conductivity, and ρ is the density. The SAR calculated from the electric field varies spatially. In some cases the temperature rise has been normalised by the local SAR without the implant in place, with the intention that any effects of the location of the implant within the phantom can be reduced, but since the implants are in the same place in all models this is unnecessary.

2.2.2 Screws and rods

An initial study of screw heating was carried out using geometries that included a sharpened tip and a representation of the screw head, as illustrated in figure 1. An additional run was carried out that included a screw thread on a screw of 3 mm diameter and 50 mm length, as shown in figure 2(a).

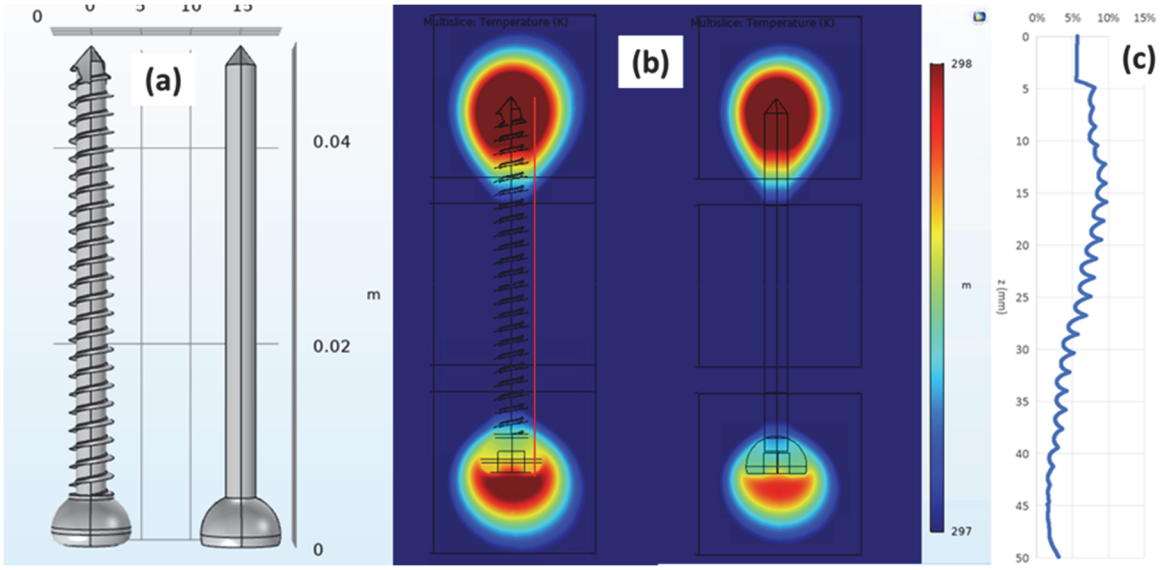

Figure 2: Geometry and temperature results for comparable models with and without a screw thread.

The model results suggested that the screw thread had a minor effect on the temperature and the local SAR. Figure 2(b) shows the temperature contours around the screw to the same scale, suggesting that the thread does not cause a significant amount of local heating. The maximum difference in local SAR was 6 % at one end of the screw and 7 % at the other. Figure 2(c) shows the temperature difference between the two models as a percentage of the temperature in the model with the screw thread along the red line parallel to the screw shown adjacent to the left hand screw in figure 2(b). Note that the large percentage differences occur in regions where the temperature rise is low. The details of screw thread were therefore omitted from subsequent analyses.

A set of 18 model runs was carried out using a screw of length 40 mm and diameter 3 mm to examine the effects of field orientation. The screw showed the highest level of heating when the screw axis and the coil axis are parallel. This orientation is most severe because of the

antenna effect, discussed in section 1.1 above. The line plots in the polar chart shown in figure 3 are asymmetric due to the normalisation by background SAR level with no implant present, which has a left-right asymmetry within the phantom.

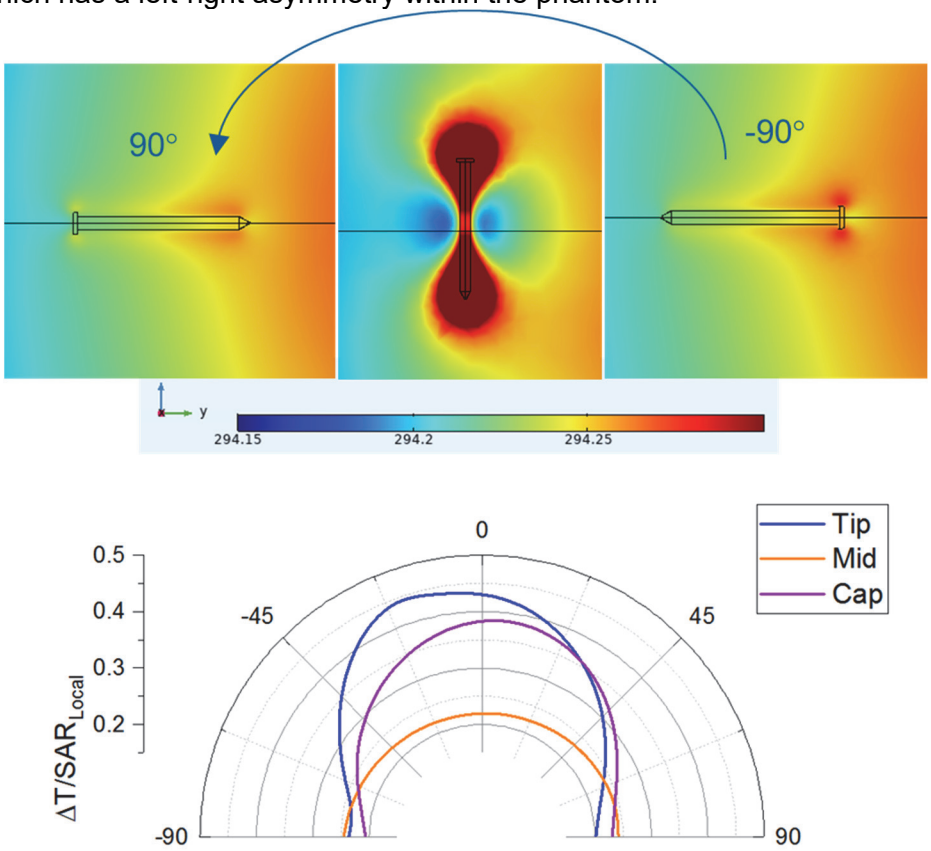

Figure 3: The effects of screw orientation on the temperature rise

Many orthopaedic screws are deployed perpendicular to the length of the bone they are attached to. Since most MRI scans involve the patient's limbs (and hence most of their bones) being parallel to the coil access, this may make the worst-case configuration less likely for some screws, but screws in the skull or collar-bone are likely to have this orientation and so may be problematic. In general the orientation can be considered as multiplying the temperature rise by a factor of cos α where α is the angle between the longest dimension of the implant and the direction of the static B0 field. Note that the time-varying B1 field will lie within the plane perpendicular to the B0 field, and will be randomly oriented in relation to the implant.

The results of the models with varying tip sharpness suggested that the sharpness had very little effect on the temperature rise and the SAR. Figure 4 shows the relative difference between values of the maximum temperature rise divided by local SAR for pairs of models with the same geometry but different tip aspect ratios.

Figure 5 shows results for a single tip sharpness and for all diameters and lengths. Each symbol represents a different diameter of screw, and the values are plotted against length. The results obtained from screws of different diameters are consistent, showing that the screw length has the dominant effect. It was found that the results can be well fitted by a function of the form

$$\frac{\Delta T}{SAR_{local}} = A + BL^2. \qquad (4)$$

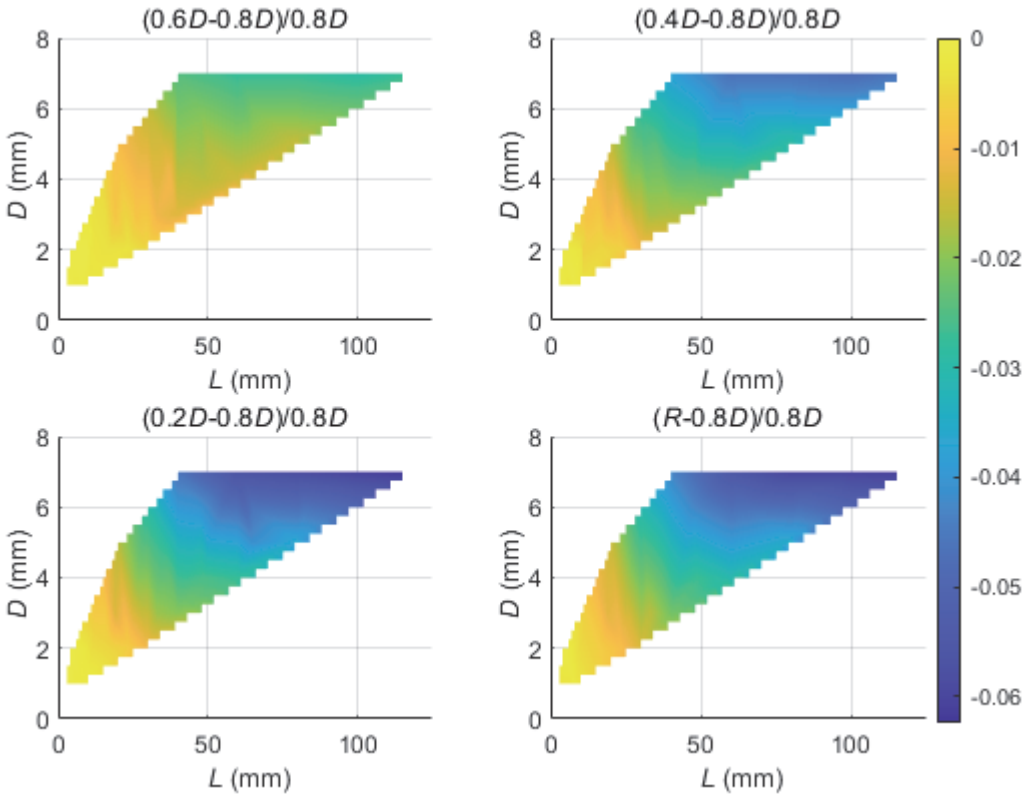

Figure 4: Relative difference in maximum temperature rise divided by local SAR for models of different tip aspect ratio. *R* denotes the rounded tip and "0.8 *D*" refers to the model with a tip aspect ratio of 0.8.

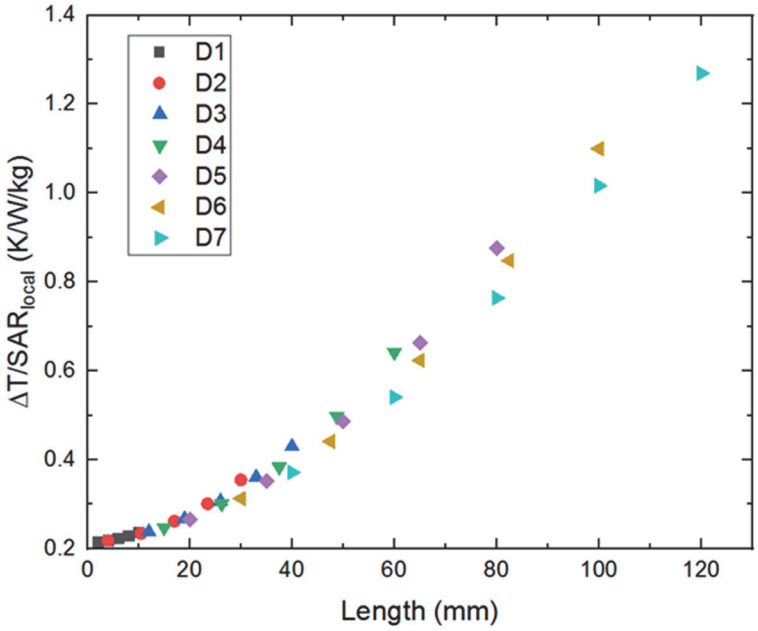

Figure 5: Results from models with a tip parameter of 0.8.

The results presented above show that screws can be well approximated by cylinders for modelling heating. All subsequent model results reported in this section come from models of cylinders unless otherwise stated.

As was noted in section 1.1 above, long thin objects such as cylinders behave in a similar way to an antenna in RF fields. A given set of material properties of the surrounding tissue has a resonant length, and the maximum heating for a thin cylinder will be close to that resonant length with the exact length being affected by the radius. Figure 6 shows the maximum temperature rise in the model after 900 s of the applied RF field as a function of cylinder length (horizontal axis) and diameter (vertical axis). The upper plot is for a field of 1.5 T and the lower plot is for a field of 3.0 T. Both plots show that for a given diameter of cylinder there is a particular cylinder length that leads to a maximum temperature rise, and that the relationship between the length and the temperature rise is nonlinear and non-monotonic. Some noise is present in the results due to variations of mesh within the models.

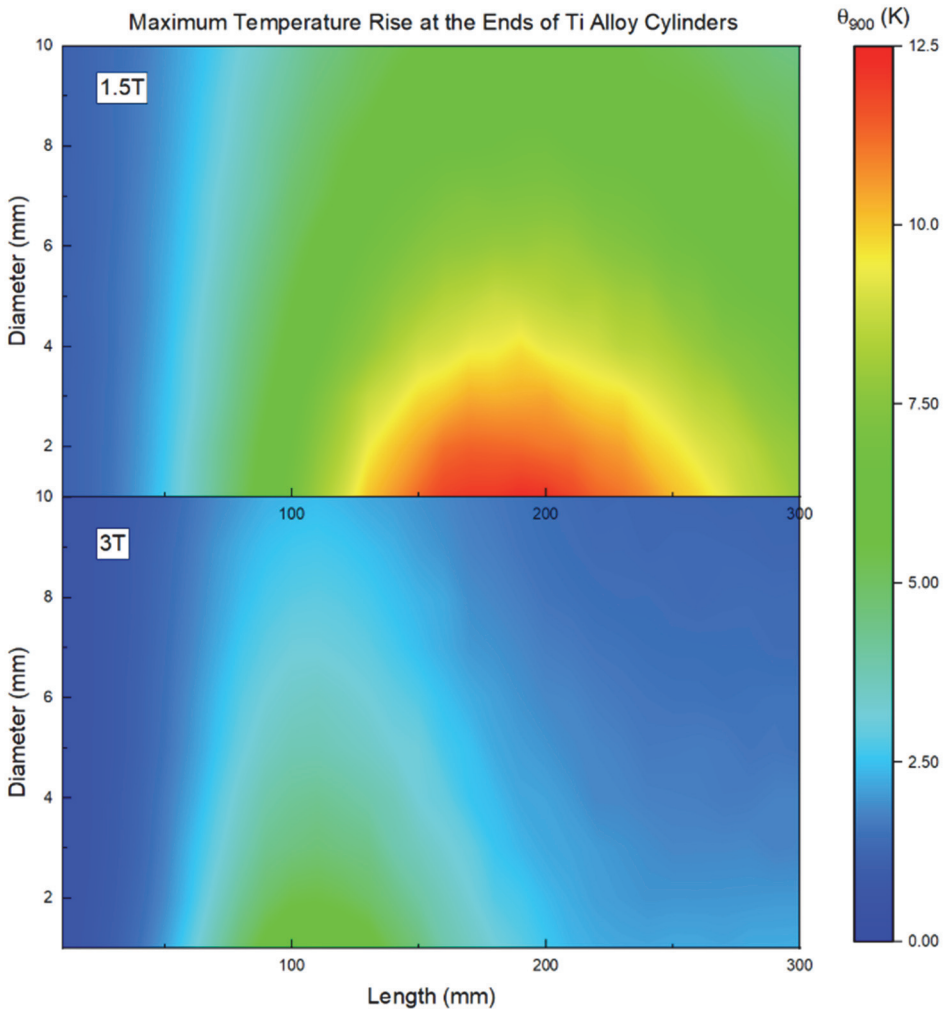

Figure 6: Maximum temperature rise after 900 s of RF power as a function of cylinder length and diameter. The upper plot is for a field of 1.5 T, the lower plot is for a field of 3.0 T.

A series of models of a titanium rod of diameter 5 mm and various lengths were calculated using the material properties in table 3 for the surrounding tissue using field strengths of 1.5 T and 3.0 T. Each set of models led to an identifiable peak value of SAR (as is shown in the left-hand plot of figure 7). The peak positions were obtained from bi-Gaussian fits for the peaks with enough data on the right hand side of the peak, or simple Gaussian fits for the

long wavelength materials. The associated resonant lengths were calculated from equation (2) for each set of tissue properties. The values from the COMSOL model results (vertical axis) and from equation (2) (horizontal axis) are shown in the right-hand plot of figure 7 with a $y = x$ line for comparison. The results are in reasonable agreement, given that the effects of radius on resonance behaviour will mean that equation (2) applies only to very thin wires.

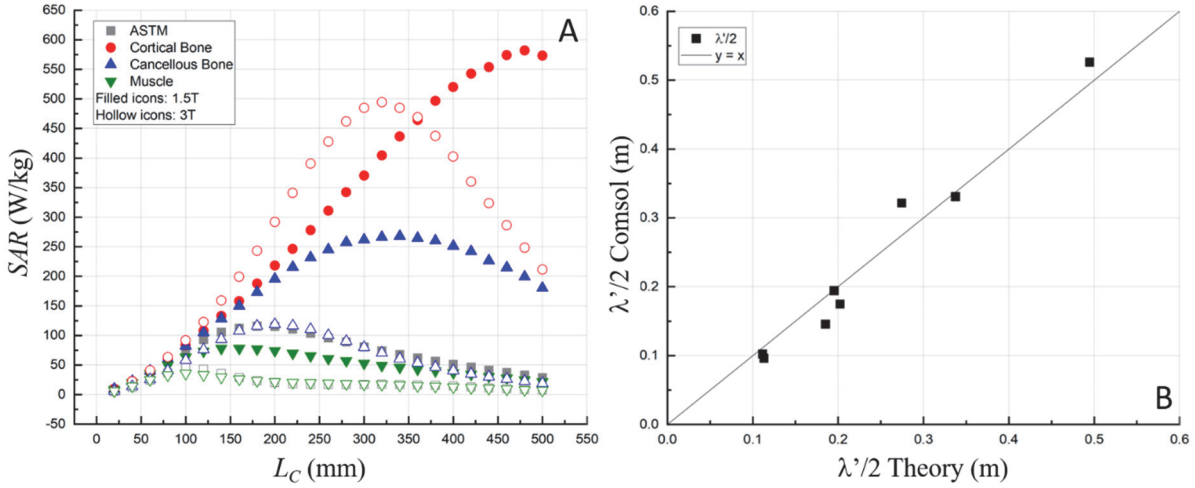

Figure 7: SAR for cylinders of diameter 5 mm in various tissue materials (left-hand plot) and a comparison between the resonant length calculated from equation (2) and resonant length extracted from the left-hand plot (right-hand plot).

The effects of the electrical conductivity of the implant were examined for a cylinder of 1 mm diameter and resonant length for fields of 1.5 T and 3.0 T in saline gel, using properties of titanium other than the electrical conductivity. The results are shown in figure 8, along with the results obtained for the same geometry with the material properties listed in table 2. Filled symbols relate to a field of 1.5 T and should be read from the left-hand axis; empty symbols relate to a field of 3.0 T and should be read from the right-hand axis. Figure 8 shows that the energy deposited increases monotonically with the electrical conductivity, but the difference in temperature rise for a conductivity of 0.1 MS m^{-1} and a conductivity of 10 MS m^{-1} is 6 % for a field of 1.5 T and 8 % for a field of 3.0 T, so the effect is secondary compared to (say) implant length when determining the heating.

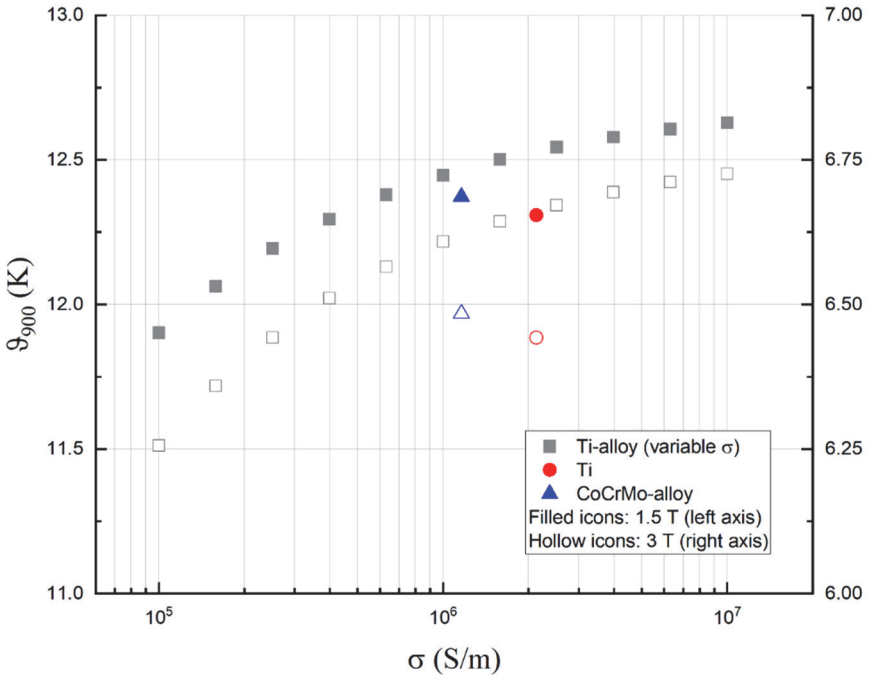

Figure 8: Maximum temperature rise after 900 s for a cylinder of 1 mm diameter and resonant length plotted against electrical conductivity. Filled symbols relate to a field of 1.5 T and should be read from the left-hand axis; empty symbols relate to a field of 3.0 T and should be read from the right-hand axis.

A series of models of cuboidal titanium plates were created. The plates were arranged with their long axis parallel to the field direction, and their width along the direction perpendicular to the nearest face of the phantom, see figure 9. The temperature distribution around the plates showed the maximum temperature rises occurring at the ends of the plate, in a similar way to the temperature distribution around the screws shown in figure 2. The effects of the material properties and orientation on the temperature rise are the same for the plates as for the cylinders. Figure 10 shows a complete set of temperature rise results after 900 s as a function of length, width and thickness for fields of 1.5 T and 3.0 T. The plots show the resonant behaviour seen in figure 6 for the cylinder models. The results also show that for a given implant length, increasing the dimension in the directions perpendicular to the length reduces the temperature rise.

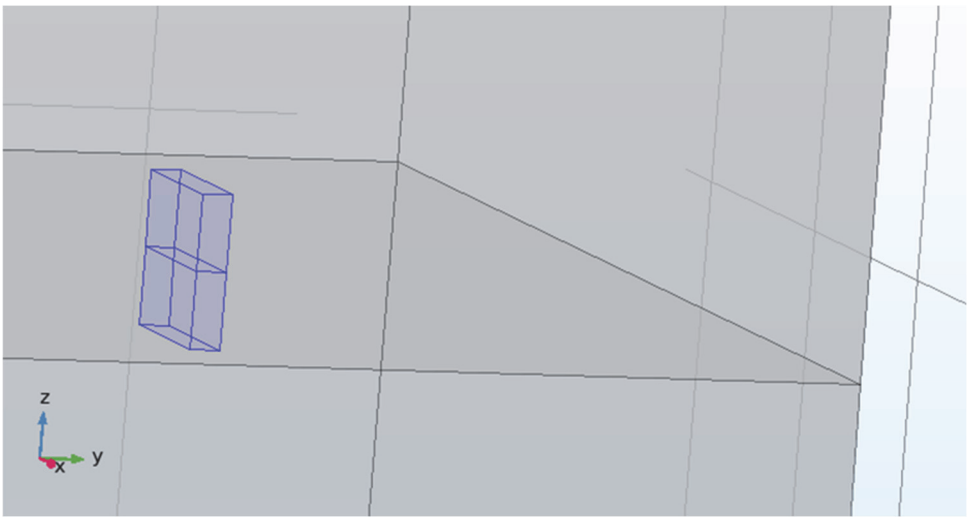

Figure 9: Orientation of a typical plate (blue) within the phantom (grey).

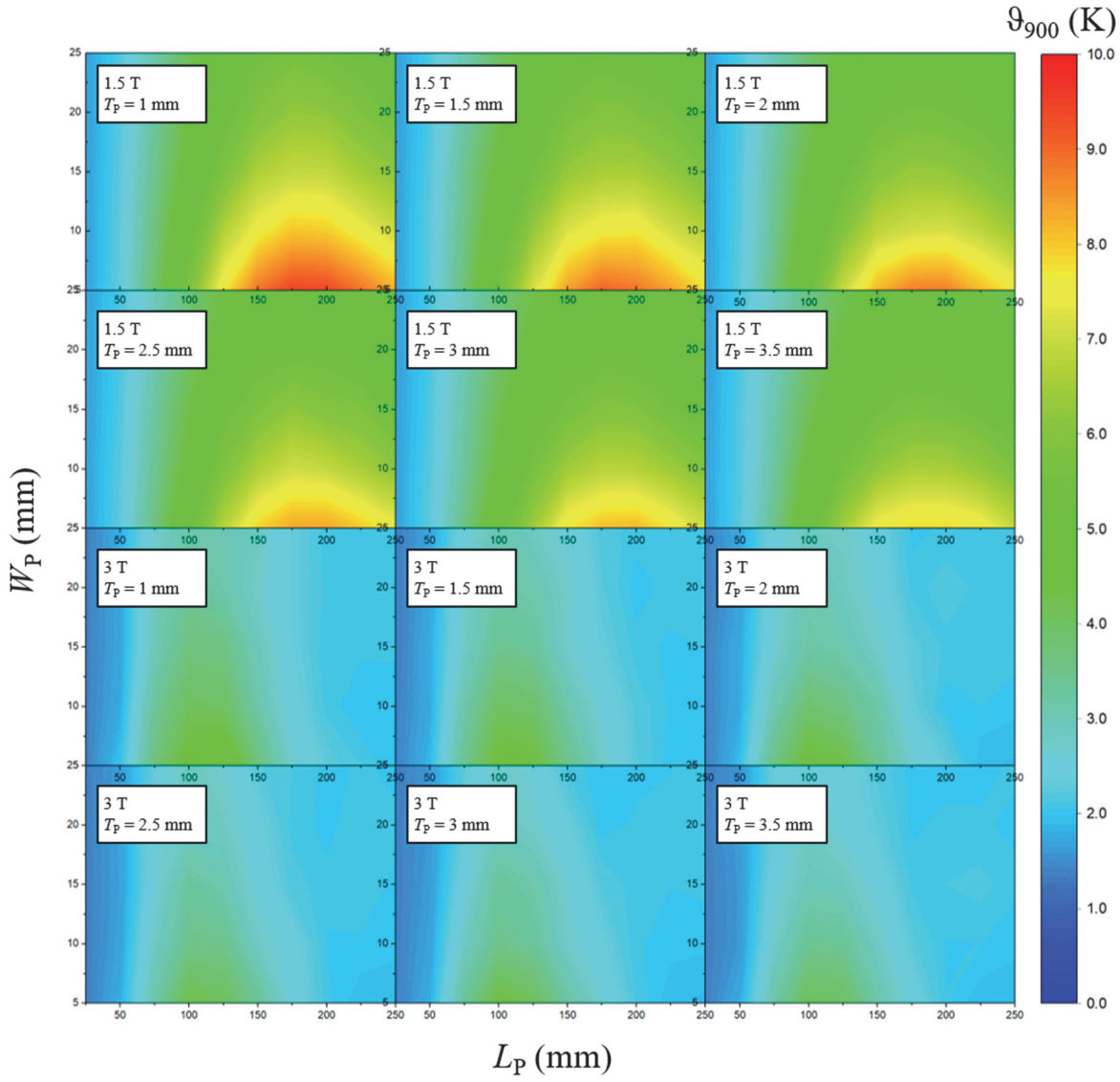

Figure 10: Temperature rise in the plate models after 900 s as a function of length L_p, width W_p, and thickness T_p.

2.3 MEASUREMENT OF RF-INDUCED HEATING OF PHANTOMS CONTAINING STRAIGHT RODS

A series of measurements of the temperature rise caused by exposing steel rods to RF heating was made. These measurements were compliant with the test method and requirements specified in ASTM F2182-11 (2011) [1]. A Zurich MedTech MITS1.5 64 MHz 16-rung high-pass birdcage coil was used to recreate the RF exposure conditions of a 1.5 T MRI scanner [6]. The coil has length 650 mm and inner diameter 700 mm and the length of the shield is 850 mm. The coil was excited in quadrature with a continuous wave signal at the resonant frequency (in the range 63 MHz to 65 MHz).

The titanium rods were flat-ended cylinders supplied by ZMT. Nine cylinders were measured in total, and the diameters and lengths of the cylinders are listed in table 5.

Table 5: Dimensions of cylinders used in the tests.

Length (mm)	Diameters (mm)
100	10, 3.2, 1
75	3.2, 1
50	3.2, 1
20	3.2, 1

RF induced heating tests were conducted with each rod submerged in the saline phantom gelled with polyacrylic acid (PAA), as specified by [1], within a Plexiglas tank model ZMI-ASTM2009. The phantom had dimensions of 65 cm by 42 cm by 9 cm and mass 24.4 kg. It was placed with its centroid at the isocentre of the RF coil as shown in Figure 11. Local heating during a 15-minute RF exposure was measured at three positions very close to the rod and one position remote from the rod using Luxtron STF or SFF series fast response immersion probes, labelled T1 to T4 in this report. The tests were then repeated without the rods to establish the local SAR at the measurement positions. Sufficient time was left between the tests for the system to return to thermal equilibrium. The phantom-averaged specific absorption rate (SAR) was measured by the calorimetric method described in [1] and using a saline phantom prior to the heating tests with the rods present. All equipment used for the tests was calibrated traceable to primary standards. The electrical permittivity and conductivity of the phantoms were measured prior to the tests.

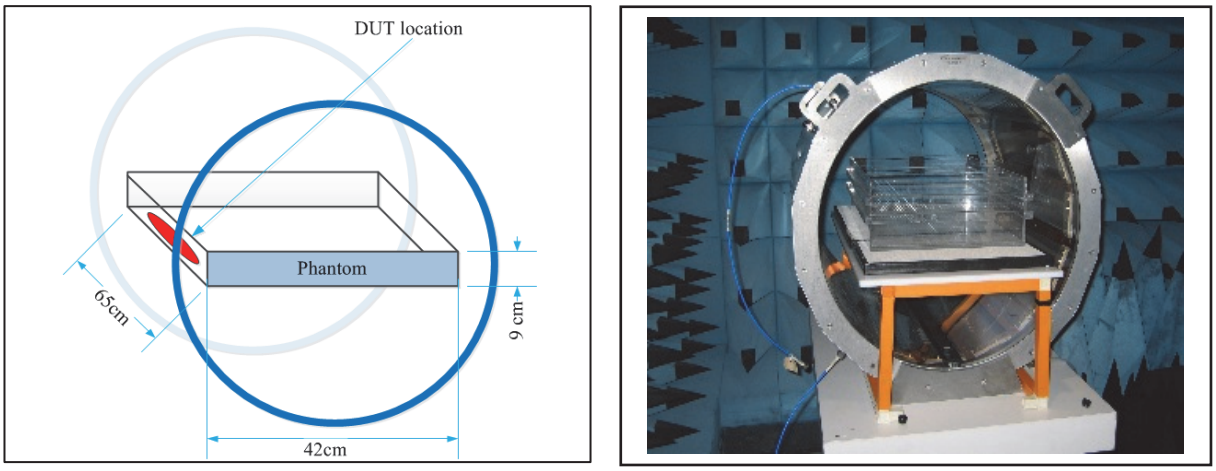

Figure 11: Location of the phantom in the RF coil. DUT ("Device Under Test") indicates the position of the rod.

The phantom-averaged SAR (WBSAR) was calculated using

$$\mathrm{WBSAR}\ (W/kg) = c_p\ \frac{\Delta T}{\Delta t}, \tag{5}$$

where c is the specific heat of the phantom and ΔT is the change in temperature during the exposure period of Δt seconds. A value of c_p = 4160 J/(kg K) was used in the calculation.

The local SAR was calculated using

$$\mathrm{SAR}\ (W/kg) = c_p\ m, \tag{6}$$

where m is the slope of the straight line fitted to the temperature against time data using least squares linear regression.

Both the phantom-averaged SAR and local SAR values are normalised to the average input power level during the heating tests with the DUT present.

The temperature rise was calculated as

$$\Delta T = T(15) - T(0), \tag{7}$$

where $T(15)$ is the temperature after 15 minutes of exposure, and $T(0)$ is the temperature immediately before the exposure. To reduce the effects of measurement system noise, temperature rises of less than or equal to 0.2 K were calculated using

$$\Delta T = \Delta t \times m, \tag{8}$$

where m was determined from the slope of a straight line fitted to the temperature against time data by linear regression. This approach reduces the effects of measurement noise on the result.

The rod was located with its axis aligned to the axis of the coil (corresponding to maximum E-field in the phantom) and positioned approximately centrally with respect of the depth and length of the phantom. Detailed measurements were taken of the distance of the rods from the edge and bottom of the phantom as the available sample holders affected positioning of the rods. The rod was supported using a plastic grid in the phantom. All supporting structures were at least 5 mm away from the measurement positions. The sensing part of T1 and T3 were placed as close as possible to within 0.5 mm of the ends of the rod and T2 was in direct contact with the rod close to its midpoint. T4 was used as the reference and located on the contralateral side of the phantom. The rods were placed between 2 cm and 4 cm from the face of the phantom, sufficiently far that the presence of the boundary is not expected to affect the heating. All temperature measurements had a 95 % confidence interval (k = 2) of ± 0.32 K. Table 6 shows the measured temperature rises for each experiment with and without the cylinder in place, and table 7 shows the difference between the temperature rise values with and without the cylinder.

Table 6: Temperature rises measured at each position in each test. The uncertainty associated with all temperature measurements is 0.32 K using a coverage factor of *k* = 2.

Length (mm)	Diameter (mm)	Cylinder	T1 temperature rise (K)	T2 temperature rise (K)	T3.0 Temperature rise (K)	T4 temperature rise (K)
100	10	Yes	4.5	1.31	5.19	1.65
100	10	No	1.15	1.2	1.22	1.69
100	3.2	Yes	9.83	1.19	9.05	1.59
100	3.2	No	1.59	1.53	1.49	1.63
100	1	Yes	8.64	1.12	11.32	1.78
100	1	No	1.58	1.67	1.49	1.56
75	3.2	Yes	6.11	1.21	6.05	1.84
75	3.2	No	1.43	1.48	1.45	1.65
75	1	Yes	7.92	1.52	6.15	1.75
75	1	No	1.72	1.99	1.71	1.69
50	3.2	Yes	4.32	1.72	4.08	1.49
50	3.2	No	1.74	1.7	1.64	1.52
50	1	Yes	5.27	1.89	4.32	1.36
50	1	No	1.74	1.7	1.64	1.52
20	3.2	Yes	1.98	2.14	2.3	1.53
20	3.2	No	1.5	1.7	1.73	1.53
20	1	Yes	2.08	2.27	2.46	1.31
20	1	No	1.77	1.83	1.99	1.26

Table 7: Difference between temperature rise with and without the cylinder present for each cylinder geometry

Length (mm)	Diameter (mm)	T1 temperature rise difference (K)	T2 temperature rise difference (K)	T3.0 Temperature rise difference (K)	T4 temperature rise difference (K)
100	10	3.35	0.11	3.97	-0.04
100	3.2	8.24	-0.34	7.56	-0.04
100	1	7.06	-0.55	9.83	0.22
75	3.2	4.68	-0.27	4.6	0.19
75	1	6.2	-0.47	4.44	0.06
50	3.2	2.58	0.02	2.44	-0.03
50	1	3.53	0.19	2.68	-0.16
20	3.2	0.48	0.44	0.57	0
20	1	0.31	0.44	0.47	0.05

The results in table 7 are consistent with expectations based on physical understanding: it is expected that the majority of the heating occurs at the ends of the cylinder (measurements point T1 and T3), and that the temperature rise at the two ends should be approximately equal, as is observed. The measurement point T4 is sufficiently far from the cylinder that the temperature measurements should be unaffected by the presence of the cylinder, as is seen in the results.

Simulations of the RF heating within the calibration cylinders were constructed in COMSOL Multiphysics, following the methodology used in section 2.2.1, with the birdcage coil dimensions adjusted to match those of the experimental set up described above. Technical drawings of the exact location of each cylinder within the phantom were used to set the position of the cylinder within the model. Measurements of local SAR at positions T1, T2 and T3 without the cylinder present were used to adjust the input voltage on the simulated coil to achieve the measured results; once this calibration was completed the simulation was run once more setting the cylinder to have the material properties of steel (see table 2).

Plots of the simulated temperature distributions around the ends of each of the calibration cylinders are shown in figure 12. The effects of uncertainty in positioning the temperature sensor were considered by evaluating the minimum and maximum temperature amongst all points that lie 1 mm from the centre of the end of the cylinder, and repeating the calculation for distances of 2 mm and 3 mm so that for each rod, three temperature ranges related to an offset of the temperature sensor from the end of the rod were obtained. Figure 13 shows the measured temperature rises for each rod (with a 95 % coverage interval) on the left hand side of each plot, and the temperature ranges obtained at 1 mm, 2 mm, and 3 mm from the end of the rod. Two thirds of measurements are within the temperature ranges obtained from the simulations for the 1 mm spheres, increasing to 94% at 2 mm and 100% at 3 mm. Hence if a positioning accuracy of better than 3 mm is assumed, the models can be considered as validated.

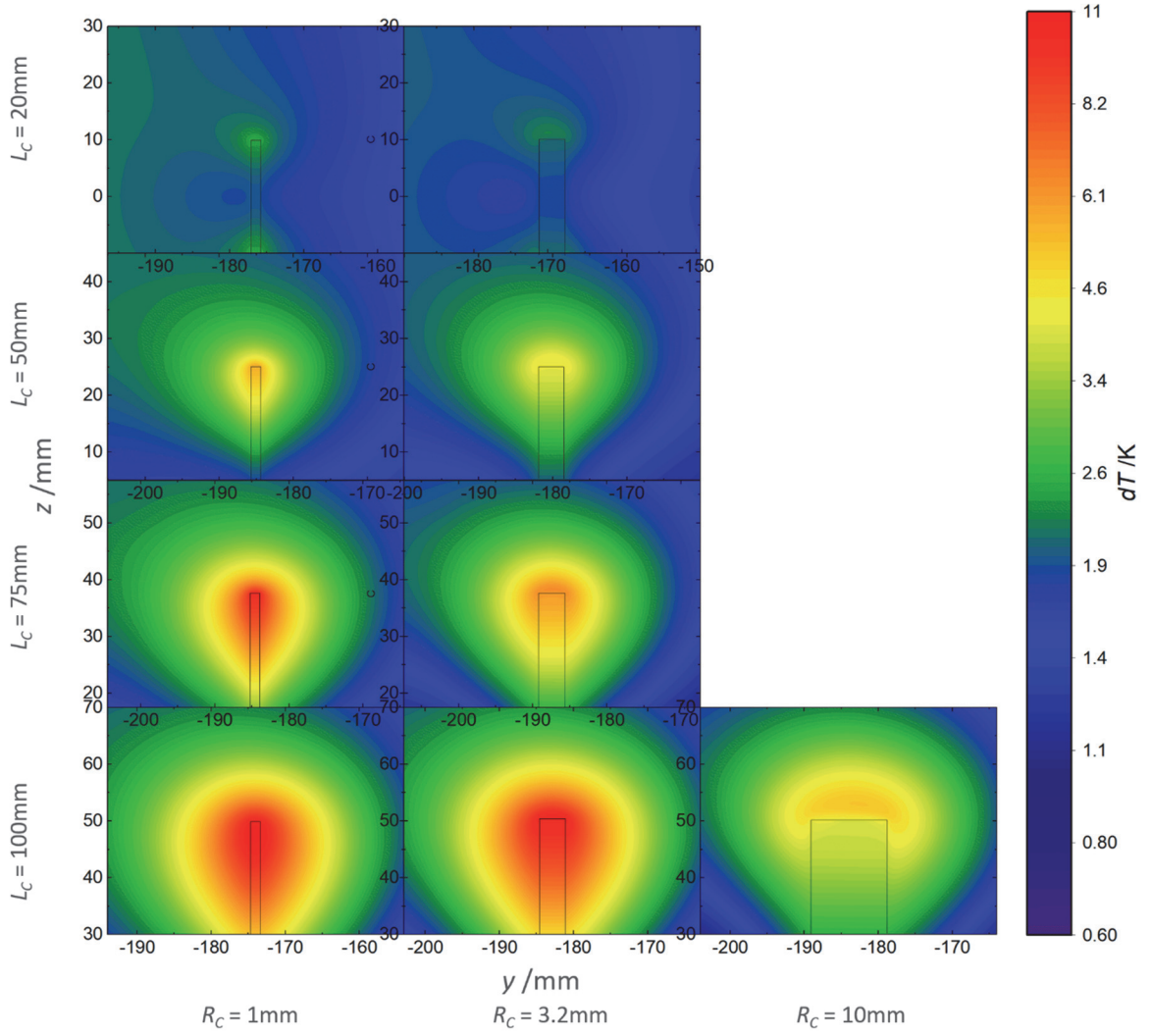

Figure 12: Simulated temperature profiles around the ends of the steel calibration cylinders. Note the colour axis has been ln2 scaled in order to visibly differentiate the temperature ranges in each subplot. The subplots are ordered by cylinder length, L_C, and cylinder radius, R_C.

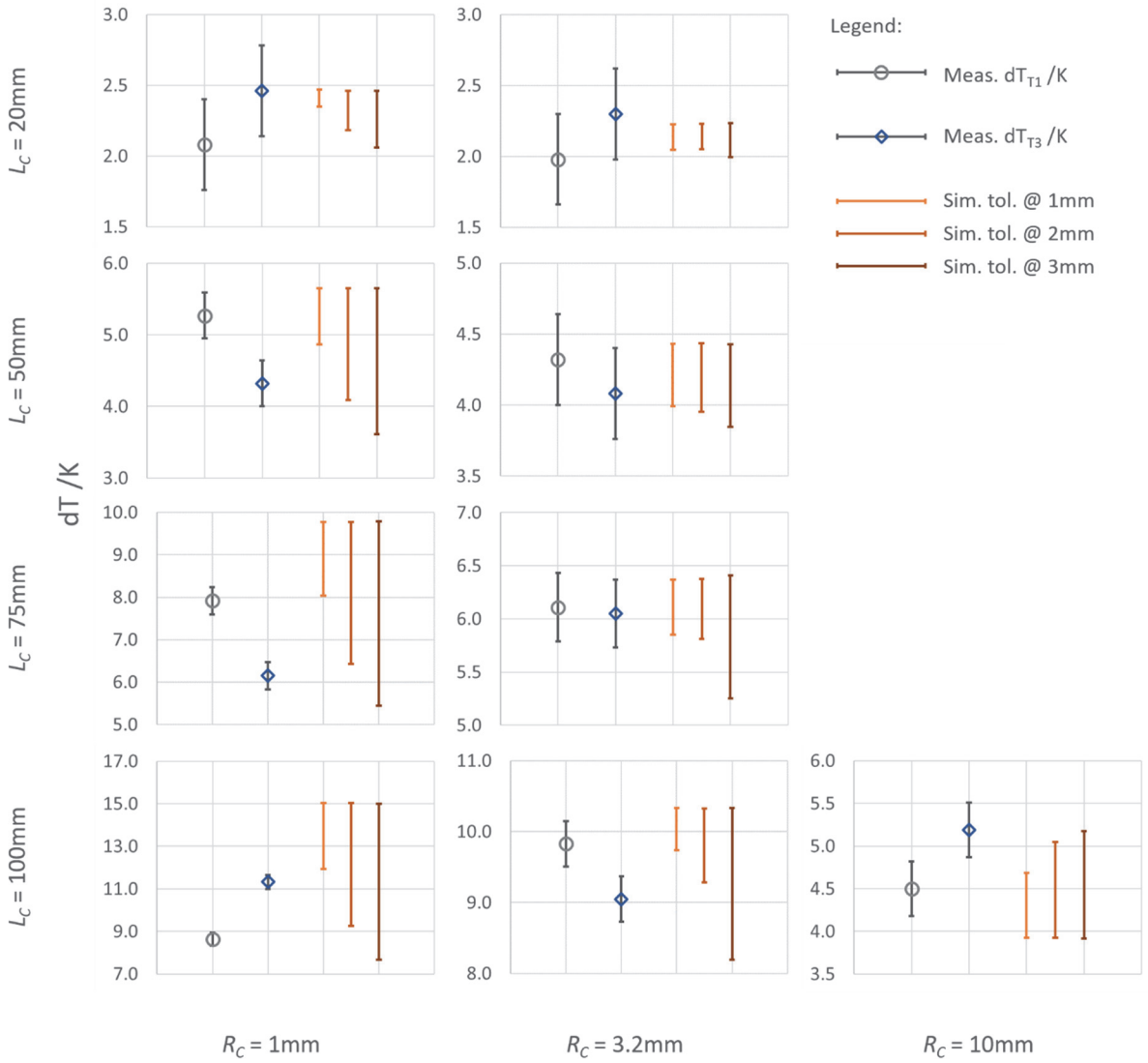

Figure 13: Measured temperature rises at the top (T1) and bottom (T3) of the steel calibration cylinders plotted as grey circles and blue diamonds respectively, with the estimated uncertainty (k=2) of 0.32 K. Maximum and minimum simulated temperatures within a sphere of radius 1 mm, 2 mm and 3 mm away from the cylinder ends are displayed alongside the measurement values. The subplots are ordered by cylinder length, L_C, and cylinder radius, R_C.

Whilst there is overall a very good agreement between the measurement and simulation results, it is clear that the temperature sensors must be aligned with the device under test (DUT), at the positions known to give the largest heating values, to extremely tight tolerance levels in order to obtain an accurate measure of implant heating. In practice this can often be difficult to achieve whilst removing and/or inserting the DUT within the semi-opaque gel without disturbing the temperature sensor positions, especially in the case of DUTs with complex geometries. Figure 14 shows the thermal gradients within the phantom gel at positions up to 5 mm from the cylinder end for the 100 mm long 1 mm diameter cylinder, with gradients of up to 4 K mm^{-1} close to the cylinder tip. This plot shows that it can be very easy to miss 'hot spots' within implant heating safety testing procedures, especially in the cases where adequate modelling has not been performed prior to the measurement procedure to determine the hot spot location, and particularly in the cases of implants which have long, thin wire-like components that are oriented along the length of the MRI coil.

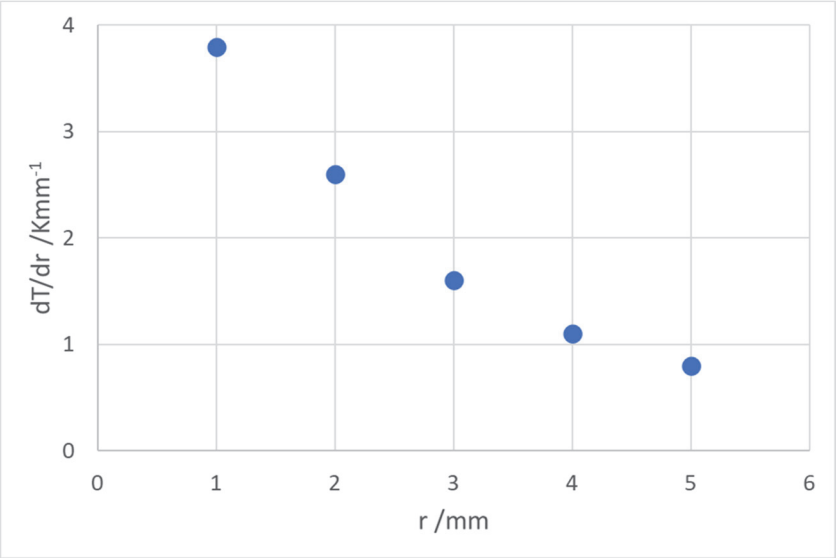

Figure 14: Thermal gradient as a function of distance from the cylinder tip (L_C = 100 mm, R_C = 1 mm).

2.3.1 Measurement and modelling of real small implants

A set of three additional measurements, using the procedure described above, were made of a set of small implants. The implants were a Valgus osteotomy plate, a Titan osteotomy plate, and a Blount staple. The geometry of the implants was measured using a coordinate measuring machine, and the resulting data was converted into an STL representation of each implant. These representations proved to be too noisy to mesh within COMSOL, so instead the shape and dimensions were used to develop suitable geometries by hand in a form that could be meshed. Figure 15 shows a photograph, the STL representation, and the final geometry for each implant.

Figure 15: A photograph, the STL representation, and the final geometry for three implants measured and modelled undergoing RF exposure.

Figure 16 shows a comparison between the measured and simulated temperatures for each implant. Two of the temperature sensors were placed close to the extremities of the implants and the third was placed near to the centre. The locations of the sensors are indicated by black symbols on the coloured contour plots in figure 16. The symbol shape corresponds to the symbol used in the adjacent graph comparing measured (black symbols) and simulated

(orange symbols) temperature rises. The error bars on the measured values are a 95 % coverage interval; the error bars on the simulated values are the minimum and maximum temperature within a 1 mm sphere surrounding the expected sensor location. In all cases the measurements and simulated values are consistent, giving further confidence in the simulation technique.

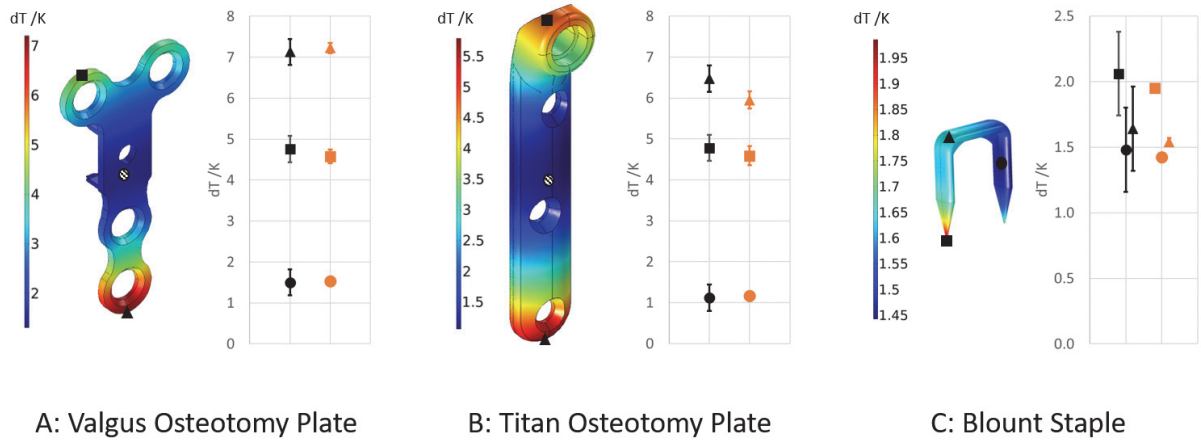

Figure 16: Distribution of temperature rise after 900 s (colour contours) and comparison between measured (black symbols) and predicted (orange symbols) temperature rises for the three implants.

2.4 PARAMETRIC MODELS FOR RF HEATING

A set of parametric models was constructed based on the results of the COMSOL models described in section 2.2 above. The parameters used were restricted to the geometric quantities as insufficient results were available for reliable inclusion of material properties and other such quantities. The data used in the fits was restricted to implant lengths of less than 100 mm, as per the original protocol for the project. Initial attempts to fit the full range of lengths proved unsuccessful. The cylinder models used every possible combination of:

- Lengths between 10 mm and 100 mm, inclusive, in steps of 10 mm;
- Diameters between 1 mm and 10 mm inclusive, in steps of 1 mm.

The cuboidal models used every possible combination of:

- Lengths between 25 mm and 100 mm, inclusive, in steps of 25 mm;
- Widths between 5 mm and 25 mm inclusive, in steps of 5 mm;
- Thicknesses between 1 mm and 3.5 mm, inclusive, in steps of 0.5 mm.

Polynomial models were used throughout. These are purely empirical models, but since the models results in section 2.2 suggest that the dependence of temperature rise on geometric quantities is smooth and continuous, they are a reasonable choice. In general, the guidance in ISO/TS 28038 [7], the ISO Technical Specification for determination and use of polynomial calibration functions was followed, with some extensions applied to allow for multivariate models. Chebyshev polynomials were used throughout as they offer superior stability and the coefficients in the Chebyshev polynomial expansion show more clearly which of the terms are more important and which are less significant than the coefficients associated with powers of unscaled variables.

The polynomials were fitted directly to the raw model results. Unweighted least-squares approximation was used to estimate the coefficients of the polynomial in each case. In all cases the root mean square residuals (RMSR) were calculated and were used to select the best-fitting model, using the assumption that the uncertainty on the simulated values was of

the order of 0.06 K. This uncertainty value was obtained by using variable and fixed meshes to calculate the temperature rise of a cylinder simulated in COMSOL Multiphysics, and taking uncertainty to be the average of the absolute difference between the two. Optimal fits were then selected to be those whose RMSR values approached 0.06 K whilst having an order close to or lower than $\sqrt{2m}$ in a given dimension, where m was the number of data points available in that dimension.

The simulations of cylinders were fitted with 2D polynomials using length and diameter as the control variables. The best fits obtained using the above criteria may be seen in figure 17 for simulations using a field of 1.5 T and of 3.0 T. The fits provide reasonable estimates in the ranges investigated, though it can be seen that as the length increases, the fits appear to become less accurate. Fits for the 3.0 T data require a higher degree to achieve a similar RMSR, which is likely to be caused by a more pronounced variation in the shape of the curve.

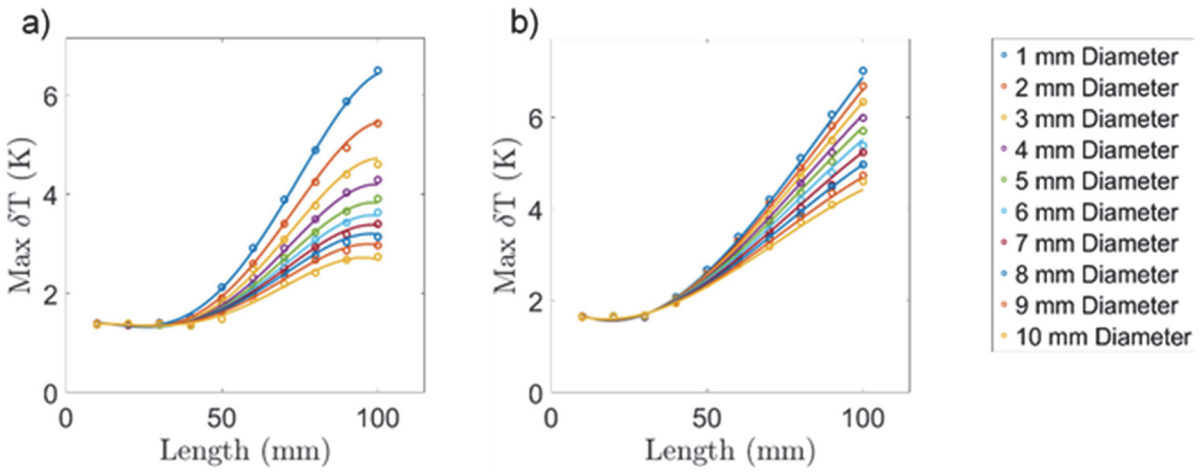

Figure 17: Parametric models for cylinder heating after 900 seconds. Each figure shows the projection of a 2D fit onto a single plane. a) Temperature rise for a field of 1.5 T. The model has a degree of 1 for diameter and 3 for length. The RMSR is 0.06 K. b) Temperature rise for a field of 3.0 T. The model has a degree of 3 for diameter and 4 for length. The RMSR is 0.06 K.

The results of the models of cuboids were fitted with 3D polynomials, using length, thickness and width as control variables. The best fit results to the cuboid data are shown in Figure 18 and Figure 19 for fields of 1.5 T and 3.0 T respectively. As was the case for the cylinders, larger lengths were more poorly fitted, and fits for a 3.0 T field required a higher degree to achieve a similar, or indeed poorer RMSR. For the results with a field of 3.0 T an RMSR of 0.06 K was only possible with even higher degrees than those selected, which leads to overfitting, so the fit shown is the best fit that is consistent with the requirement that the order be less than or equal to $\sqrt{2m}$.

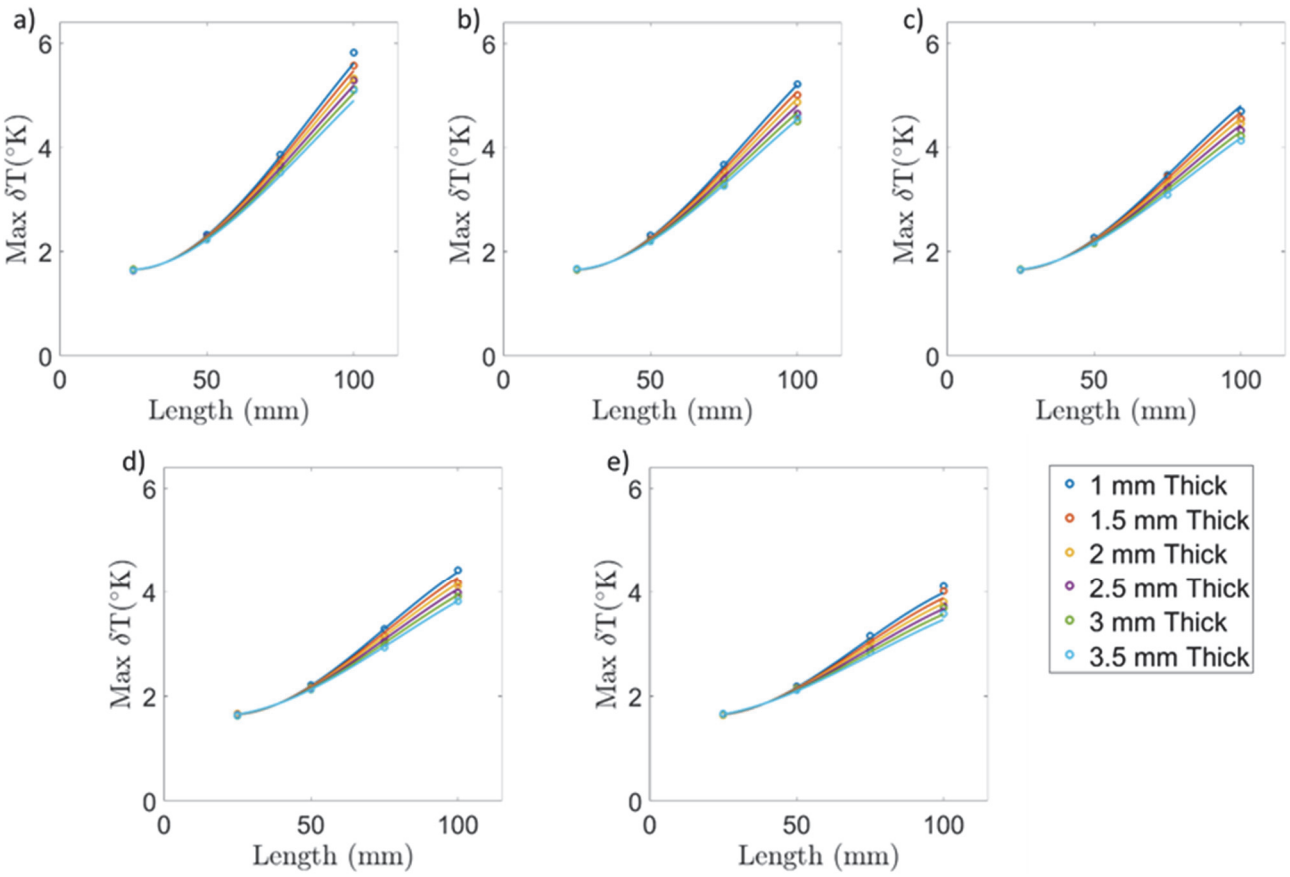

Figure 18: Parametric models for cuboid heating after 900 seconds in a 1.5 T field. Each figure shows a slice of a projection of a 3D fit onto a single plane for a width value of a) 5 mm b) 10 mm c) 15 mm d) 20 mm e) 25 mm. This model has a degree of 1 in thickness, 1 in width and 3 in length, for an RMSR of 0.06 K. The legend is shared for all subfigures.

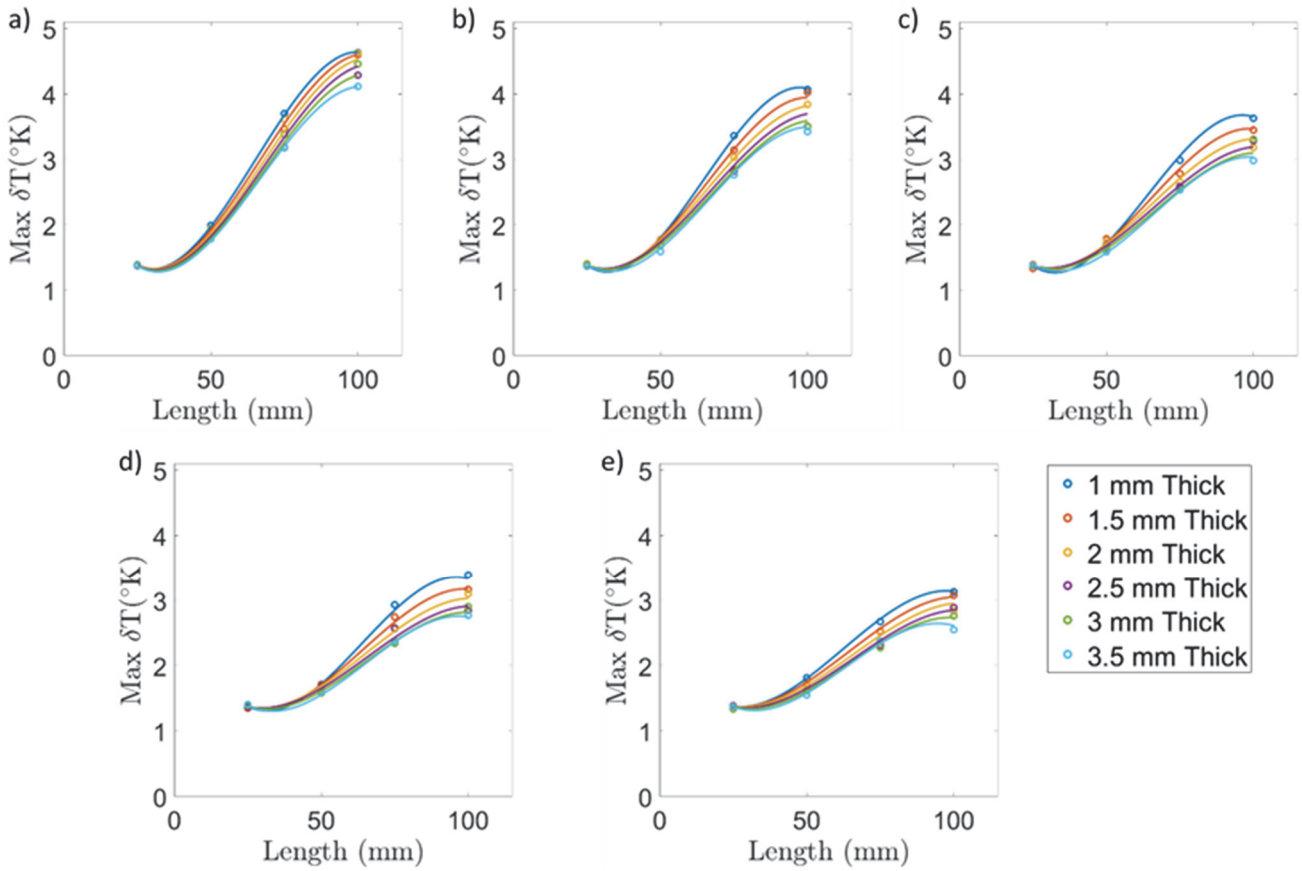

Figure 19: Parametric models for cuboid heating after 900 seconds in a 3.0 T field. Each figure shows a slice of a projection of a 3D fit onto a single plane for a width value of a) 5 mm b) 10 mm c) 15 mm d) 20 mm e) 25 mm. This model has a degree of 2 in thickness, 2 in width and 3 in length, for an RMSR of 0.07 K. The legend is shared for all subfigures.

Table 8 gives the coefficients for the best fit polynomial approximation to the cylinder data obtained using a field of 1.5 T. This polynomial was of order 1 in diameter and of order 3 in length and had an RMSR of 0.06 K. The coefficients are labelled with two subscripts. The first subscript (generally *i*) denotes length and the second (generally *j*) denotes diameter. Each column of the table contains coefficients that are associated with polynomials that are of the same order in length, and each row contains coefficients that are associated with polynomials that are of the same order in diameter. So for instance the coefficient that is associated with the polynomial of order 1 in diameter and 2 in length is denoted a_{21} and is in the third column (headed a_{2j}) and the second row (labelled a_{i1}).

The use of Chebyshev polynomials means that values of the coefficients are normally higher in the top left hand corner and decrease towards the bottom right hand corner. Values lower than the target RMSR typically indicate coefficients of little significance, and can if present in abundance indicate an overfit.

Table 8: Coefficients of the best fit polynomial for cylindrical data using a field of 1.5 T. The first suffix denotes order of the polynomial in length, and the second the order of the polynomial in diameter. Note that the coefficients are associated with Chebyshev polynomials.

	a_{0j}	a_{1j}	a_{2j}	a_{3j}
a_{i0}	3.20	2.13	0.46	-0.13
a_{i1}	-0.42	-0.62	-0.20	0.01

Table 9 shows the same information for the cylinder data at 3.0 T, where the best fit was of order 3 in diameter and 4 in length and had an RMSR of 0.06 K.

Table 9: Coefficients of the best fit polynomial for cylindrical data using a field of 3.0 T. The first suffix denotes order of the polynomial in length, and the second the order of the polynomial in diameter. Note that the coefficients are associated with Chebyshev polynomials.

	a_{0j}	a_{1j}	a_{2j}	a_{3j}	a_{4j}
a_{i0}	2.46	1.54	0.39	-0.18	-0.09
a_{i1}	-0.63	-0.9	-0.26	0.06	0.04
a_{i2}	0.16	0.22	0.06	0.00	-0.01
a_{i3}	-0.07	-0.09	-0.02	0.00	0.00

The fits to the cuboids have three control variables and so the coefficients are more complicated to present in tabular form. The best fit found for the 1.5 T data was of order 3 in length, 1 in width, and 1 in thickness and had an RMSR of 0.06 K. The best fit for the 3.0 T data was of order 3 in length, 2 in width, and 1 in thickness and had an RMSR of 0.07 K. Tables 10 and 11 give the coefficients for the best fit polynomials to the 1.5 T and 3.0 T data respectively. The coefficients are labelled with three suffixes. The first relates to length, the second to width and the third to thickness. Each row gives the coefficients associated with all orders of length for fixed orders of width and thickness.

Table 10: Coefficients of the best fit polynomial for cuboidal data using a field of 1.5 T. The first suffix denotes order of the polynomial in length, the second the order of the polynomial in width, and the third the order of the polynomial in thickness. Note that the coefficients are associated with Chebyshev polynomials.

	a_{0j0}	a_{1j0}	a_{2j0}	a_{3j0}
a_{i00}	2.89	1.48	0.18	-0.06
a_{i10}	-0.28	-0.4	-0.1	0.01

	a_{0j1}	a_{1j1}	a_{2j1}	a_{3j1}
a_{i01}	-0.13	-0.17	-0.03	0.01
a_{i11}	0.02	0.02	0.01	0

Table 11: Coefficients of the best fit polynomial for cylindrical data using a field of 3.0 T. The first suffix denotes order of the polynomial in length, the second the order of the polynomial in width, and the third the order of the polynomial in thickness. Note that the coefficients are associated with Chebyshev polynomials.

	a_{0j0}	a_{1j0}	a_{2j0}	a_{3j0}
a_{i00}	2.34	1.22	0.09	-0.17
a_{i10}	-0.33	-0.44	-0.06	0.05
a_{i20}	0.08	0.09	0.01	0.00

	a_{0j1}	a_{1j1}	a_{2j1}	a_{3j1}
a_{i01}	-0.16	-0.17	0.01	0.02
a_{i11}	0.01	0.01	-0.01	-0.01
a_{i21}	0.01	0.03	0.00	-0.02

3 PARAMETRIC ANALYSIS OF FACTORS AFFECTING GRADIENT INDUCED HEATING OF IMPLANTS

3.1 RELEVANT PARAMETERS

The broad classes of parameter identified were:

- Coil and scan sequence used
- Properties of the implant material
- Properties of the surrounding tissue
- Geometrical parameters
- Field orientation

MRI scanners in current use have a wide variety of gradient coils and use a number of different clinical sequences. The work in this work package has focussed mainly on small implants, although some larger orthopaedic implants have been considered. The implants are sufficiently small that the type of gradient coil will have no effect on the electromagnetic fields in the implant, so this aspect has not been considered in the analysis.

The scan sequences have been approximated by a continuous repetition of a trapezoidal waveform shown in figure 20. This shape can be described using three parameters: G (the gradient amplitude), $t_s/2$ (the rise time) and t_{dwell} (the dwell time). The value of G has been fixed at 23 mT/m for all simulations, which is approximately the flux density gradient that would be expected at hip level for an adult in a typical toroidal MRI scanner with a central bore. The electromagnetic fields are linearly dependent on G, so the expected power or temperature rise at any other field G_0 can be calculated by multiplying by a factor of $(G_0/G)^2$.

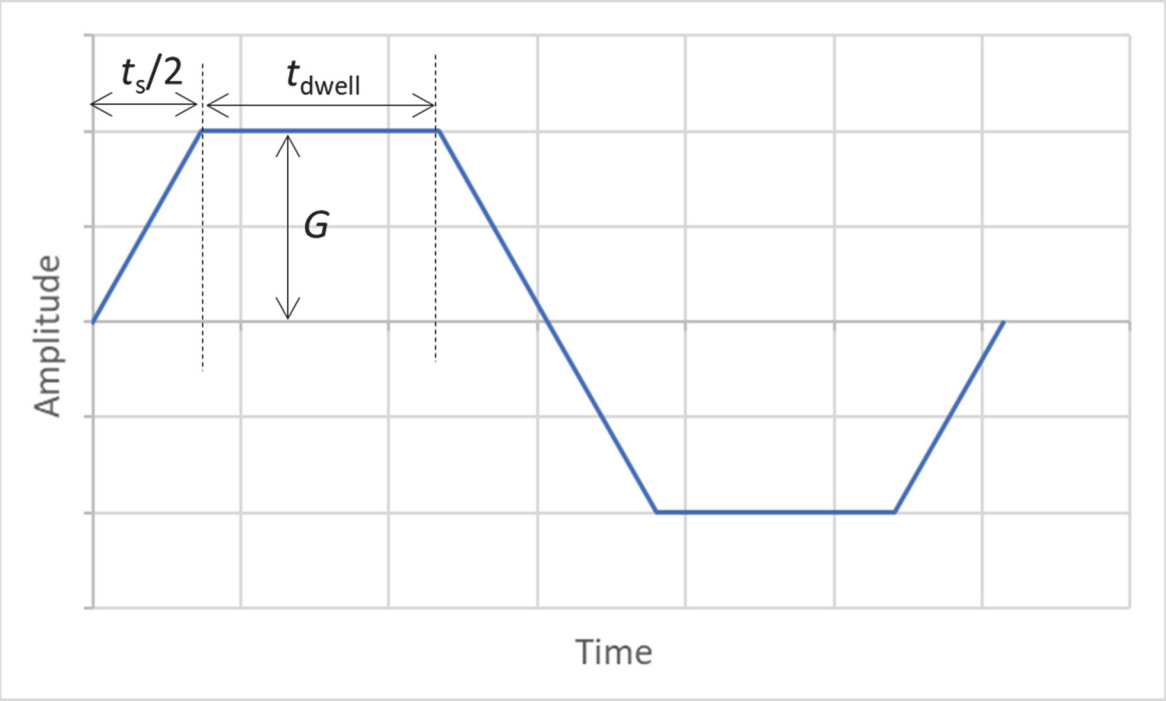

Figure 20: Trapezoidal waveform and associated parameters

Ten signals have been defined using different values of $t_s/2$ and t_{dwell}, and the values of each pair of parameters are listed in table 12. Table 12 also shows the value of f, the fundamental frequency of the scan (i.e. $1/T$ where T is the total duration of the signal, equal to $2(t_s + t_{dwell})$), and the thermal stress index

$$I_s = \sqrt{\frac{1}{T}\int_0^T \left(\frac{dG}{dt}\right)^2 dt}, \tag{9}$$

where *G* is the gradient of applied magnetic flux density. If skin effects are neglected and the electric field is assumed to respond to the flux variation instantaneously, this index is proportional to the average power deposited by the scan.

Table 12: Scan sequence parameters used in the study.

Sequence code	$t_s/2$ (ms)	t_{dwell} (ms)	Thermal stress index I_s (T ms^{-1})	Fundamental frequency f (Hz)
SEQ1	0.147	0.32	110.6	815
SEQ2	0.500	0.32	40.9	379
SEQ3	0.147	1.00	76.2	386
SEQ4	0.100	0.32	145.8	962
SEQ5	0.300	0.32	63.2	543
SEQ6	0.147	0.00	159.9	1695
SEQ7	0.147	3.00	47.8	152
SEQ8	0.100	0.25	156.7	1111
SEQ9	0.500	3.00	27.5	125
SEQ10	3.000	4.00	13.5	50

Four implant materials were considered in the work, using the same properties as were listed in table 2. The electromagnetic properties are characterised by a conductivity only, assuming the permittivity to be equal to 1.0 (which is reasonable for these metals).

Four different surrounding materials were used in the work, with thermal properties as shown in table 3 above. The gradient coil MRI fields are such that only the energy deposited in the implant needs to be calculated, so the surrounding materials do not need to have electromagnetic properties defined. The materials that model human tissue included a source term of the form

$$C_{\mathrm{perf}}(T - T_b), \tag{10}$$

where T is the temperature, C_{perf} is the perfusion coefficient in W m^{-3} K^{-1} and T_b is the blood temperature (fixed at 310.15 K), in the transient heat equation to simulate the heat transfer due to perfusion. The values of the perfusion coefficient used in the gradient coil models are listed in table 13 (gel has no perfusion so perfusion was not modelled and no value is quoted in the table). See section 5.2 for more discussion of the effects of perfusion.

Table 13: Properties of surrounding materials.

Material	Perfusion coefficient (W/(m^3 K))
Muscle	2699
Cancellous bone	1207
Cortical bone	7468

Several different implant geometries were considered. A set of parameterised spheroidal models were constructed to understand the effects of shape, volume and field orientation in detail. These models had vertical semi-axes ranging from 5 mm to 120 mm, and horizontal semi-axes ranging from 5 mm to 40 mm. Smaller sets of models were run to simulate screw and plate behaviour (geometric details are given in the next section), and a number of models of realistic implant geometries were run.

3.2 SENSITIVITY OF GRADIENT FIELD INDUCED HEATING TO PARAMETERS

3.2.1 Model overview

The thermal heating due to the GC field was evaluated by computing (a) the distribution of the power density within the implant consequent to the interaction between the magnetic field and the metallic object and (b) the subsequent heating of the metallic object and thermal diffusion within a rectangular gelled saline phantom in a similar construction to ASTM F2182 [1] (which is not used for GC heating).

The implant and the surrounding phantom were discretized into homogeneous cubic voxels of given electrical and thermal properties. For step (a), the electromagnetic problem was conveniently limited to the region of the metallic objects, assuming that induced currents and related power deposition are confined within the implant at the low frequencies of the GC field. In order to account for the complex time evolution of realistic sequences, the approach proposed and validated in [8] was adopted. The time waveforms of the magnetic field signals were decomposed into truncated Fourier series. For each signal the related electromagnetic problem, which involves the field reaction caused by induced currents, was solved in the frequency domain using the hybrid Finite Element/Boundary Element solver described in [9] and [10]. Finally, the induced currents and the powers deposited in each voxel were evaluated.

For step (b), the thermal problem generated by the power deposition in the metal was solved in the whole domain (metallic object and phantom) using Pennes' bioheat equation in terms of the temperature elevation ΔT after time t with respect to the initial temperature T_0. Robin boundary conditions were set on the external surface of the phantom to account for the heat exchange with the ambient atmosphere. The bioheat equation was numerically solved by a finite difference method (FDM) using a Douglas-Gunn (DG) time split scheme, which allows for an efficient parallel implementation on graphics processing units (GPUs) [11].

3.2.2 Results

The power deposited in an implant by an MRI scan due to the gradient coils, P, is caused by the formation of eddy currents within the implant. These eddy currents depend on the gradient of the field strength of the scanner at the location of the implant (B_G); the electromagnetic properties and detailed geometry of the implant, captured in a factor k_p; the time-dependent behaviour of the scan sequence which can be captured in I_s as defined above; and a factor $\beta \leq 1$ capturing the effects of orientation of the implant to the magnetic field. These effects have been combined as

$$P = k_p B_G^2 f(I_s)\beta, \tag{11}$$

based on the assumption that the effects of each factor can be considered as independent, and for the heating an extra set of parameters Θ are required that include the thermal properties of the surrounding tissue and the implant and the heat transfer between the two, so that the temperature rise ΔT (either maximal or at some specified time) can be written as

$$\Delta T = g(P, \Theta), \tag{12}$$

for some function g. Each of these aspects will be discussed separately. The dependence on B_G is known analytically to be dependent on the square of the magnetic field magnitude.

The dependence of P on I_s (defined in equation (9)) has been calculated for all implant geometries for worst case orientations of the plates. Figure 21 shows a logarithmic plot of deposited power against I_s for a selection of small plates and grids. Fitting a straight line to

these data showed that P is proportional to I_s^2. This square law holds for plates with holes and mesh-like implants as well as simple cuboids. The exponent of the dependence is seen to decrease as the implant volume increases (i.e. the dependence becomes I_s^n where n<2). It is believed that this decrease is due to skin effects: a similar effect is seen with an increase in electrical conductivity of the implant material.

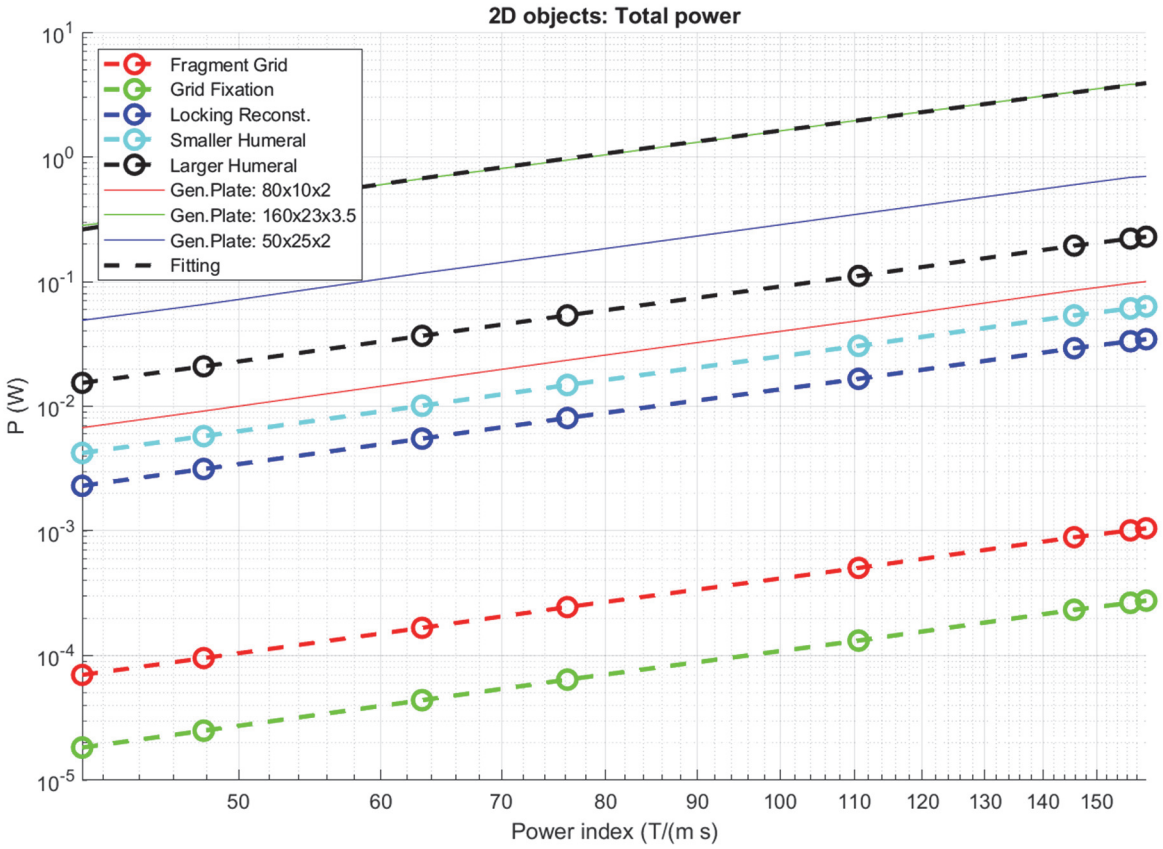

Figure 21: Deposited power plotted against I_s for a selection of small implants.

The simulated objects can be split into two broad groups: 2D objects, which have one dimension much smaller than the other two, and 3D objects which do not. The power deposited in the two groups of objects will have different geometric dependencies. The value of k_p was calculated from a rearrangement of equation (11) based on the largest deposited power, so that β = 1, and taking $f(I_s) = I_s^2$. Figure 22 shows a plot of the value of the coefficient k_p against volume for the 3D objects (spheroids, screws, and large orthopaedic implants), using a logarithmic scale on both axes. The plot shows that there is a strong correlation between implant volume and k_p.

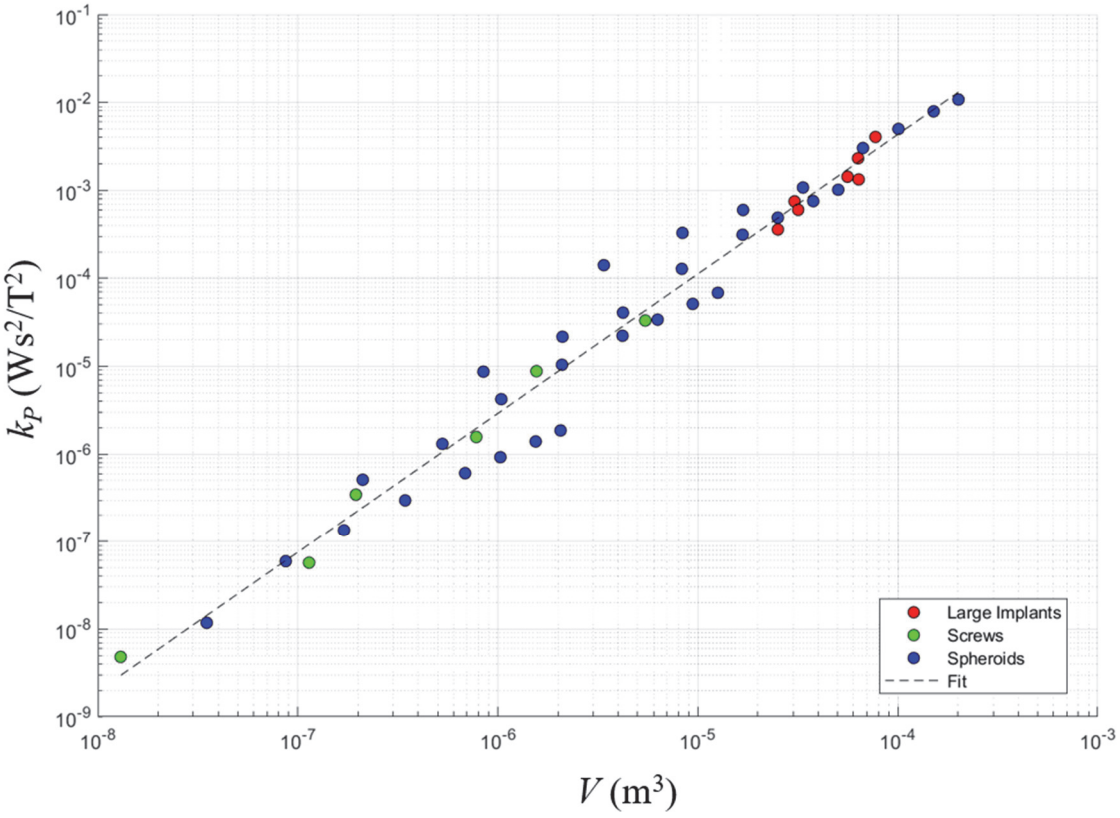

Figure 22: Effect of implant volume on k_p.

The 2D objects (plates, including realistic implant shapes) show the highest deposited power when the axis of the field is perpendicular to the largest surface area of the plate. The dependence of the value of k_p/d (where d is the thickness of the plate) calculated from this maximum power on the cross-sectional area S and the plate aspect ratio is shown in figure 23. Qualitative trends are visible, in particular the value of k_p increases with the area S for a fixed aspect ratio and decreases with aspect ratio for a fixed value of S. The cause of this behaviour is not immediately obvious, but may provide direction for further investigation.

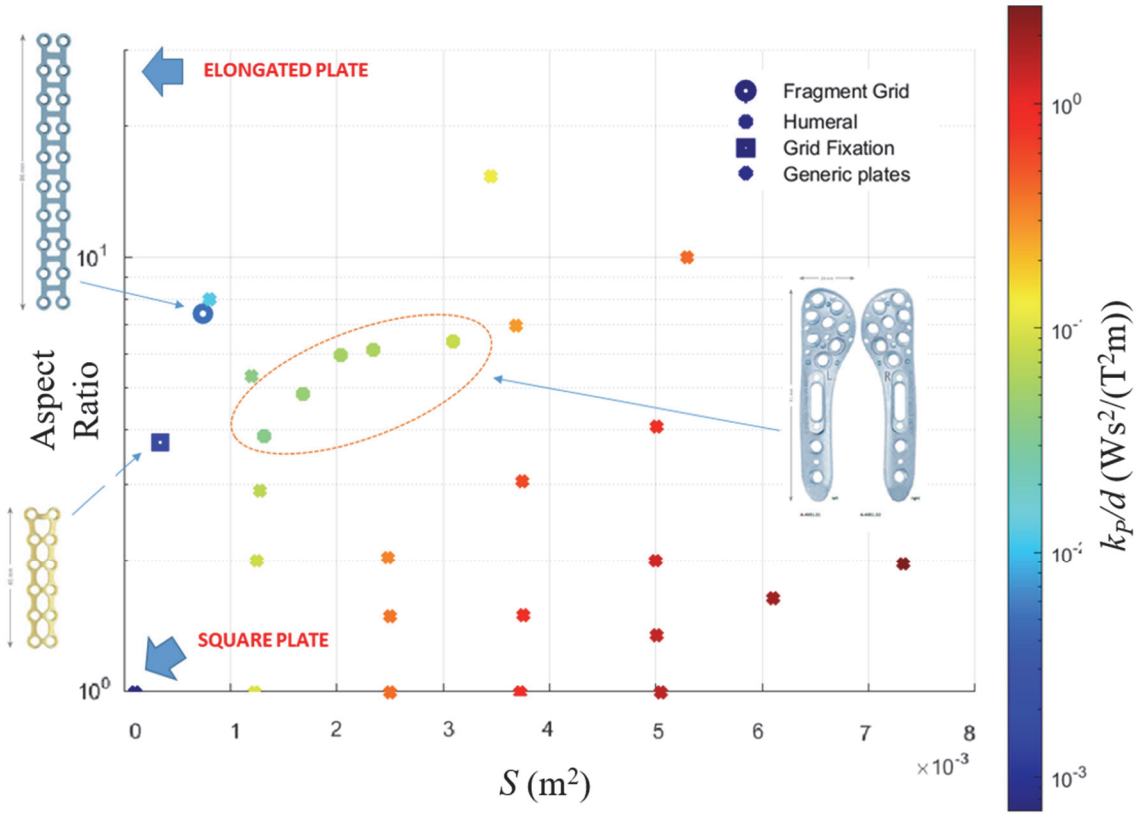

Figure 23: Effect of cross-sectional area and aspect ratio on k_p/d.

Calculations with different implant material properties have shown that the deposited power is linearly proportional to the electrical conductivity of the implant for small implants. For larger implants, the skin depth effect restricts the deposited power to a surface layer and so less power is deposited and the increase with conductivity becomes slower than linear.

The local heating, and hence the maximum temperature rise, is strongly influenced by the rate of transfer of energy from the surface of implant to the surrounding material. The material property that affects the heat transfer most significantly is the thermal conductivity. The smaller the thermal conductivity, the more slowly heat is transferred away from the interface between the implant and the tissue, and so the higher the local heating. Figure 24 shows the temperature rise after 360 s (θ_{360}) plotted against the ratio of deposited power to surface area (P/S) for large implants surrounded by three different materials. The lines on the plot are linear fits to the data for each material. The slope of the red line (gel) and the blue line (muscle) are very similar to one another, with the green line (bone) being separate and having a larger slope (indicating greater heating). The thermal conductivities of gel, muscle, and bone are 0.54 W/(m K), 0.50 W/(m K) and 0.3 W/(m K) respectively, illustrating the relationship.

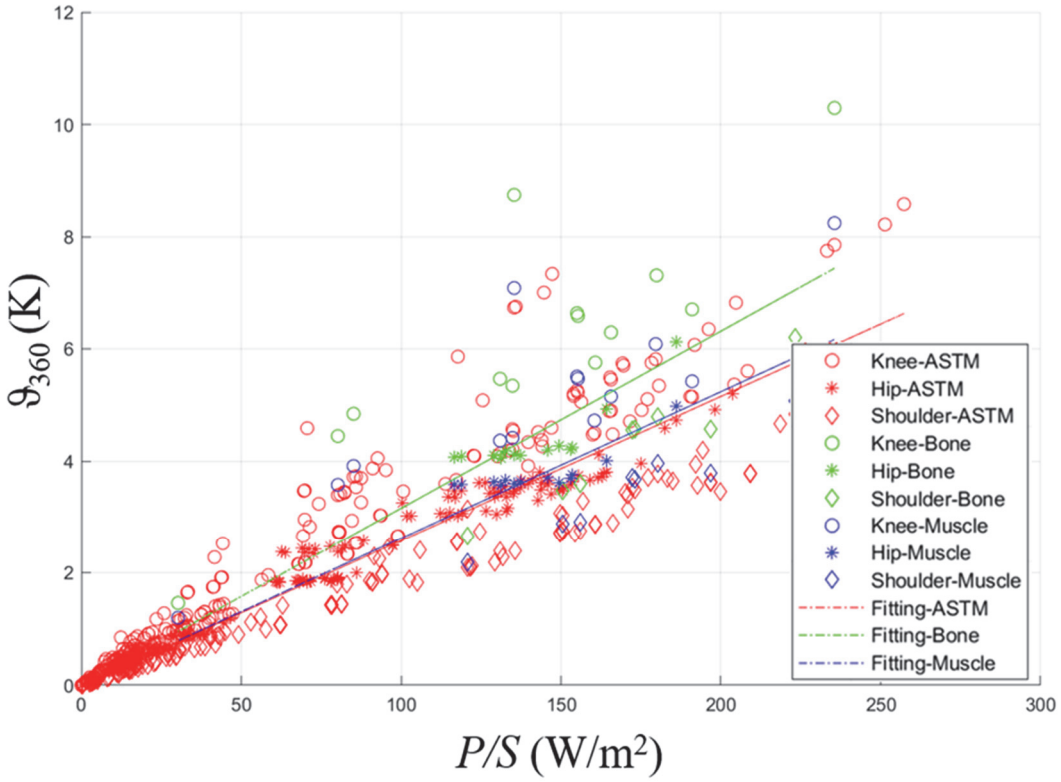

Figure 24: Temperature rise after 360 s plotted against the ratio of deposited power to surface area for large implants surrounded by three different materials.

3.3 PARAMETRIC MODELS FOR GRADIENT FIELD-INDUCED HEATING

The parametric model fitting for the gradient-field model results has used only the results of models of spheroids, because the other geometries had too few model results for a reliable parametric model to be constructed. Two distinct approaches have been used: radial basis functions, and polynomials.

The radial basis function fits used six control variables:

- Spheroid semi-length L,
- Spheroid radius R,
- Spheroid material electrical conductivity σ,
- Angle of field orientation α,
- Scan rise time t_s,
- Scan sequence dwell time t_{dwell}.

Whilst it would be possible to include all six parameters in a single model, the models instead fitted two parameters at a time, holding the values of the other parameter fixed. This approach produces functions that are easier to interpret and to visualise.

The radial basis functions used in this work have been selected to be Gaussian functions, so the models fitted took the form

$$u(\mathbf{x}) = \sum_{i=1}^{N} \gamma_i \Phi(\|\mathbf{x} - \mathbf{x}_i\|), \tag{13}$$

$$\Phi(\|\mathbf{x} - \mathbf{x}_i\|) = \exp(-\beta\|\mathbf{x} - \mathbf{x}_i\|^2), \qquad (14)$$

where u is the quantity of interest (deposited power or temperature rise), $\mathbf{x}$ is a set of values of the control variables, $\mathbf{x}_i$, i = 1, 2, …, N, are the sets of values of the control variables for which model results are available, and γ_i, i = 1, 2, …, N, and β are the parameters to be determined in the fitting. Figures 25 and 26 show some typical results for surfaces fitted to the values of deposited power. Figure 25 shows the dependence on the geometric parameters L and R, and figure 26 shows a fitted surface for the scan sequence parameters t_{dwell} and t_s.

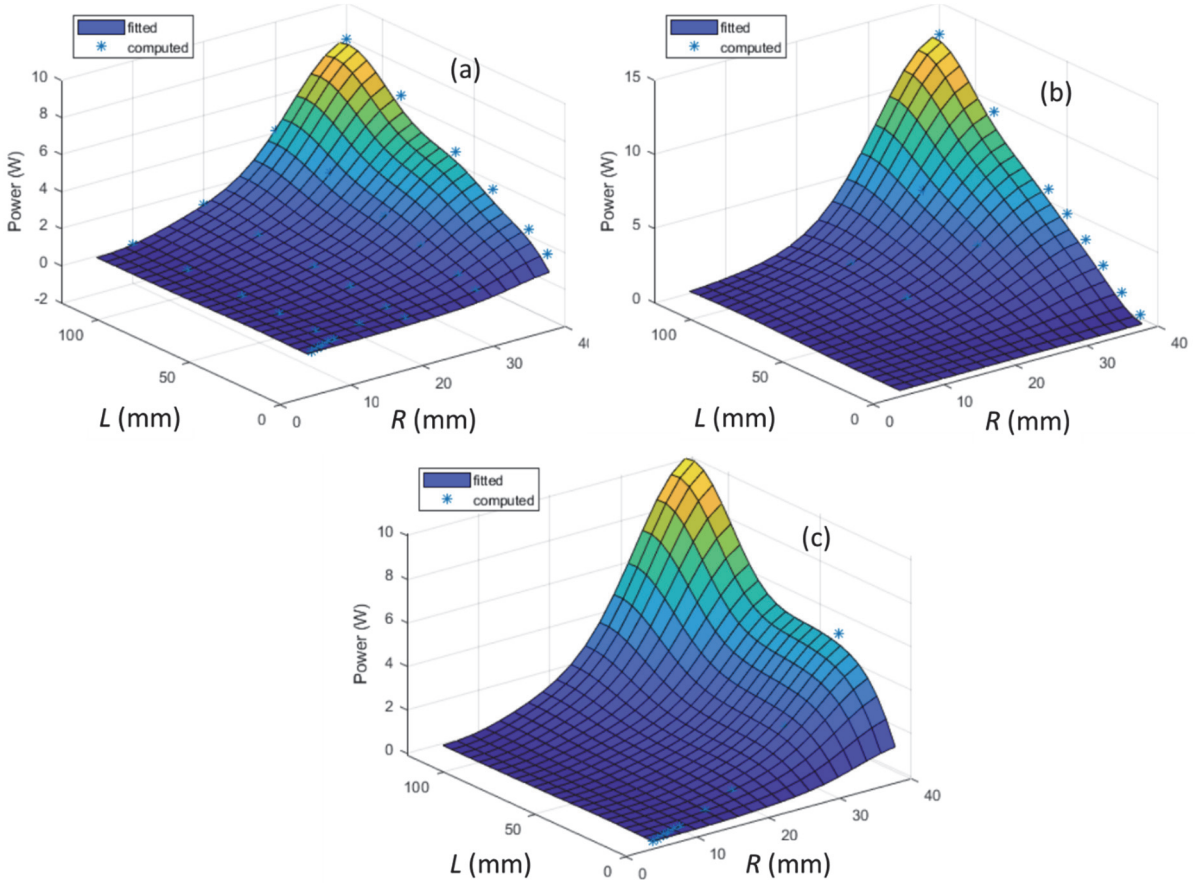

Figure 25: Surfaces showing the deposited power P_T as a function of L and R for a) the SEQ1 sequence for α = 0, b) the SEQ1 sequence for α = π/2, c) the SEQ8 sequence for α = 0.

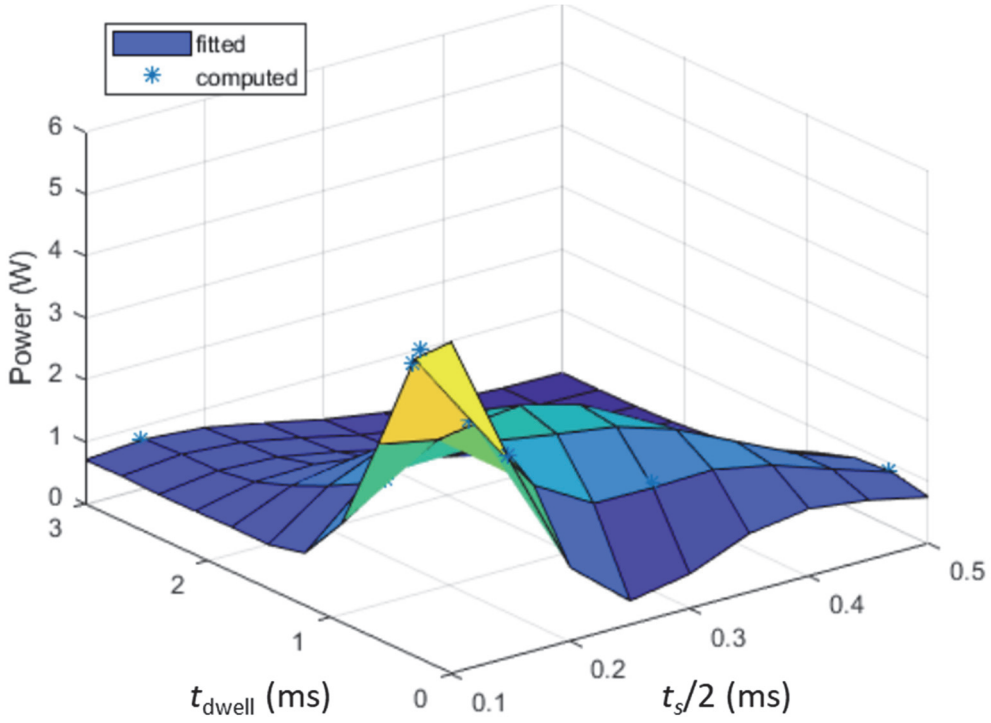

Figure 26: Surface of P_T as a function of t_{dwell} and t_s for α = 0, R = 40 mm and L = 40 mm.

The polynomial fitting used the procedure defined in section 2.3 above. The fitting focussed on the results produced using the scan parameters for SEQ8 as defined in table 8 above. The control parameters were restricted to the geometric parameters L and R and the field angle α, and the temperature rise results were accordingly fitted with 3D polynomials. In the absence of an uncertainty estimate for the GC results, the selection of the best fit was guided by the $\sqrt{2}m$ rule mentioned in section 2.3. The RMSR values obtained for the fits were much larger than those obtained for the RF heating model results, indicating a poor fit. Figure 27 shows the results of the best fit polynomial, and clearly shows that the polynomial is a poor fit to the data. In particular the fit for the largest value of R and small values of L is poor, perhaps indicating a change in the physics causing the temperature rise. The coefficients for these polynomials are not supplied as the fit is too poor for the polynomial to be of use.

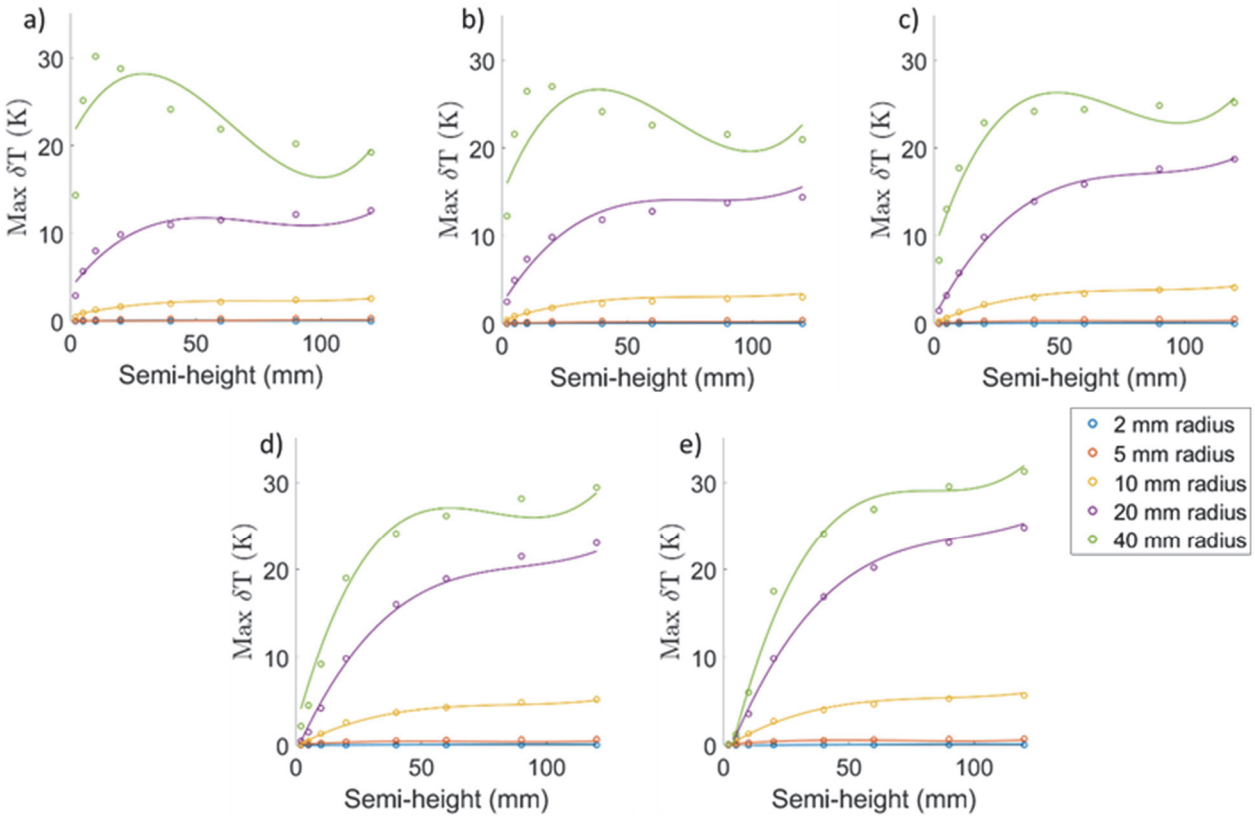

Figure 27: Parametric models for ellipsoid heating after 900 seconds in a 3.0 T field. Each figure shows a slice of a projection of a 3D fit onto a single plane for an angular value of a) 0 °, b) 22.5 °, c) 45 °, d) 67.5 °, e) 90 °. This model has a degree of 1 in angle, 3 in radius and 3 in semi-height, for an RMSR of 1.28 K. The legend is shared for all subfigures.

3.4 COMPARISON OF RESULTS FROM DETAILED AND APPROXIMATE IMPLANT GEOMETRIES

The simulations described in section 2.2 and 3.2 of this report have largely focussed on simple geometries, because these geometries can be parameterised and the parameters can be varied systematically to generate data sets that are amenable to fitting of parametric models. A comparison between more detailed geometric models of implants has also been carried out for both gradient coil and RF modalities.

Two groups of implants were considered. Large orthopaedic implants, including five hip implants, a knee implant and a shoulder implant, were simulated using gradient coil MRI only. These implants were approximated by a set of spheroids that had the same volume and longest dimensions as each of the detailed geometries. As was noted in sections 2.2 and 3.2, RF heating is affected by the longest implant dimension and gradient coil temperature rise is correlated with implant volume which is why these quantities were used to define the spheroidal geometries.

The second group of implants were simulated in both RF and gradient coil modalities. This group consisted of five humeral plates and two fixations. These implants were approximated by cuboidal geometries. The cuboid length and thickness were set equal to the length and thickness of the detailed implant, and the width was set equal to the implant width of the longest section of the implant (the implants generally consist of a long near-cuboidal section and a wider “head” section). The volume of the cuboidal approximations differed from the volume of the detailed geometry by at most 11 % for the humeral plates. A direct comparison

between the detailed implant geometries and the spheroids and cuboids is shown in figure 28, where the blue objects are the detailed implant geometries and the grey objects are the spheroids and cuboids.

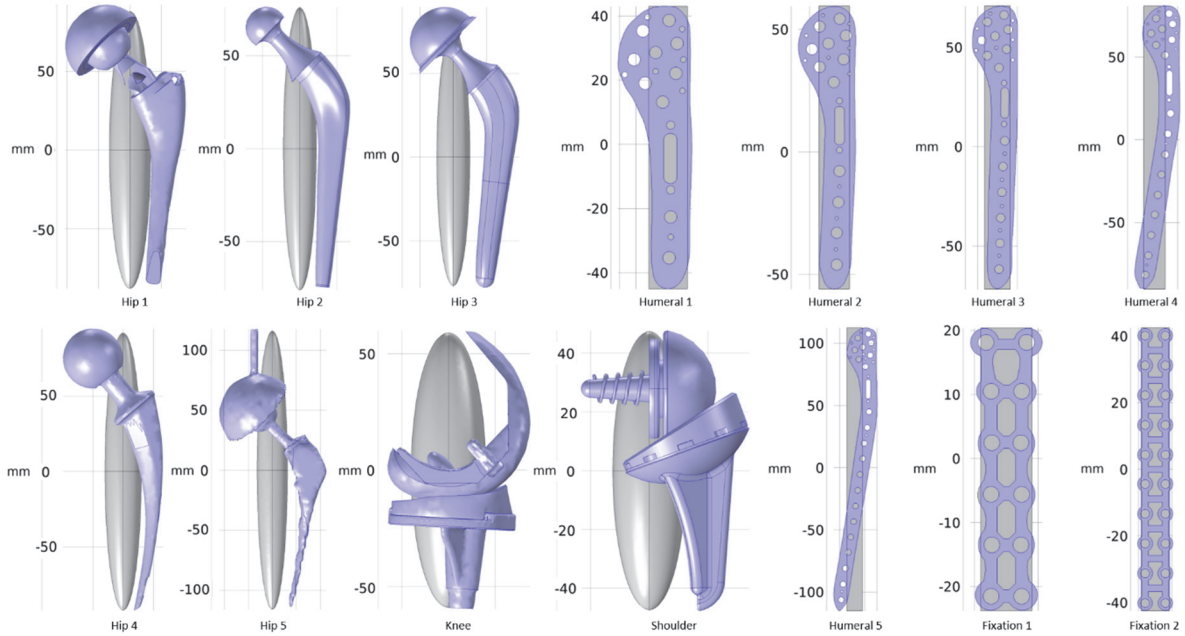

Figure 28: Comparison between the detailed geometries of the realistic implant models and the spheroids of the same volume and longest dimension.

The maximum temperature rises and geometric parameters for each set of models are shown in tables 14, 15, 16 and 17, along with the difference between the temperature rise calculated from the details implant geometry and the temperature rise calculated using the approximate geometry (as a percentage of the value calculated using the detailed geometry). The results show that there is a significant difference between the results of the detailed and approximate models, particularly for the gradient coil models. The results make it clear that an accurate determination of the temperature rise requires consideration of the detailed geometry. Note also that in many cases the gradient coil models with simplified geometry under-predict the temperature rise, in some cases by more than 70 %, meaning that the use of such models may lead to implants being considered to be safe when they are not.

Table 14: Results of approximate and detailed models of large orthopaedic implants in gradient coil MRI scans.

Implant	Detailed geometry temperature rise (K)	Spheroid radius (mm)	Spheroid length (mm)	Spheroid temperature rise (K)	Difference (%)
Hip1	5.57	13.1	88	4.97	-11
Hip2	2.05	8.9	76	1.69	-18
Hip3	1.67	9.9	77	2.27	36
Hip4	8.92	12.1	92	4.08	-54
Hip5	17.5	12.6	116	4.71	-73
Knee	11.8	16	59	7.35	-38
Shoulder	5.52	12.4	47	3.77	-32

Table 15: Results of approximate and detailed models of plate fixtures in gradient coil MRI scans.

Implant	Detailed geometry temperature rise (K)	Cuboid length (mm)	Cuboid width (mm)	Cuboid thickness (mm)	Cuboid temperature rise (K)	Difference (%)
Humeral1	3.76	88	12	3	2.20	-41
Humeral2	3.83	115.5	12.5	3	2.55	-33
Humeral3	3.84	142.5	13	3	2.88	-25
Humeral4	3.63	171	13	3.4	3.29	-9
Humeral5	4.189	227.5	12.5	3.4	3.01	-28
Fixation 1	0.17	44.1	8	1	0.27	59
Fixation 2	0.29	85	8.5	1	0.37	28

Table 16: Results of approximate and detailed models of plate fixtures in RF MRI scans with a field of 1.5 T.

Implant	Detailed geometry temperature rise (K)	Cuboid length (mm)	Cuboid width (mm)	Cuboid thickness (mm)	Cuboid temperature rise (K)	Difference (%)
Humeral1	4.69	88	12	3	4.30	-8
Humeral2	6.18	115.5	12.5	3	5.61	-9
Humeral3	7.15	142.5	13	3	6.49	-9
Humeral4	7.48	171	13	3.4	7.27	-3
Humeral5	7.17	227.5	12.5	3.4	7.35	2
Fixation 1	2.32	44.1	8	1	2.17	-6
Fixation 2	4.86	85	8.5	1	4.84	0

Table 17: Results of approximate and detailed models of plate fixtures in RF MRI scans with a field of 3.0 T.

Implant	Detailed geometry temperature rise (K)	Cuboid length (mm)	Cuboid width (mm)	Cuboid thickness (mm)	Cuboid temperature rise (K)	Difference (%)
Humeral1	3.54	88	12	3	3.44	-3
Humeral2	4.20	115.5	12.5	3	3.46	-18
Humeral3	3.25	142.5	13	3	3.03	-7
Humeral4	2.60	171	13	3.4	2.53	-3
Humeral5	2.54	227.5	12.5	3.4	2.39	2
Fixation 1	1.74	44.1	8	1	1.51	-14
Fixation 2	3.87	85	8.5	1	4.05	-5

4 STATISTICAL ANALYSIS OF THE DISTRIBUTIONS OF COMPUTED RF EXPOSURES OF IMPLANTS FOR THE POPULATION OF PATIENTS AND SCANS

4.1 EXTRACTION AND ANALYSIS OF E-FIELD DISTRIBUTIONS

A series of models of MRI scans of two different human anatomical models (Glenn and Yoon-sun) were developed and run. Every possible combination of

- ten different RF birdcage coils (configurations listed in table 18),
- six different implant locations (hip, knee and shoulder on left and right sides of the body),
- two different frequencies (64 MHz and 128 MHz),

was considered for each anatomical model. Throughout the following, a single combination of implant location, model and excitation frequency will be referred to as a “target”.

The maximum 10 g-averaged electrical field (E10g) within each region of interest around the implant locations was computed and extracted using an evaluation tool developed within work package 2 of MIMAS . Figure 29 shows the regions of interest within each model. The averaging over any 10 g of tissue as described in IEEE C95.31 is implemented by the tool. The value of E10g was calculated at 17 imaging positions for each model, with adjacent positions being separated by 10 cm.

Table 18: Configurations of birdcage coils used in this work. All coils had 16 runs and were operated at both 64 MHz and 128 MHz.

Coil name	Coil diameter (cm)	Coil length (cm)	Shield diameter (cm)
B65_L50	65	50	70
B65_L60	65	60	70
B65_L70	65	70	70
B75_L40	75	40	80
B75_L50	75	50	80
B75_L60	75	60	80
B75_L70	75	70	80
B80_L50	80	50	85
B80_L60	80	60	85
B80_L70	80	70	85

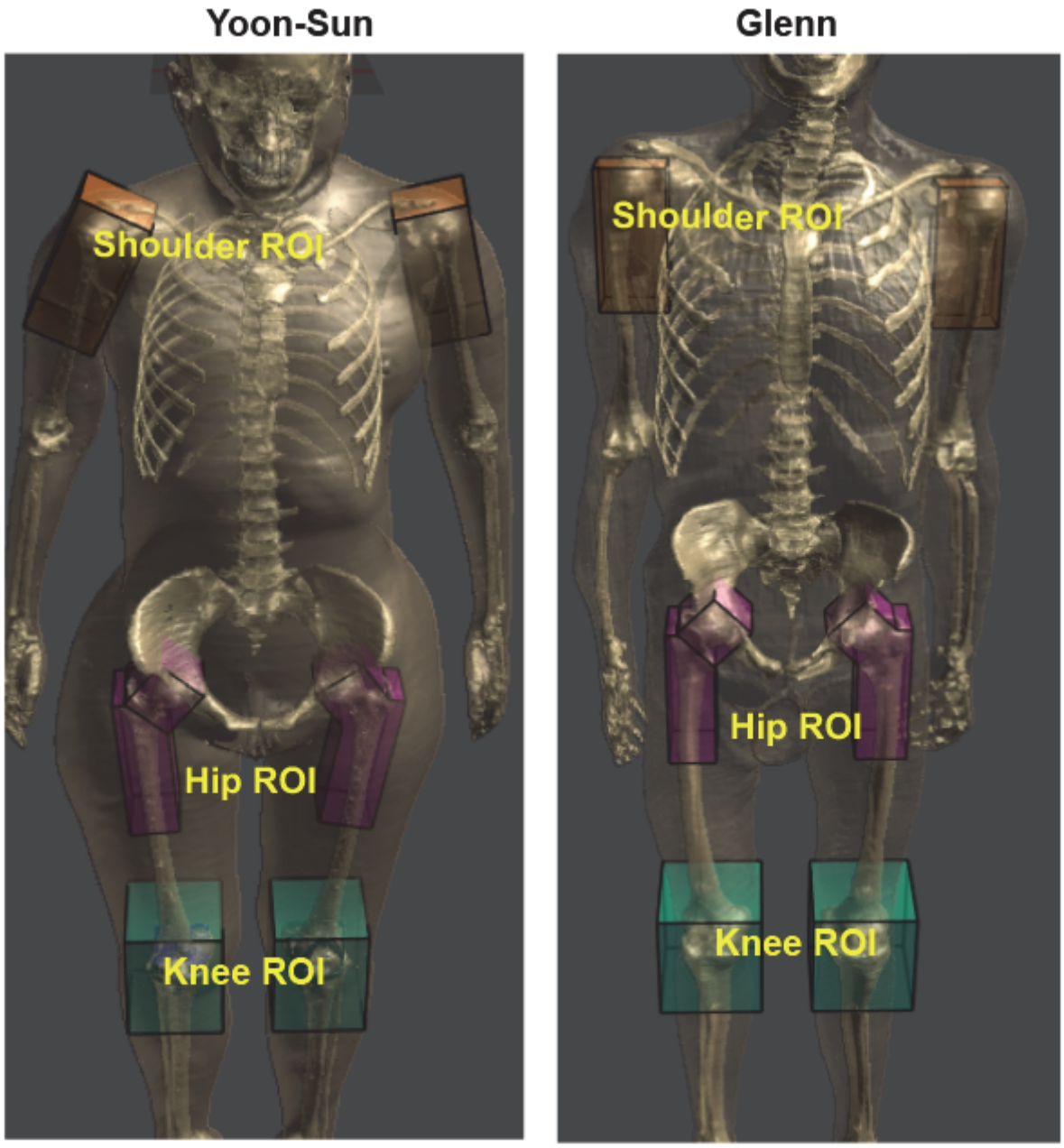

Figure 29: Regions of interest within each anatomical model.

An initial inspection of the data showed that for most (but by no means all) of the targets, the variation of E10g with coil geometry was small. Two examples are shown in figure 30, the plot on the left (Glenn 128 MHz hip left) being typical of the small variations seen in most targets, and the plot on the right (Yoon-Sun 64 MHz knee left) being the plot with the most variation.

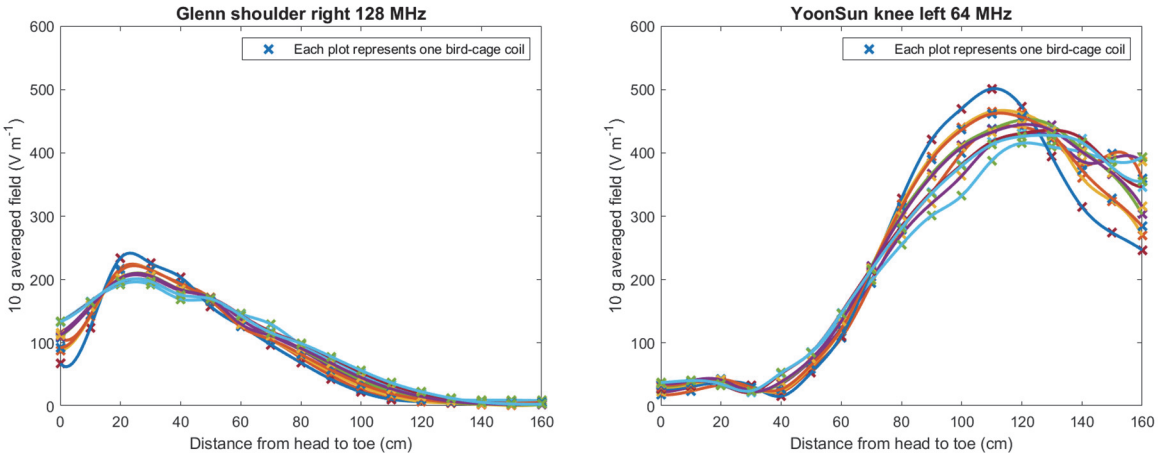

Figure 30: Typical small (left hand plot) and large (right hand plot) variations with coil geometry.

This observation suggested another way of summarizing the data. For each of the 24 targets, the mean of the ten 10 g averaged E-field values was calculated at each image position and plotted against location along with the minimum and maximum values of E10g at each location. To help with visualisation, interpolating cubic splines were calculated and plotted for the minimum, maximum and mean, and the region lying between the minimum and maximum was shaded. The resulting plots are shown in figures 31 to 42, with each figure representing the same anatomical model and implant location and the two plots representing the two different excitation frequencies. The same scale is used throughout on the vertical axes to ease comparison between different plots.

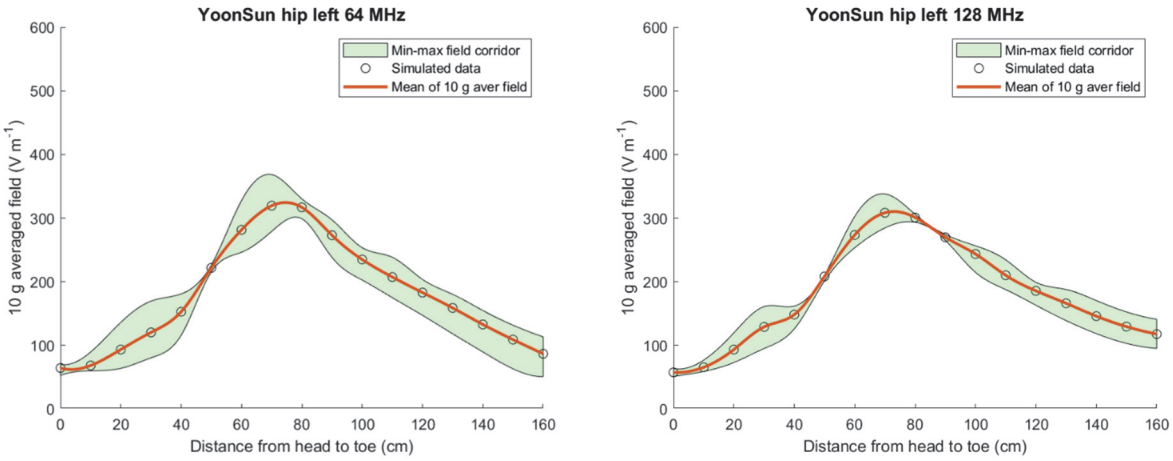

Figure 31: Distribution of 10 g averaged field for Yoon-Sun in the left hip region.

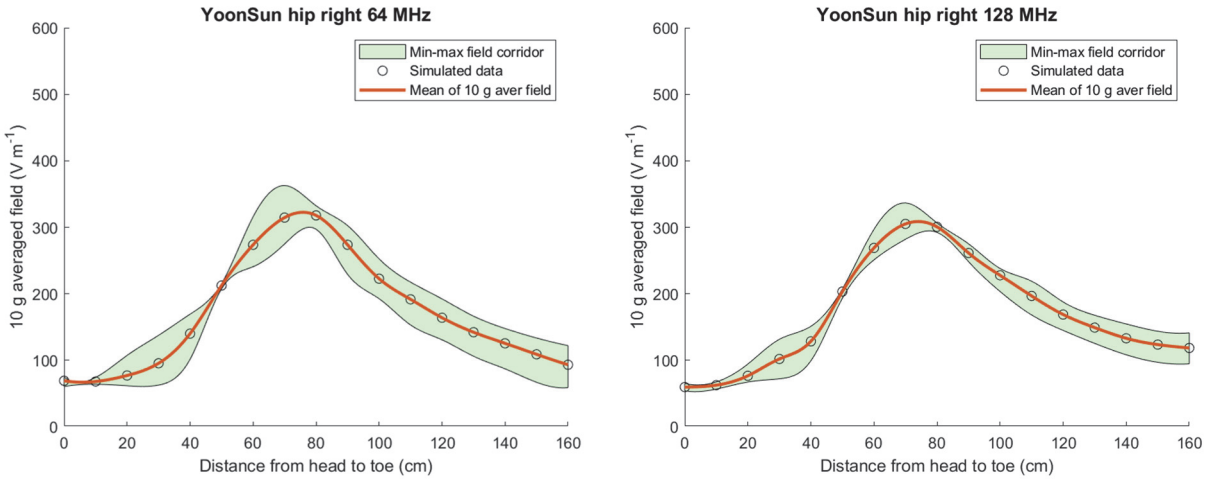

Figure 32: Distribution of 10 g averaged field for Yoon-Sun in the right hip region.

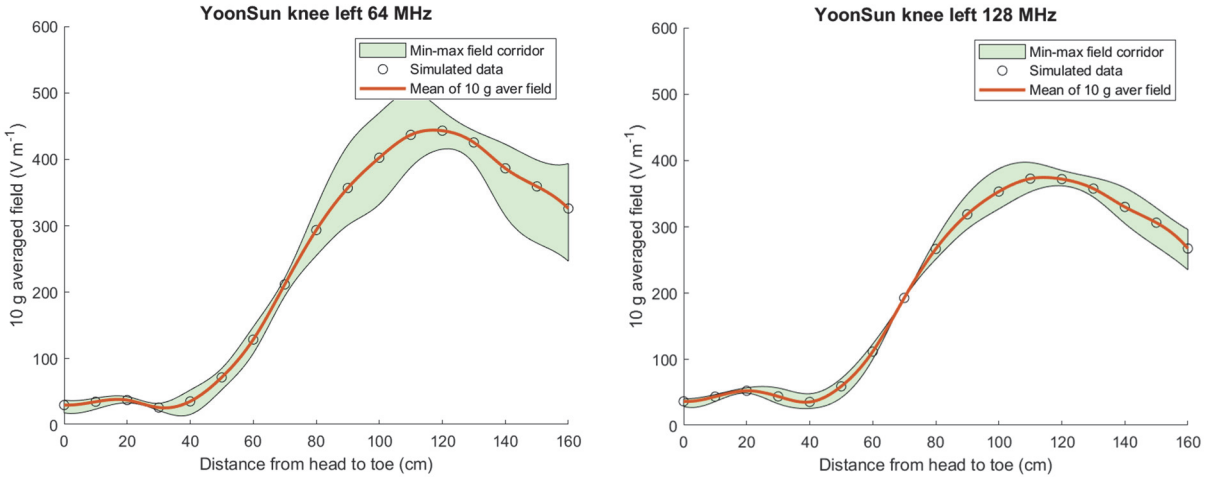

Figure 33: Distribution of 10 g averaged field for Yoon-Sun in the left knee region.

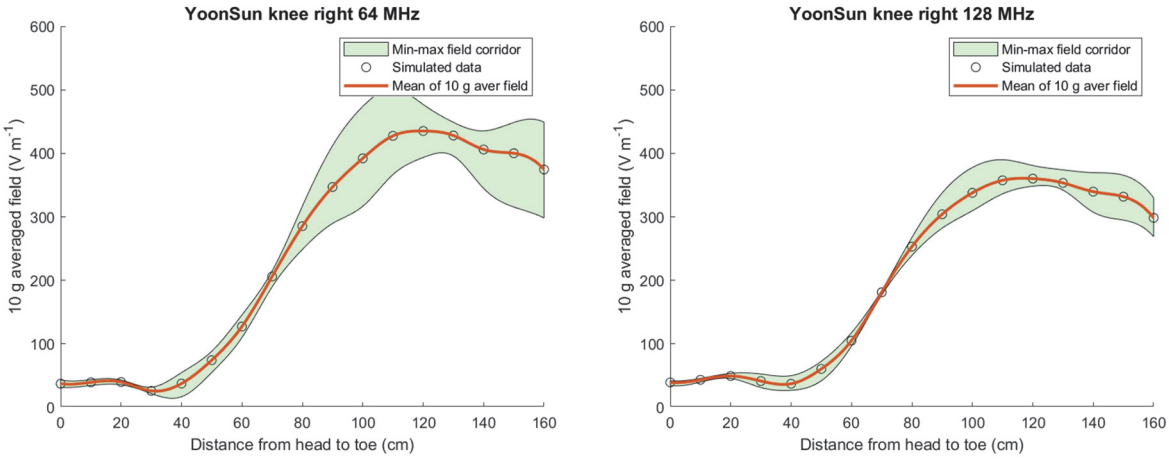

Figure 34: Distribution of 10 g averaged field for Yoon-Sun in the right knee region.

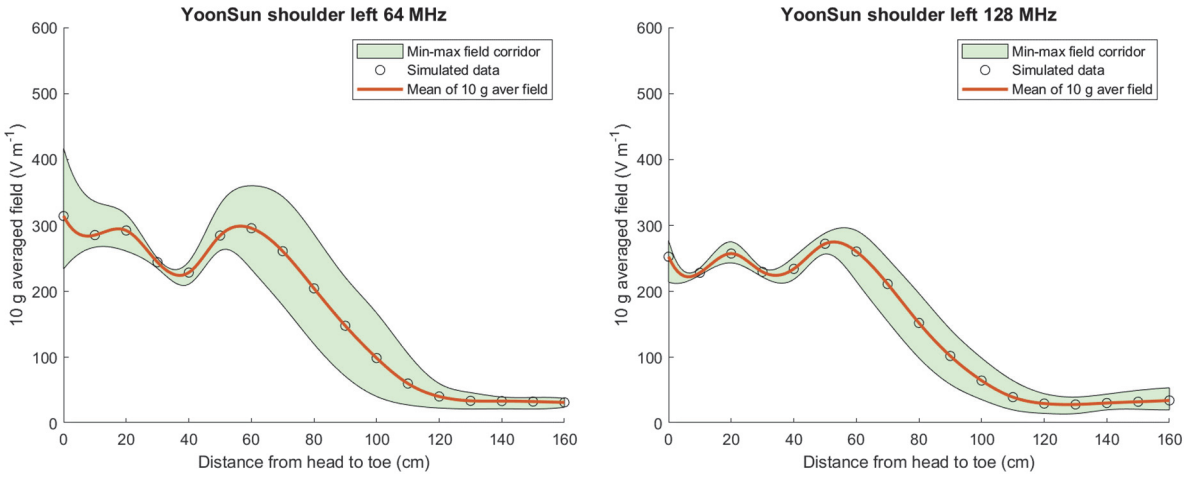

Figure 35: Distribution of 10 g averaged field for Yoon-Sun in the left shoulder region.

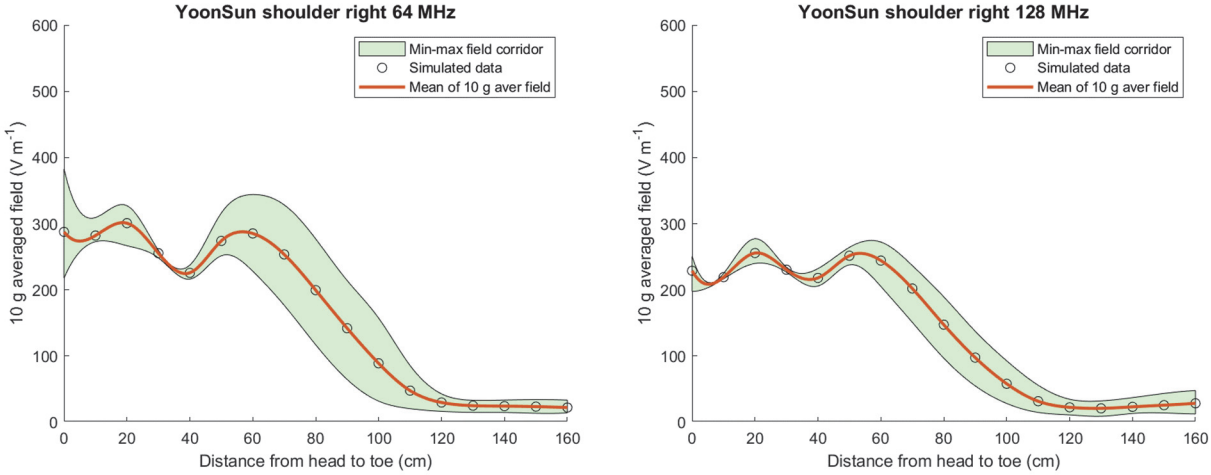

Figure 36: Distribution of 10 g averaged field for Yoon-Sun in the right shoulder region.

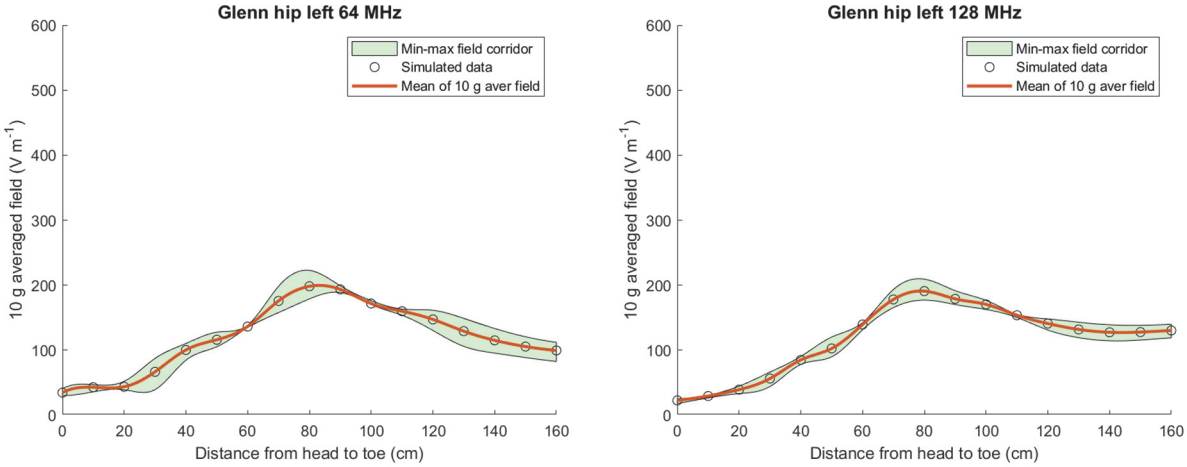

Figure 37: Distribution of 10 g averaged field for Glenn in the left hip region

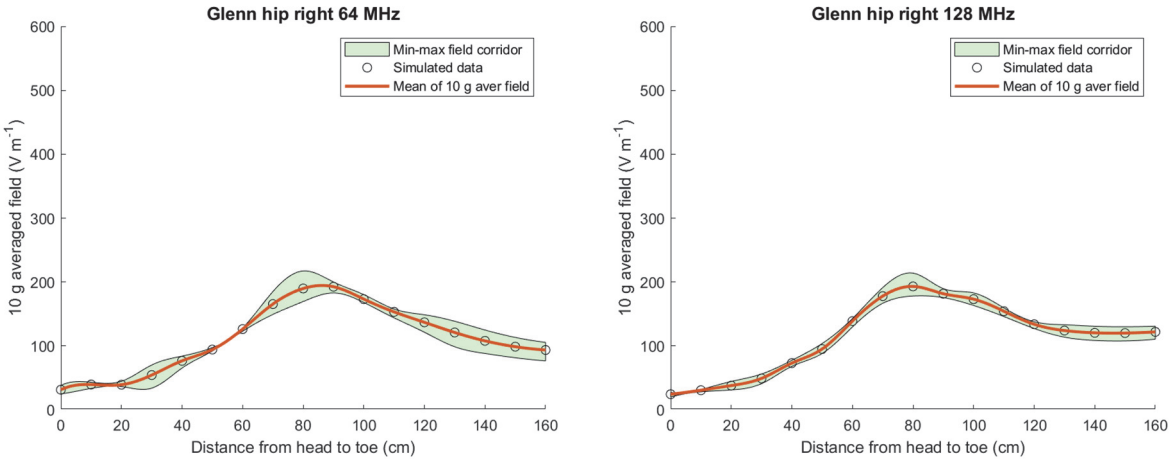

Figure 38: Distribution of 10 g averaged field for Glenn in the right hip region.

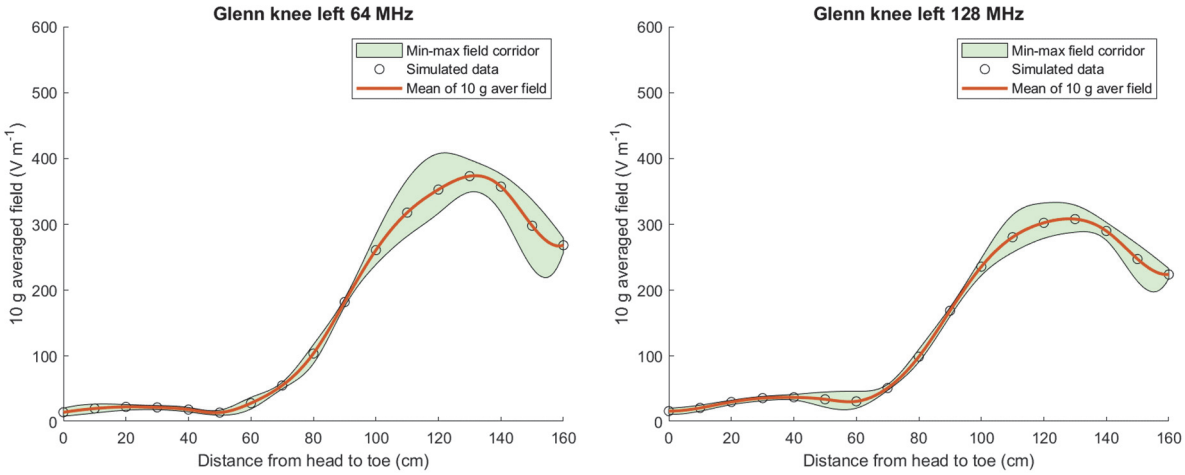

Figure 39: Distribution of 10 g averaged field for Glenn in the left knee region.

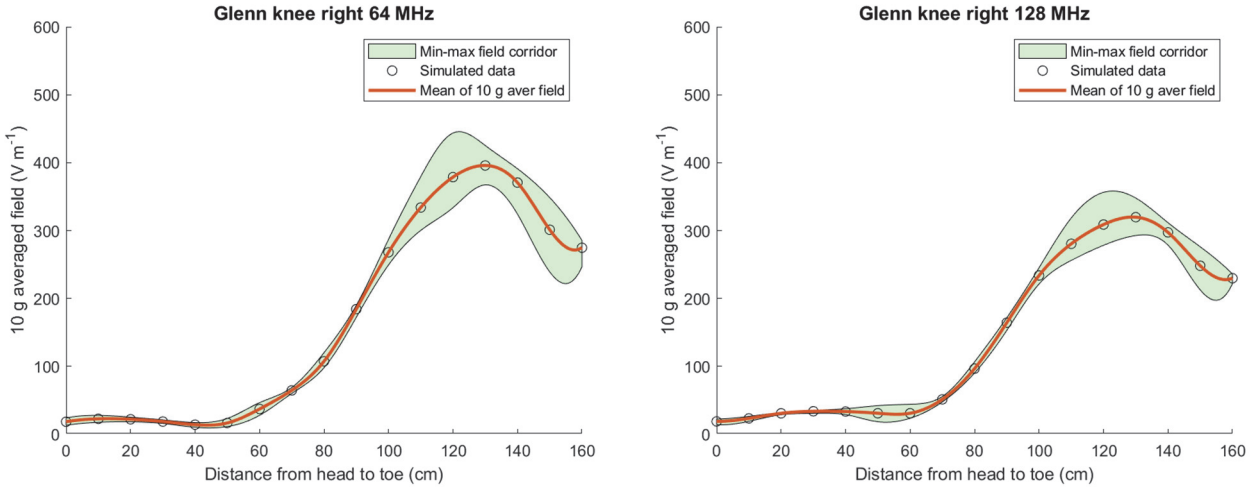

Figure 40: Distribution of 10 g averaged field for Glenn in the right knee region.

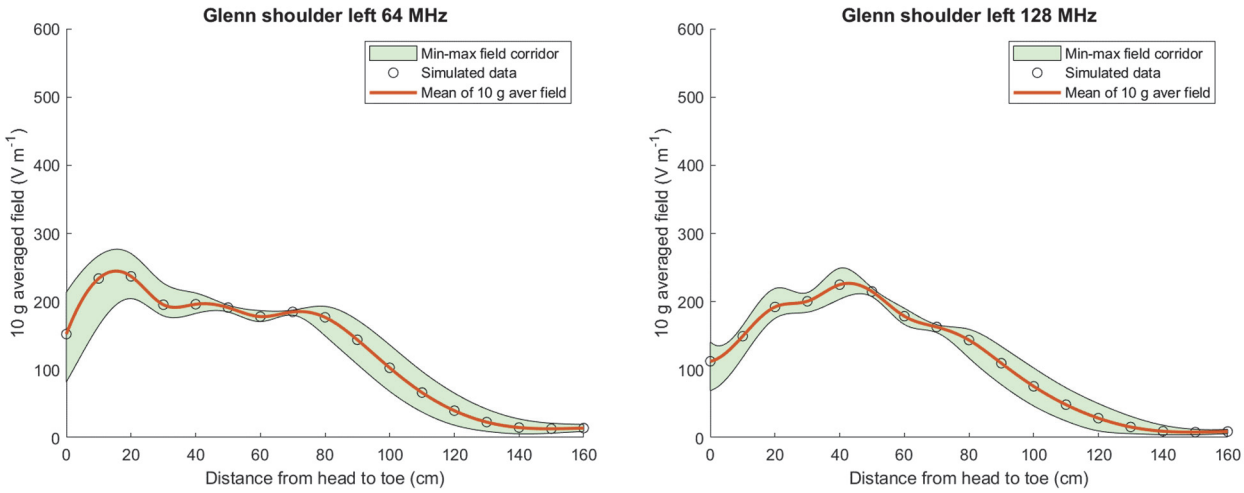

Figure 41: Distribution of 10 g averaged field for Glenn in the left shoulder region.

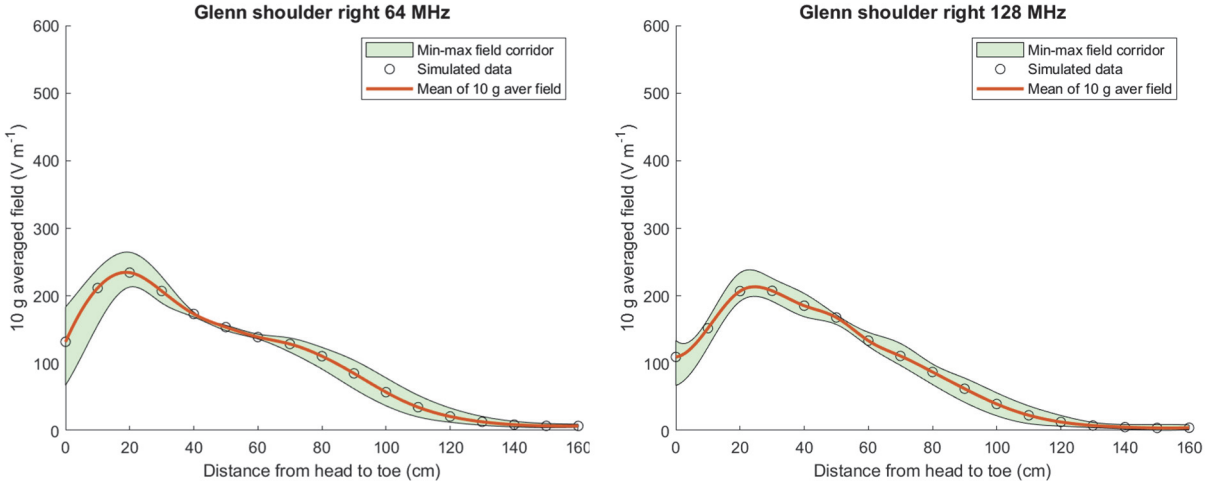

Figure 42: Distribution of 10 g averaged field for Glenn in the right shoulder region.

These figures suggest a number of qualitative observations:

- For most anatomical models and implant locations, the mean behaviour is qualitatively similar for the 64 MHz and 128 MHz excitation frequencies, but the variability is typically higher for the 64 MHz frequency.
- For a given implant location and excitation frequency, the Yoon-Sun anatomical model typically has a larger mean and larger variability than the Glenn anatomical model.
- For a given anatomical model and excitation frequency, the knees have the highest mean values.
- For most anatomical models and excitation frequencies, for a given implant class, the left location shows more variability in E10g values than the right location.

4.2 SCANNER SEQUENCE EFFECTS ANALYSIS

Sequence parameters for seven commonly used MRI sequences were provided by the project partners at INRIM, details are provided in table 19. The parameters of most importance to SAR estimations relate to the RF echo train, which is defined by the pulse repetition time (T_R) which contains the individual pulses of time varying magnetic fields at RF frequencies modulated by an envelope function of width τ , separated by the echo time T_R. T_E is the time at which the echo arrives. The pulse envelope may be simple rectangular

functions, or more commonly sinc shaped pulses with a defined number of side lobes. The duty cycle (*D*) of a pulse train describes the proportion of the total time within T_R in which the RF field is switched on. Finally, the total scan time is defined by the pulse train details and the size of the matrix.

Table 19: Sequence parameters for seven commonly used MRI sequences

Parameter	TRUE FISP	T1 FSE	T2 FRFSE	DWI SE-EPI	T2*GRE	3D FSPGR	PERF GRE-EPI
f (kHz)	64	64	64	64	64	64	64
T_R (ms)	3.9	840	3160	5625	500	14.6	15000
T_E (ms)	1.7	Min(13.2)	68	Min(115.2)	15	6	Min(50.8)
Initial flip angle (°)	70	90	90	90	20	12	90
Matrix	256 × 256	256 × 256	256 × 256	128 × 128	256 × 256	256 × 256	128 × 128
Duration (s)	84	215	200	240	192	336	180
Slices per T_R	1	4	2	12	18	1	12
Echo train and pulse length	1 × 70° τ_{70} = 0.8 ms	4 × 90°, 16 × 180° τ_{90} = 1.6 ms τ_{180} = 3.0 ms	4 × 90°, 34 × 180° τ_{90} = 1.6 ms τ_{180} = 3.0 ms	12 × 90°, 12 × 180° τ_{90} = 1.6 ms τ_{180} = 3.0 ms	18 × 20° τ_{20} = 1.0 ms	1 × 12° τ_{12} = 1.0 ms	12 × 90° τ_{90} = 1.6 ms
Duty cycle (%)	20.5	6.5	3.4	1.0	3.6	6.8	0.1

Attempts were made to implement a typical pulse sequence within Sim4Life so that the detailed human models could be used. The short time steps required to capture the details of the pulse shape accurately meant that the computational complexity was beyond the resources available, so a simpler approach was identified. Estimates of SAR were made using a simple loop model, in which the induced currents due to the time varying electromagnetic field are estimated as taking a circular path through homogenous materials [12-14].

The integral of the electric field around this closed loop is equal to the negative time derivative of the RF magnetic flux density integrated over the surface of the enclosed path. We can therefore write E_{RF} as

$$E_{RF} = \pi f B_{RF} R, \tag{15}$$

where *R* is the path radius, *f* is the RF frequency in Hz and B_{RF} the amplitude of the magnetic field component of the RF signal, which can be estimated from the size of the flip angle θ and the pulse length τ [15]

$$B_{RF} = \frac{\theta}{\gamma \tau}, \tag{16}$$

where γ is the gyromagnetic ratio for hydrogen in water. B_{RF} field amplitudes were calculated for the specified pulses in table 15; where a pulse train contains more than one size of flip angle, an average B_{RF} field value was employed.

Equations (15) and (16) can be substituted back into equation (3) to provide a measure for SAR at a current loop of specified radius. It is possible to derive average SAR values for simplified geometries using volume integration [12] to show that the average SAR within a cylinder (e.g. torso) is equal to half that of the SAR calculated at the perimeter, and the average within a sphere (e.g. a head) is equal to two fifths that of the surface value.

Finally, we note that the equations above assume the RF field is always present, when in fact within an MRI sequence the field is off for the majority of the time. We therefore scale the calculated SAR values with the sequence duty cycle, equal to the sum product of the pulse counts and widths divided by T_R, so that

$$SAR = \frac{\sigma D}{2\rho}\left(\frac{\pi f \theta R}{\gamma \tau}\right)^2 \quad (17)$$

The density and electrical conductivity required for SAR calculation were obtained by taking the average properties within two cylinders intersecting the torsos of the Glenn and Yoon-Sun models. Two cylinders were used per model because the human torso is elliptical so a more representative average is obtained by using two distinct geometries. The results of this calculation are shown in table 20.

Table 20: Averaged properties extracted from the models.

Body Model	Electrical conductivity (S m^{-1})	Mass density (kg m^{-3})	Average torso diameter (m)
Glenn	0.48	1137	0.128
YoonSun	0.29	1081	0.120

Average SAR values were calculated for each scan sequence using both body models. The results are shown in figure 43. In all cases Yoon-Sun has a slightly lower value of SAR, partly because that model has a lower average electrical conductivity (due to a higher fat content) and partly because that model has a lower torso radius. The slightly higher mass density does not compensate for these factors.

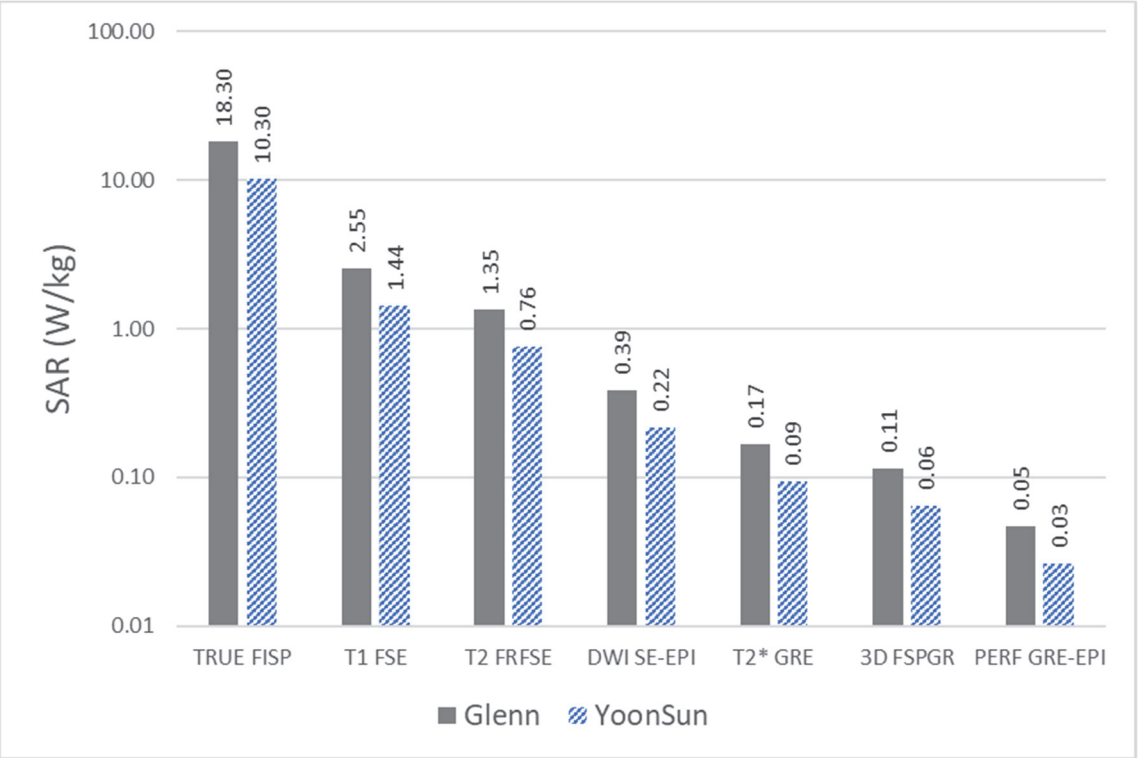

Figure 43: Average estimated SAR values within Glenn and YoonSun assuming a cylindrical loop model around the torso (note that the vertical axis is logarithmic).

In general, the results show the sequences with high numbers of pulses repetitions with high flip angles (requiring a larger perturbation to achieve the desired flip angle) result in the highest SAR values, for example fast spin echo sequences. In general, Gradient Echo sequences produce much lower SAR values because they use gradient reversals rather than refocusing pulses to rephase the MRI signal. The TRUE FISP sequence is an outlier within the group as it is a fast-imaging technique often used for cine-MRI (moving image acquisition) rather than high-resolution static pictures, so it has a very short value of T_R (3.9 ms) and a single 70 ° pulse.

Whilst the induced SAR values obtained during the stated scan durations have been calculated here, it is important to note that in clinical practice, MRI operators estimate SAR prior to each scan, based on the required imaging modality and patient characteristics and will extend scan times, or chose different sequence types in order to stay within regulatory limits. Previous research has shown [16] that the temporal effect of the pulse sequence is visible only on the millisecond timescale and that, provided the delivered doses are scaled to the same SAR, modelling of a simple harmonic excitation is all that is needed in terms of estimating tissue heating.

4.3 FREQUENCY OF REAL-WORLD EXPOSURES

The frequency of real-world exposure of implants to MRI scans was estimated based on data gathered in the UK and freely available online [17-22]. This estimation required data about the number of MRI scans that take place in the UK, data about how many people in the UK have a hip or knee implant, and consideration of the correlation between the presence of an implant and the likely need for a future MRI scan. The last of these three terms is the least known, so a range of possible frequencies has been provided based on different estimates of this term.

The data was gathered from multiple online sources. The UK's National Health Service (NHS) produces an annual report that provides the number of scans carried out using various imaging modalities [17], and the data in the report from 2018 was used to estimate the number of MRI scans carried out on people in various age groups. The Office for National Statistics (ONS) provides census data [18] that gives the age and sex profile of UK residents in 2011. The ONS also supplies the number of deaths and mortality rates in the UK for the years between 1963 and 2019 [19].

The UK's National Joint Registry (NJR) publishes an annual report [20] which provides details of the age profile of patients receiving implants in a given year, total numbers of patients receiving different implant types for each year from 2004, and also provides individual guides [21] which provide information about average age, common diagnoses, and BMI, all of which have informed the analysis.

The data from the NJR 2019 report was supplemented by data from two graphs in an online book chapter [22]. Figure 1 in that chapter shows the number of knee and hip replacements for each year from 1991 to 2006, with a separate plot for each sex. The data plotted have been gathered from GP records (via the Clinical Practice Research Datalink) by searching for particular codes that relate to knee and hip replacements within that database, so are unlikely to be identical to the NJR reports because not all practices contribute to the database (and in particular private clinics are not included) so the data may not be consistent.

This information was used to estimate how many people within various age groups in the UK population have a hip implant or a knee implant. The number of implants in each age group was estimated by calculating a cumulative total, taking mortality rates and implant revision rates into account, over a period of 50 years. The approach developed used historical data and tracked successive cohorts of people between the ages of 50 and 90 to obtain an estimate of how many people in the UK currently have an implant. Separate estimates were calculated for men and women.

The difficulty of estimating the likely correlation between having an implant and requiring an MRI scan (which is likely to be significant since conditions such as obesity increase the probability of an individual requiring both interventions) was avoided by stating the average risk and the maximum risk. The average risk assumed that there was no correlation between the two factors, and was calculated by multiplying the probability of an individual within a demographic group having a hip implant or a knee implant by the probability of an individual in that demographic group requiring an MRI scan. The maximum risk assumed that the two factors were perfectly correlated and was calculated as the smaller probability of the two risks. The calculated values are shown in tables 21 and 22.

Table 21: Estimated average and maximum risk of exposure to MRI scans for men and women with hip implants expressed as a percentage.

Age group	Male average risk	Male maximum risk	Female average risk	Female maximum risk
<55	0.03	1	0.04	1
55 – 59	0.15	2	0.18	2
60 – 64	0.25	3	0.31	3
65 – 69	0.42	4	0.57	5
70 – 74	0.64	6	0.86	8
75 – 79	0.92	8	1.1	11
80 – 84	1.3	11	1.3	13
85 - 90	2.1	15	1.3	15

Table 22: Estimated average and maximum risk of exposure to MRI scans for men and women with knee implants expressed as a percentage.

Age group	Male average risk	Male maximum risk	Female average risk	Female maximum risk
<55	0.02	0	0.03	1
55 – 59	0.11	1	0.16	2
60 – 64	0.24	2	0.33	3
65 – 69	0.49	5	0.62	6
70 – 74	0.8	8	0.95	9
75 – 79	1.2	11	1.2	12
80 – 84	1.6	14	1.3	14
85 – 90	2.5	18	1.3	15

5 ANALYSIS OF THE EFFECTS OF TISSUE COMPOSITION IN THE REGION OF IMPLANTS

5.1 EXTRACTION AND ANALYSIS OF DISTRIBUTION OF TISSUE TYPES

Digital models of Glenn and Yoon-Sun were discretized with very fine resolution (cubic voxels with a side length of 0.5 mm) to identify the tissue distributions near the implant sites shown in figure 27. As the tissue distributions are symmetric, only the left side sites were extracted. The extracted data gave location-specific tissue types (for instance "Fibula_cancellous_right") so the data from each site were grouped into twelve tissue type groups so that the distribution at different sites would be easier to compare. The percentage of each tissue type in each location are listed in table 23. SAT denotes subcutaneous adipose tissue. These results are presented visually as tree-maps in figures 44 to 49.

In general, it is clear that Yoon-Sun has higher fat percentages at all three sites. Fat has a lower thermal conductivity than muscle and hence energy deposited in fatty areas is less likely to be conducted away and so hot-spots are more likely to form. Fat also has a lower density than muscle, and so for a given deposited energy E, since $E = \rho\, c_p\, T$, higher temperature rises are likely to occur in Yoon-Sun.

Table 23: Percentage by volume of each tissue type around each implant location. Lines containing 0.00 indicate that the tissue type is present but the percentage is less than 0.005 %.

	Glenn Knee	Glenn Shoulder	Glenn Hip	Yoon-Sun Knee	Yoon-Sun Shoulder	Yoon-Sun Hip
Artery / Vein	2.5	2.0	1.3	0.3	0.4	0.5
Bone marrow	0.1	2.0	2.2	2.3	2.9	3.8
Cancellous bone	25.0	16.3	17.1	9.9	5.2	9.3
Cartilage	0.4	-	-	0.1	-	-
Cortical bone	7.2	5.7	6.6	7.6	8.0	10.0
Fat / SAT	17.8	9.4	8.2	64.9	43.4	30.0
Ligament	9.9	-	-	0.3	-	-
Lymph node	0.01	0.13	-	0.00	-	-
Muscle	27.0	62.9	64.6	9.0	32.9	45.9
Nerve	0.2	-	0.04	0.2	0.4	0.63
Skin	9.9	1.5	0.01	5.5	6.7	-
Urine	-	-	0.00	-	-	-

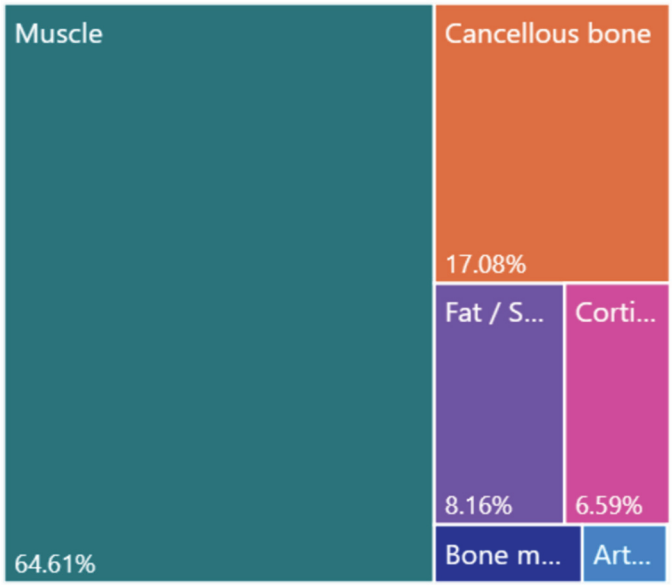

Figure 44: Tissue distribution around the Glenn hip site.

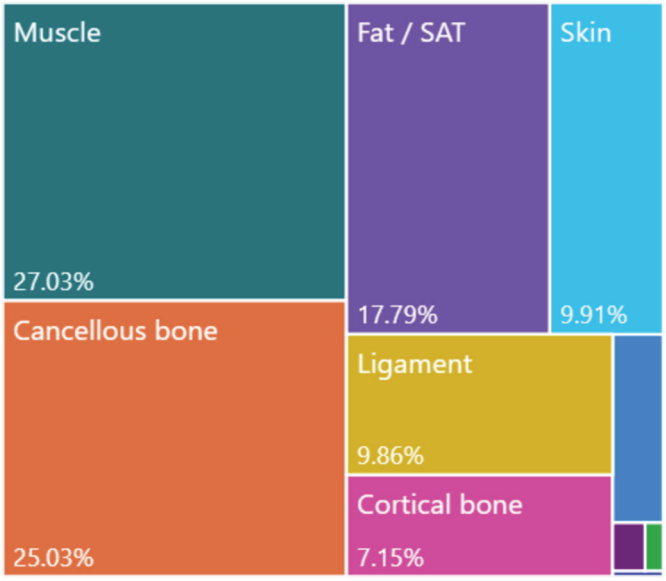

Figure 45: Tissue distribution around the Glenn knee site.

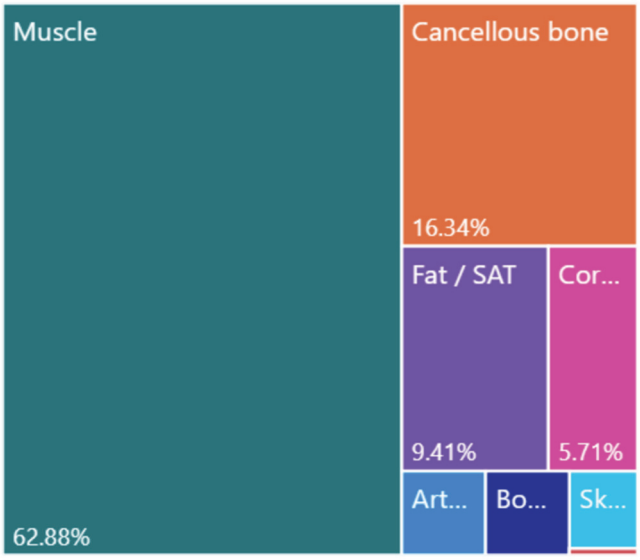

Figure 46: Tissue distribution around the Glenn shoulder site.

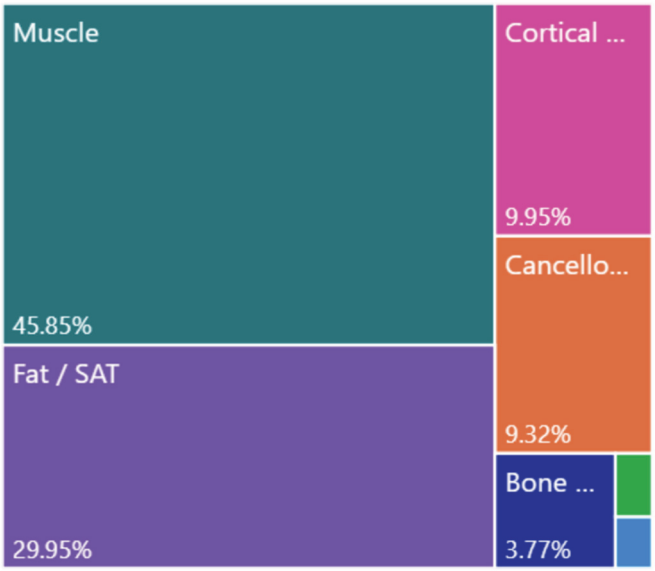

Figure 47: Tissue distribution around the Yoon-Sun hip site.

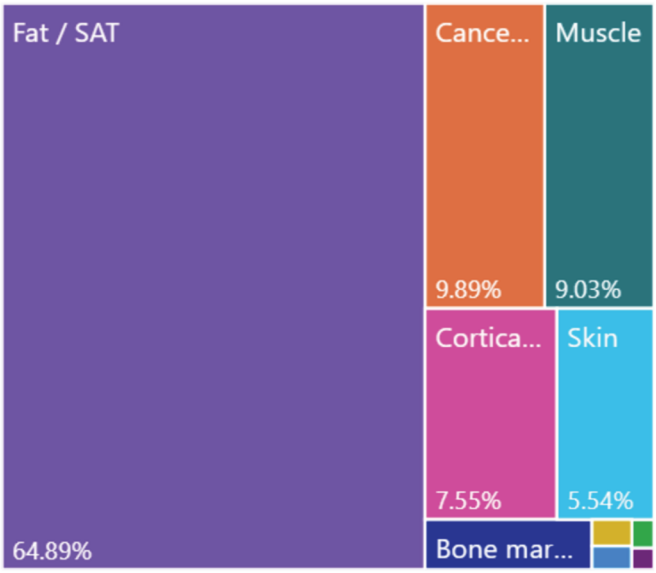

Figure 48: Tissue distribution around the Yoon-Sun knee site.

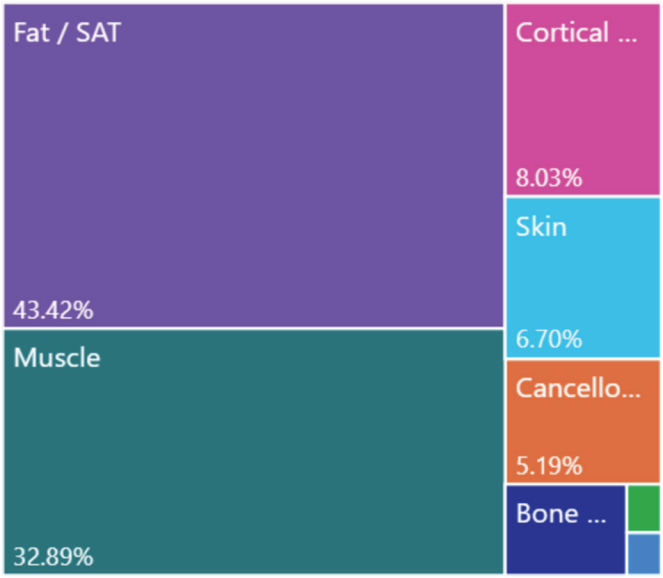

Figure 49: Tissue distribution around the Yoon-Sun shoulder site.

The in vivo field distributions (as reported in section 4.1) are not likely to be strongly correlated with the tissue properties inside the box. The distributions are affected by the properties along the whole body, not just in the implant area, so no attempts have been made to link the information above with the information in section 4.1.

The effects of varying the thermal properties of the tissue around the implant have been considered directly for GC simulations, as is described in full in deliverable 6 of the MIMAS project [46]. A set of full-body models using Yoon-Sun and Glenn were constructed, inserting realistic orthopaedic implants into the shoulder, hip and knee and placing the subjects into the MRI coils such that the most severe heating conditions would be generated. These models were solved using the material properties within Sim4Life to generate six base cases.

The values of perfusion coefficient, thermal conductivity and volumetric heat capacity were each assigned a variability range (respectively 30 %, 15 % and 20 %) after analysis of the material property data available. Four additional material property combinations were defined as follows:

- AP: perfusion coefficient decreased by 30 %, thermal conductivity decreased by 15 %, volumetric heat capacity decreased by 20 %;
- BP: perfusion coefficient decreased by 30 %, thermal conductivity decreased by 15 %, volumetric heat capacity increased by 20 %;
- AM: perfusion coefficient increased by 30 %, thermal conductivity increased by 15 %, volumetric heat capacity increased by 20 %;
- BM: perfusion coefficient increased by 30 %, thermal conductivity increased by 15 %, volumetric heat capacity decreased by 20 %;

and the six different models of a full body with an implant were evaluated using tissue properties that were all changed by the given amount. The maximum temperature rise after 900 s was evaluated for each model and compared to the relevant base case.

For models where the implant had fully replaced tissue (a “virtual surgery”), the use of the material properties defined by AM led to a decrease in maximum temperature rise of between 8 % and 11 % for Yoon-Sun (dependent on implant location) and a decrease of between 7 % and 10 % for Glenn. These values always led to the largest decrease in temperature rise. The largest increase in temperature rise occurred for the properties defined by AP, which led to an increase of between 10 % and 15 % for Yoon-Sun and an increase of between 9 % and 14 % for Glenn.

These results are consistent with what might be expected. A lower perfusion and a lower thermal conductivity mean that energy is not removed from the tissue around the implant, so hot spots become more likely. A decrease in volumetric heat capacity means that a given amount of energy in a volume of tissue will increase the temperature more in that tissue.

5.2 EFFECTS OF PERFUSION AND ASSOCIATED CORRECTION FACTORS

Perfusion is the flow of blood through microscopic capillaries in tissue, and produces a cooling effect that is lacking in the ASTM standard gel. A series of models was run that deposited energy within an implant in two distinct ways so that the effects of perfusion on temperature distribution could be investigated. The two energy deposition approaches were to distribute the energy uniformly within the implant (as might be seen in a gradient coil scan) and to focus the energy at the ends of the implant (as would be seen during an RF scan). Each model was run in three ways: without perfusion, to provide a baseline; with constant perfusion; and with temperature-dependent perfusion.

The model used was a thermal model only (with no electromagnetic calculations). The energy deposited in the model was chosen by analysing the power deposited by a 1.5 T RF field in a cylinder 100 mm long. The maximum power deposited was varied between 0.1 W and 1 W in steps of 0.09 W. The power was applied uniformly in time for 900 s. The outer surfaces of the geometry were regarded as perfectly insulated, a worst-case scenario. The initial temperature was set at 310.15 K (normal human body temperature).

The model geometry, shown in figure 50 was a highly simplified approximation to a plate placed on a bone, surrounded by tissue. The plate measured 100 mm in length, and was a 30 ° section of a hollow cylinder of inner radius 36 mm and outer radius 41 mm (meaning that the plate thickness is 5 mm and the plate width is approximately 2 cm). As can be seen in figure 48, the plate is subdivided along its length into sections that are 5 mm, 90 mm, and 5 mm long so that the power can easily be deposited in the ends of the plate within the model by defining an appropriate source term within the different sub-volumes. The bone is represented by a cylinder 36 mm in radius and 250 mm long. The surrounding tissue is a cylinder 80 mm in radius and 250 mm long.

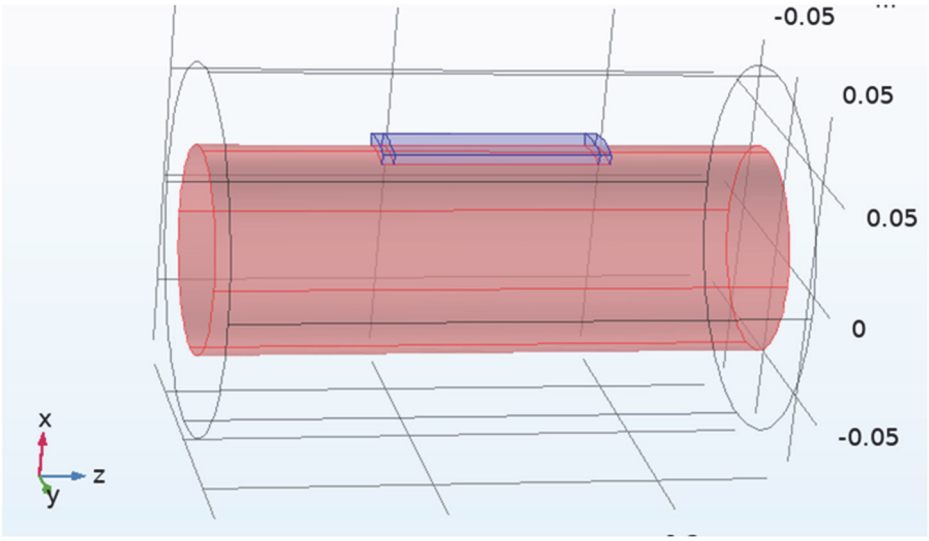

Figure 50: Model geometry, showing the plate in blue and the bone in red.

The material property data extracted from the human model Yoon-Sun in the knee region was used to define two sets of material properties (“bone”, a volume-weighted average of the cortical and cancellous bone properties, and “not bone”, a volume-weighted average of the other tissues in the Yoon-Sun knee region). The material properties used, including the properties of the plate, are listed in table 24.

Table 24: Thermal properties used in the model.

Material	Thermal conductivity (W/ (m K))	Specific heat capacity (J/(kg K))	Density (kg/m^3)
Plate	7.2	520	4430
Bone	0.31	2060	1340
Not bone	0.41	3145	1052

Only the “not bone” region was treated as having perfusion active. The version of the perfusion equation within COMSOL Multiphysics,

$$c_p \rho \frac{\partial T}{\partial t} = \nabla.(\lambda \nabla T) - \rho_b c_b \hat{\omega}(T - T_b) + Q, \quad (18)$$

requires a perfusion constant with units s^{-1}. Two different approaches were used to model the perfusion. A constant term ω_0 was set for one group of models, set equal to 0.0012 s^{-1} (again, calculated from the data supplied by ZMT). For the other group of models, the temperature dependence of perfusion on temperature (blood flow rate increases with raised temperature) was modelled as a function of the form

$$\begin{matrix} \omega_0 \left(1 + [K-1] \exp\left\{ -\left(\frac{[T - 318.15]^2}{12} \right) \right\} \right), & T \leq 318.15 \text{ K}, \\ \omega_0 K, & T > 318.15 \text{ K}, \end{matrix} \tag{19}$$

where the scaling factor *K* was set to 3.4. This form was taken from [23], with the scaling factor chosen as a balance between the fat and muscle values in that reference and the balance being in proportion to that found in the Yoon-Sun knee material properties.

An initial comparison was carried out to check the dependence of the temperature rise upon the power deposited. For the cases with constant perfusion and no perfusion, the temperature rise will always be linearly dependent on power deposited. Figure 51 shows the maximum temperature rise against time plots for temperature-dependent perfusion with energy deposited at the ends of the plate. The curves for different deposited powers are identical in shape and are evenly spaced up the vertical axis, illustrating that the dependence on power is likely to be linear.

The dependence on power of the temperature-dependent perfusion cases was considered in more detail by taking the maximum value of temperature rise at each time step for each deposited power, dividing by the maximum value of temperature rise at each time step for the maximum deposited power, and calculating the standard deviation and the mean. The mean values were equal to the ratio of the deposited power to the maximum power, and the standard deviations were between 0.2 % and 2.7 % of the mean values, suggesting that linear dependence of the temperature rise on the power is a good approximation. These results show that considering only the maximum power deposited when calculating correction factors is valid.

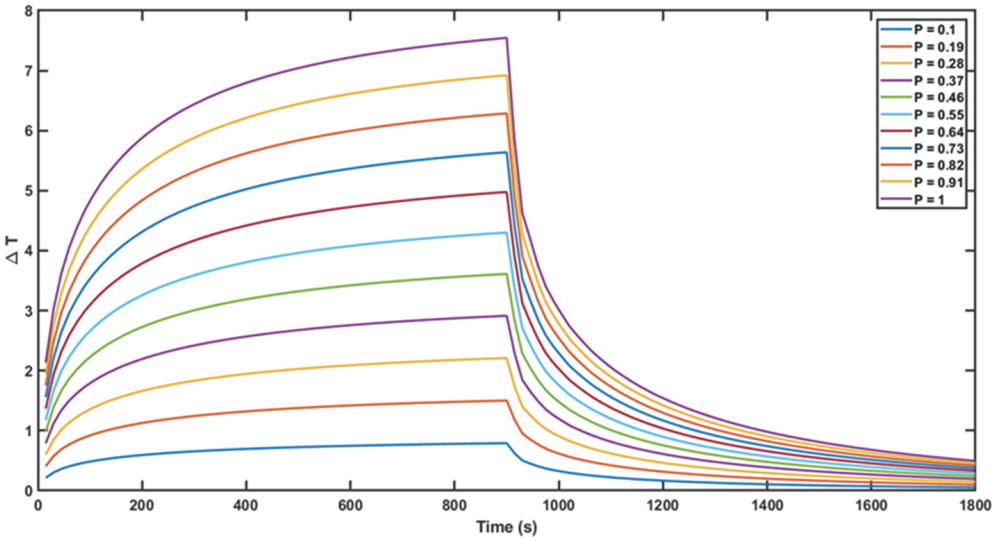

Figure 51: Maximum temperature rise plotted against time for temperature-dependent perfusion with energy deposited at the ends of the plate.

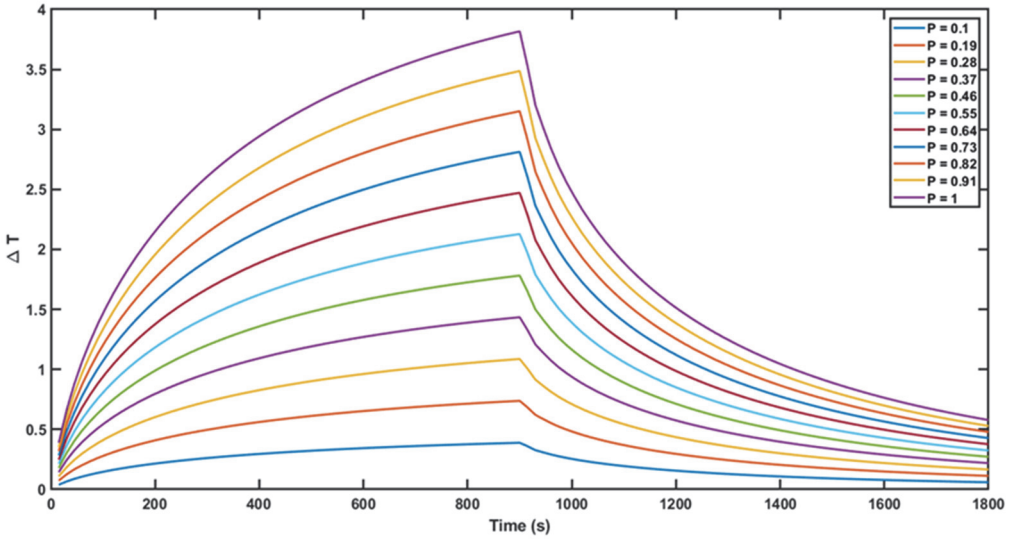

Figure 52: Maximum temperature rise plotted against time for temperature-dependent perfusion with energy deposited uniformly within the plate.

Figure 52 shows the maximum temperature rise against time plots for temperature-dependent perfusion with energy deposited uniformly within the plate. Comparing figures 51 and 52, it is clear that the focussed energy deposition leads to a temperature rise approximately double that of the uniform power deposition, and the cooling rate of the uniform power is lower, because the temperature gradients are lower compared to the temperature gradients surrounding the hot-spots in the focussed power deposition case.

Figure 53 shows a direct comparison between the temperature rise generated by the maximum deposited power for all six configurations. The figure shows that perfusion leads to a decrease in the maximum temperature, and that temperature-dependent perfusion has a slightly greater cooling effect than constant perfusion for the values used in this model. The cases with no perfusion also have a higher temperature after 15 minutes of the power being off, because these models have no means of cooling.

As was mentioned above, the lack of perfusion in saline gel means that the temperatures obtained during the ASTM test [1] are higher than would be seen in a human. The results from the models above can be used to estimate correction factors. Validation of these factors would require either measurement of temperature rise in real human subjects, which is not possible in a non-invasive manner, or creation and measurement of a phantom that included perfusion. The factors as stated here should therefore be regarded as estimates and should not be used in a clinical setting without further validation.

Figure 54 shows the ratio of the perfused to non-perfused temperatures for constant and temperature-dependent perfusion for both types of power deposition, plotted against time. The ratio is dependent on the local temperature distributions, so plotting as (for instance) a function of temperature is not useful. The most important value from this plot is probably the correction factor at the maximum temperature. The values at this point (at 900 s) are shown in table 25. The values obtained suggest that perfusion, for the values used in this model, decreases the maximum temperature in the tissue by 10%.

For interest, figure 55 shows the ratio of the maximum temperature rise for the temperature-dependent perfusion to the maximum temperature rise for the constant perfusion. The plot suggests that the temperature-dependence of the perfusion has a more significant effect on temperature for the focussed power deposition, which generates higher temperature rises.

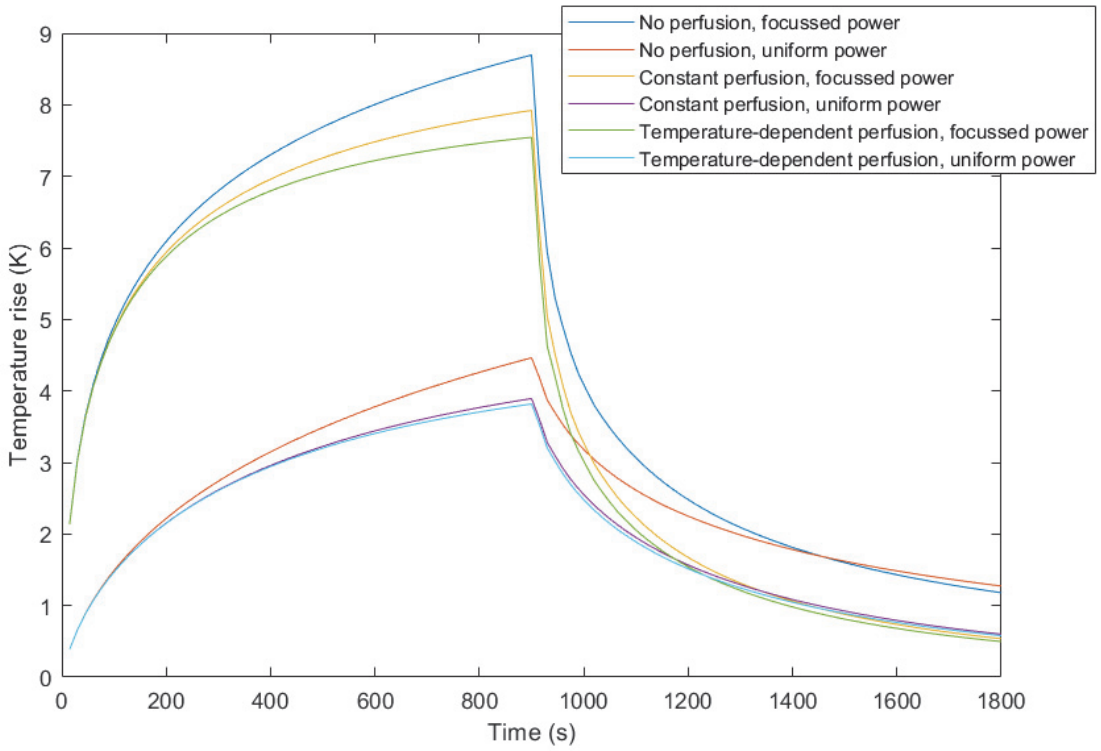

Figure 53: Temperature rise for all six cases with maximum deposited power.

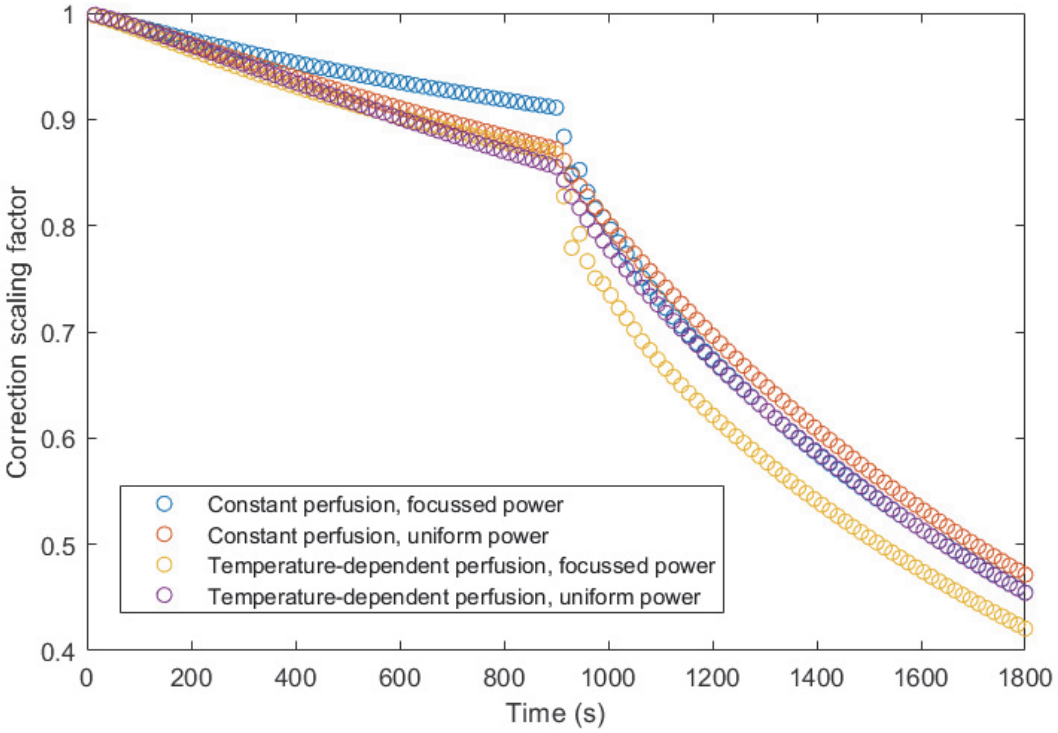

Figure 54: Correction scaling factor, calculated as the ratio of the maximum temperature rise in a model with perfusion to the maximum temperature rise in a model without perfusion.

Table 25: Values of the correction factor after 900 s for each model.

	Constant perfusion	Temperature-dependent perfusion
Focussed power	0.91	0.87
Uniform power	0.87	0.86

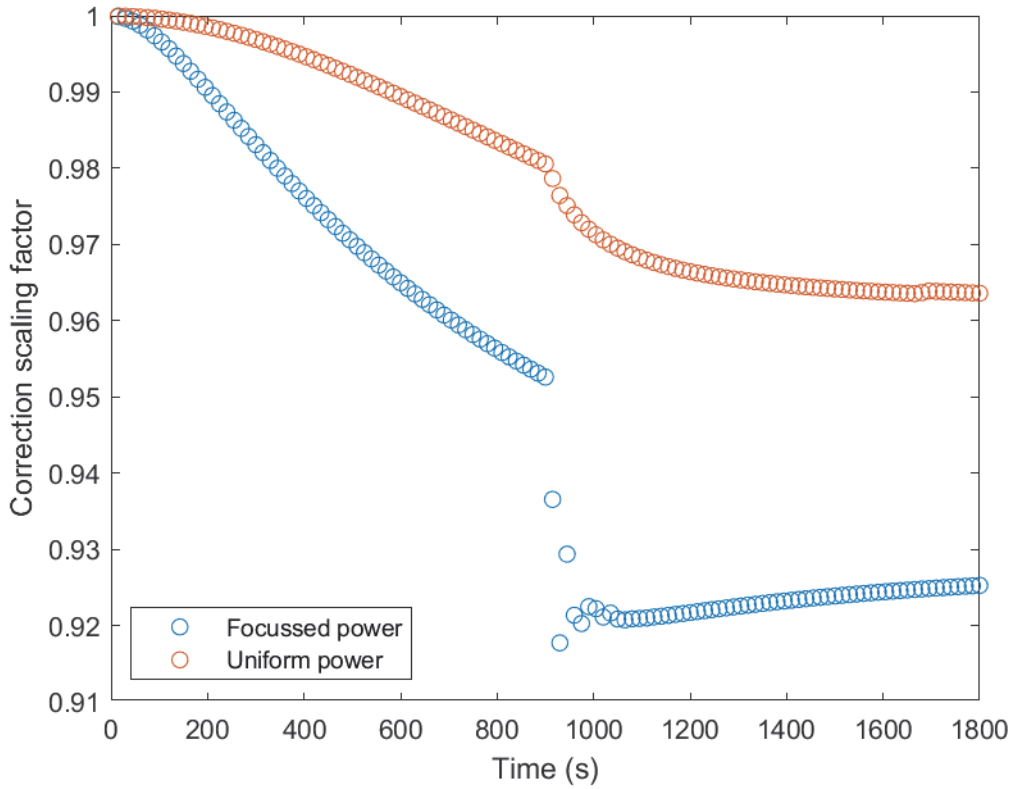

Figure 55: Ratio of temperature rise with temperature-dependent perfusion to temperature rise with constant perfusion.

The effects of perfusion were also considered for GC simulations, as is described in full in deliverable 6 of the MIMAS project [46]. The six base case models described at the end of section 5.1 were adapted to remove the perfusion coefficient from all tissues labelled as bone, fat or muscle. The temperature rise increased in all models, by between 6 % and 15 % in Yoon-Sun and by between 3 % and 7 % in Glenn, with the details of the increase depending on the implant location and the method used when applying the virtual surgery.

A further investigation was carried out that sought to compensate for the lack of perfusion in the gel phantom used in ASTM-F2182 by adjusting the thermal properties of the gel so that the temperature rise experienced by an implant in the gel phantom was as similar as possible to the temperature rise experienced by the same implant in the Yoon-Sun and Glenn anatomical models. It was found that a reduction of the thermal conductivity and specific heat capacity to 80 % of their original values led to agreement in maximum temperature rise to within 10 % of the result from the full anatomical model. This approach may indicate a useful avenue of investigation for further development of the ASTM standard.

6 FEASIBILITY OF A STOCHASTIC RISK ANALYSIS FOR MR IMPLANT SAFETY

A stochastic approach for assessment of new implants requires the many factors that affect the extent of heating during an MRI scan to be quantitatively linked to the temperature rise through a model. In addition it requires the uncertainties associated with each factor to be well-characterised and for it to be possible to propagate the uncertainties through the model so that an overall uncertainty can be associated with the estimated temperature rise. This information will ensure that safety can be assessed using statistically sound evidence. A further consideration, beyond the scope of this project, is how to go about defining an acceptable level of risk or an acceptable value of temperature rise.

It should be noted that significant steps towards creation of a framework and toolkit for use of a stochastic approach have already been made my ZMT, project partners on MIMAS. Their work on active implant safety [24] has created an approach, illustrated in figure 56, that combines a validated model of the implant with electromagnetic fields that are representative of a wide range of scan configurations and a variety of human body types to create an RF heating risk assessment that takes the variability of both scan parameters and patient properties into account when estimating the temperature rise in the patient due to the implant. In theory, a similar approach could be applied to any type of implant.

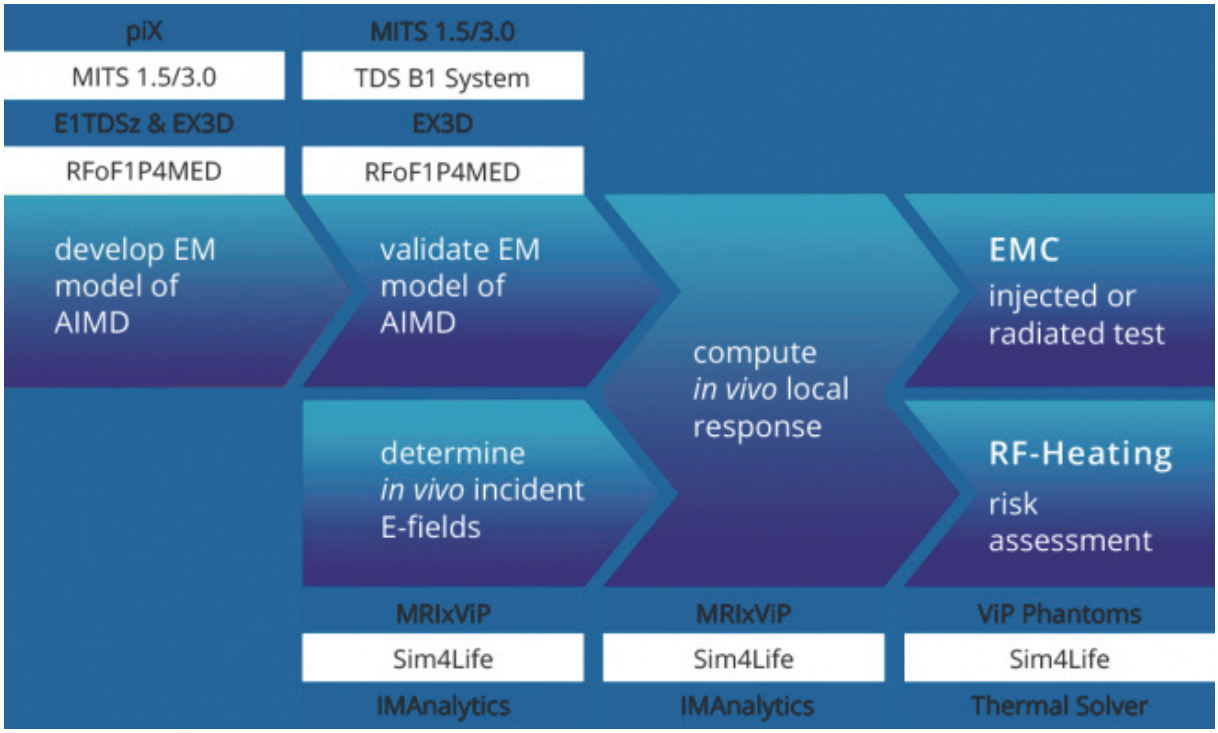

Figure 56: Illustration of the ZMT stochastic approach to MRI safety for active implants.

The work reported above has shown that the provision of the model linking temperature rise to the various quantities that it depends on is by no means straightforward, and that the provision of associated uncertainties is also highly problematic.

The geometry of a typical orthopaedic implant is complex, and typically the geometric complexity is essential to the reliable functioning of the implant so cannot be removed. The details of localised heating are strongly dependent on the details of the geometry as this determines both the electromagnetic fields in and around the implant, and the heat transfer between the implant and the surrounding tissue. Whilst some qualitative observations relating implant volume (for gradient coil fields) and maximum dimension in the direction of

the field (for RF fields) to temperature rise have been made above, these observations are not sufficient to provide reliable quantitative estimates for the temperature rise caused by a given implant. The attempts to fit parametric models to the RF and GC data have been moderately successful for small implants, but these are fits to models of highly simplified geometries, and a direct comparison of detailed and approximate models shows significant differences in temperature rise.

A further complicating factor is the material properties of the implant. The work reported in this project has used the thermal and electromagnetic properties of materials that are commonly used in medical implants, and has assumed that the entire implant is made of a single homogeneous material. This focus has meant that a thorough parametric exploration of the effects of material properties has not been carried out, and so no quantitative model linking temperature rise to implant material properties is available. An additional complication is that real-world implants may be constructed from several different materials, and that material properties and geometric details of the various parts may not be easily available.

Not all implants are geometrically complex: the work reported in sections 2.2 and 3.4 has shown that screws and plates can be well approximated by cylinders and cuboids in RF scans. However, the work reported in sections 2.3 and 3.3 has shown that developing simple parametric models for prediction of temperature rise is not straightforward even for well-parameterised simple geometries. The unsatisfactory outcome of these fitting processes suggests that something other than polynomial approximation may be necessary, but the lack of successfully fitted models means that a stochastic approach to risk assessment is not currently possible.

The temperature rise that an individual person will experience when undergoing a scan will depend not only on the implant geometry, location within the scanner, and orientation, but also on the nature of the tissue directly surrounding the implant. In general, fatty tissue has a lower thermal conductivity than muscle, and so will not move heat away from the implant as quickly, and has a lower specific heat capacity, so the deposition of the same amount of energy in fat and in muscle will lead to a higher temperature rise in the fat. The lack of detailed knowledge of the tissue types surrounding and implant ahead of scanning the patient means that there is a significant source of uncertainty that affects the feasibility of a stochastic approach. The process of perfusion is a further source of uncertainty, particularly since some conditions that could be diagnosed via an MRI scan may create reduced perfusion, increasing the risk of a higher temperature rise in the patient.

The scanner settings for the gradient coil approach and the scan sequences for both modalities have a strong effect on the temperature rise, as has been shown in sections 4.2 and 3.2. These effects have proved to be more straightforward to model than geometric and material property dependencies, but the uncertainties associated with these parameters may be difficult to obtain.

7 REFERENCES

[1] ASTM F2182-11 (2011) “Standard test method for measurement of radio frequency induced heating on or near passive implants during magnetic resonance imaging”, ASTM 2011, DOI: 10.1520/F2182-11

[2] https://www.medartis.com/documentation/product-brochures/ Accessed September 2021.

[3] COMSOL Multiphysics® v. 5.5. COMSOL AB, Stockholm, Sweden, 2020.

[4] Giulio Giovannetti, Luigi Landini, Maria Filomena Santarelli, and Vincenzo Positano. “A fast and accurate simulator for the design of birdcage coils in MRI”. *Magnetic Resonance Materials in Physics, Biology and Medicine*, **15(1-3)**, 36-44, 2002.

[5] Luca Zilberti, Umberto Zanovello, Alessandro Arduino, Oriano Bottauscio, and Mario Chiampi. “RF-induced heating of metallic implants simulated as PEC: Is there something missing?” *Magnetic Resonance in Medicine*, **85(2)**, 583-586, 2020.

[6] https://zurichmedtech.com/validation-hw/mits-systems/mits1-5/ Accessed September 2021.

[7] ISO/TS 28038:2018, Determination and use of polynomial calibration functions.

[8] Alessandro Arduino, Oriano Bottauscio, Rüdiger Brühl, Mario Chiampi, and Luca Zilberti. “In silico evaluation of the thermal stress induced by MRI switched gradient fields in patients with metallic hip implant”. *Physics in Medicine and Biology*, **64(24)**:245006, 2019.

[9] Oriano Bottauscio, Mario Chiampi, Jeff Hand, and Luca Zilberti. “A GPU computational code for eddy-current problems in voxel-based anatomy”. *IEEE Transactions on Magnetics*, **51(3)**, 1-4, 2015.

[10] Luca Zilberti, Oriano Bottauscio, Mario Chiampi, Jeffrey Hand, Hector Sanchez Lopez, Rüdiger Brühl, and Stuart Crozier. “Numerical prediction of temperature elevation induced around metallic hip prostheses by traditional, split, and uniplanar gradient coils”. *Magnetic Resonance in Medicine*, **74(1)**, 272-279, 2015.

[11] Alessandro Arduino, Oriano Bottauscio, Mario Chiampi, and Luca Zilberti. “Douglas-Gunn method applied to dosimetric assessment in magnetic resonance imaging”. *IEEE Transactions on Magnetics*, **53(6)**, 1-4, 2017.

[12] L. P. Panych and B. Madore. “The Physics of MRI Safety”, *Journal of Magnetic Resonance Imaging*, **47**, 28-43, 2018. doi: 10.1002/jmri.25761

[13] P. A. Bottomley et al. “Estimating Radiofrequency Power Deposition in Body NMR Imaging”, *Magnetic Resonance in Medicine*, **2**, 336-349, 1985. doi: 10.1002/mrm.1910020404

[14] P. A. Bottomley and W. A. Edelstein. “Power Deposition in Whole-Body NMR Imaging”, *Medical Physics*, **8(4)**, 510-512, 1981. doi: 10.1118/1.595000

[15] J. Wang et al. "Factors Influencing Flip Angle Mapping in MRI: RF Pulse Shape, Slice-Select Gradients, Off-Resonance Excitation, and B0 Inhomogeneities", *Magnetic Resonance in Medicine*, **56**, 463-468, 2006. doi: 10.1002/mrm.20947

[16] Z. Wang and C. M. Collins. “Effect of RF Pulse Sequence on Temperature Elevation for a Given Time-Average SAR”, *Concepts Magn Reson Part B Magn Reson Eng*., **37B(4)**, 215-219, 2010. doi: 10.1002/cmr.b.20172

[17] https://www.england.nhs.uk/statistics/statistical-work-areas/diagnostic-imaging-dataset/ Accessed September 2021.

[18] https://www.ons.gov.uk/peoplepopulationandcommunity/populationandmigration/populationestimates/datasets/2011censuspopulationandhouseholdestimatesfortheunitedkingdom Accessed September 2021.

[19] https://www.ons.gov.uk/peoplepopulationandcommunity/birthsdeathsandmarriages/deaths/datasets/deathsregisteredinenglandandwalesseriesdrreferencetables Accessed September 2021.

[20] https://www.njrcentre.org.uk/njrcentre/Reports-Publications-and-Minutes/Annual-reports Accessed September 2021.

[21] https://www.njrcentre.org.uk/njrcentre/Reports-Publications-and-Minutes/Public-and-Patient-Guide Accessed September 2021.

[22] https://www.ncbi.nlm.nih.gov/books/NBK436873/ Accessed September 2021.

[23] https://www.researchgate.net/publication/44247441_Comparison_of_Constant_and_Temperature_Dependent_Blood_Perfusion_in_Temperature_Prediction_for_Superficial_Hyperthermia Accessed September 2021.

[24] https://zmt.swiss/applications/mri-active-implant-safety/ Accessed September 2021.

[25] Smithells Metals Reference Book, 7th Edition. Edited by E.A. Brandes & G.B. Brook (1992) ISBN 0750610204. Table 14.8.

[26] http://asm.matweb.com/search/SpecificMaterial.asp?bassnum=mtu010 Accessed September 2021.

[27] http://asm.matweb.com/search/SpecificMaterial.asp?bassnum=MTU011 Accessed September 2021.

[28] http://asm.matweb.com/search/SpecificMaterial.asp?bassnum=MTU020 Accessed September 2021.

[29] http://asm.matweb.com/search/SpecificMaterial.asp?bassnum=MTU021 Accessed September 2021.

[30] http://asm.matweb.com/search/SpecificMaterial.asp?bassnum=MTU030 Accessed September 2021.

[31] http://asm.matweb.com/search/SpecificMaterial.asp?bassnum=MTU031 Accessed September 2021.

[32] http://asm.matweb.com/search/SpecificMaterial.asp?bassnum=MTU040 Accessed September 2021.

[33] http://asm.matweb.com/search/SpecificMaterial.asp?bassnum=MTU041 Accessed September 2021.

[34] http://asm.matweb.com/search/SpecificMaterial.asp?bassnum=MTP641 Accessed September 2021.

[35] http://asm.matweb.com/search/SpecificMaterial.asp?bassnum=MTP644 Accessed September 2021.

[36] http://asm.matweb.com/search/SpecificMaterial.asp?bassnum=MTP642 Accessed September 2021.

[37] http://asm.matweb.com/search/SpecificMaterial.asp?bassnum=MTP645 Accessed September 2021.

[38] http://asm.matweb.com/search/SpecificMaterial.asp?bassnum=MTP643 Accessed September 2021.

[39] http://www.metalcor.de/en/datenblatt/130/ Accessed September 2021.

[40] https://www.upmet.com/sites/default/files/datasheets/ti-6al-4v-eli.pdf Accessed September 2021.

[41] http://www.matweb.com/search/datasheet_print.aspx?matguid=c4297fb8f1094da189732c224e3be1ed Accessed September 2021.

[42] https://www.finetubes.co.uk/-/media/ametekfinetubes/files/products/materials/titanium%20tubes/fine_tubes_-_ti_6al_4v.pdf?la=en Accessed September 2021.

[43] https://www.spacematdb.com/spacemat/manudatasheets/TITANIUM%20ALLOY%20GUIDE.pdf Accessed September 2021.

[44] Robert L McIntosh and V Anderson. “A comprehensive tissue properties database provided for the thermal assessment of a human at rest”, Biophysical Reviews and Letters 5(3), 129-151, 2010. https://doi.org/10.1142/S1793048010001184

[45] Camelia Gabriel and Sami Gabriel. “Compilation of the dielectric properties of body tissues at RF and microwave frequencies”. Armstrong Laboratory report AL/OE-TR-1996-0037, 1996. Available from http://niremf.ifac.cnr.it/docs/DIELECTRIC/home.html

[46] Internal INRIM report, “Report on the results of the investigation of the hazards associated with the interaction between metallic implants and switched magnetic fields in the kilohertz regime”, May 2021.